Università degli Studi di Ferrara

DOTTORATO DI RICERCA IN
SCIENZE DELL'INGEGNERIA

CICLO XXIII

COORDINATORE Prof. Trillo Stefano

A 3D ENVIRONMENT FOR SURGICAL PLANNING AND SIMULATION

Settore Scientifico Disciplinare ING-INF/05

Dottorando
Dott. Chiarelli Tommaso

____
(firma)

Tutore
Prof. Lamma Evelina

____
(firma)

Tutore esterno
Dott. Sansoni Tommaso

Anni 2007-2009

ABSTRACT

(ENG)

The use of Computed Tomography (CT) images and their three-dimensional (3D) reconstruction has spread in the last decade for implantology and surgery. A common use of acquired CT datasets is to be handled by dedicated software that provide a work context to accomplish preoperative planning upon. These software are able to exploit image processing techniques and computer graphics to provide fundamental information needed to work in safety, in order to minimize the surgeon possible error during the surgical operation. However, most of them carry on lacks and flaws, that compromise the precision and additional safety that their use should provide. The research accomplished during my PhD career has concerned the development of an optimized software for surgical preoperative planning. With this purpose, the state of the art has been analyzed, and main deficiencies have been identified. Then, in order to produce practical solutions, those lacks and defects have been contextualized in a medical field in particular: it has been opted for oral implantology, due to the available support of a pool of implantologists. It has emerged that most software systems for oral implantology, that are based on a multi-view approach, often accompanied with a 3D rendered model, are affected by the following problems: unreliability of measurements computed upon misleading views (panoramic one), as well as a not optimized use of the 3D environment, significant planning errors implied by the software work

context (incorrect cross-sectional planes), and absence of automatic recognition of fundamental anatomies (as the mandibular canal). Thus, it has been defined a fully 3D approach, and a planning software system in particular, where image processing and computer graphic techniques have been used to create a smooth and user-friendly completely-3D environment to work upon for oral implant planning and simulation. Interpolation of the axial slices is used to produce a continuous radiographic volume and to get an isotropic voxel, in order to achieve a correct work context. Freedom of choosing, arbitrarily, during the planning phase, the best cross-sectional plane for achieving correct measurements is obtained through interpolation and texture generation. Correct orientation of the planned implants is also easily computed, by exploiting a radiological mask with radio-opaque markers, worn by the patient during the CT scan, and reconstructing the cross-sectional images along the preferred directions. The mandibular canal is automatically recognised through an adaptive surface-extracting statistical-segmentation based algorithm developed on purpose. Then, aiming at completing the overall approach, interfacing between the software and an anthropomorphic robot, in order to being able to transfer the planning on a surgical guide, has been achieved through proper coordinates change and exploiting a physical reference frame in the radiological stent. Finally, every software feature has been evaluated and validated, statistically or clinically, and it has resulted that the precision achieved outperforms the one in literature.

ABSTRACT
(ITA)

L'uso di immagini ottenute tramite Tomografia Assiale Computerizzata (TAC), e la loro ricostruzione tridimensionale (3D), si è diffusa negli ultimi decenni per l'implantologia e la chirurgia. Un uso comune dei dataset di TAC è di essere gestiti da software dedicati che forniscono un contesto di lavoro su cui effettuare pianificazione preoperatoria. Questi software sono in grado di sfruttare tecniche di elaborazione delle immagini e grafica computerizzata per fornire informazioni fondamentali necessarie per lavorare in sicurezza, in maniera da minimizzare il margine d'errore del chirurgo durante un intervento. Tuttavia, la maggior parte di loro è gravata da mancanze e difetti, che compromettono la precisione e la sicurezza aggiuntiva che il loro uso dovrebbe conferire. L'attività effettuata durante il dottorato di ricerca ha riguardato lo sviluppo di un software ottimizzato per la pianificazione chirurgica preoperatoria. Con questo proposito, è stato analizzato lo stato dell'arte, e sono state identificate le relative carenze principali. Poi, in maniera da produrre soluzioni pratiche, le mancanze e difetti riscontrati sono stati contestualizzati in un campo medico in particolare: è stata scelta l'implantologia dentale, in relazione alla disponibilità a supportare questa ricerca da parte di un gruppo di implantologi. E' emerso che la maggior parte dei software per l'implantologia orale, che sono basati su un approccio multi-vista, spesso accompagnato da una vista dedicata al modello 3D della struttura ossea, sono affetti dai seguenti problemi: inaffidabilità delle

misurazioni effettuate su viste ingannevoli (quella panoramica), così come un uso dell'ambiente 3D non ottimizzato, significativi errori di pianificazione implicati dal contesto di lavoro del software (piani cross-sectional incorretti), e l'assenza di riconoscimento automatico di anatomie fondamentali (come il canale mandibolare). Perciò, è stato seguito un approccio 3D, e definito un software di pianificazione nello specifico, integrando tecniche di elaborazione delle immagini e di grafica computerizzata. Il risultato è un ambiente 3D pratico, semplice, e completamente integrato, su cui lavorare, per la simulazione e pianificazione implantare orale. Si è definito un algoritmo di interpolazione, applicato sulle immagini TAC assiali, per produrre un volume radiografico continuo ed un voxel isotropico, in maniera da ottenere un contesto di lavoro su cui effettuare misure corrette. La possibilità di ricostruire arbitrariamente, durante la pianificazione, i migliori piani cross-sectional per conseguire misurazioni corrette, è ottenuta tramite interpolazione e generazione di texture. Anche il corretto orientamento degli impianti pianificati è facilmente conseguibile, sfruttando una maschera radiologica equipaggiata con reperi radio-opachi, indossata dal paziente durante la scansione TAC, e ricostruendo le immagini cross-sectional lungo le direzioni preferite. Il canale mandibolare è riconosciuto automaticamente tramite un algoritmo adattivo, appositamente sviluppato, basato sulla segmentazione statistica e l'estrazione di superficie. Poi, mirando al completamento dell'approccio globale, è stato implementato l'interfacciamento tra il software ed un robot antropomorfo, in maniera da poter trasferire la pianificazione su una guida chirurgica, ed è stato ottenuto tramite appropriati cambi di coordinate e sfruttando un riferimento fisico nella mascherina radiologica. Infine, ogni soluzione software implementata è stata valutata e convalidata, statisticamente o clinicamente, e la precisione ottenuta è risultata essere nettamente superiore alla corrispettiva in letteratura.

INDEX

INTRODUCTION

Medical imaging is the subject involving the study of the application of image processing techniques, computer graphics, and computer vision in support of diagnostic imaging. Nowadays medical imaging indeed is a research field: it includes computer science competencies related to computer graphics, image processing, computer vision, and medical ones, related to necessities definition, meta-products comprehension, and result interpretation. This field has born because of the transition from film bases systems, as common radiographic devices, to digital and computer-based ones: during the years, different procedures have been developed, and each one has found the proper medical field, in relation to determinant factors like the set-up and maintenance costs, level of danger in regard of the patient, timings (exam duration and number of necessary scans), and inherent characteristics of the achieved product (more suitable for morphologic highlighting of certain tissues rather than others, or more appropriate for functional-metabolic tracing). Among the most used procedures there are Computed Tomography (CT), Magnetic Resonance Imaging (MRI), Medical Ultrasonography, and Nuclear Medicine. The result of these techniques is an informative dataset that, through the proper software, provides a detailed visualization of the anatomical section (or metabolic path) of interest for the related doctor, without the need of a surgical intervention.

A common use of the achieved information is the diagnostic imaging in support of preoperative planning. This concerns cases in which the exam is applied before the surgical operation, and because of this planning, the doctor is then able to perform the surgical operation less invasively and with more safety for the patient, due to the wider knowledge obtained about the area of interest. In implantology in particular, but in general in the surgical field, the doctor needs complete information about structures and tissues which he/she has to operate upon, in order to get a precise planning, which the common images only, the ones obtained by radiographic devices, are not enough for. With the aim of helping the operator, there are preoperative planning software that takes care of calculating fundamental data to operate in safety, and provides, through digital reconstruction, meaningful anatomical sections different from the axial one (the common horizontal slice plane, that is orthogonal to the body axis). Therefore, the purposes of the preoperative planning, as well as of the related software, are the minimization of the surgeon possible error during the surgical operation, that is reaching the complete predictability of the surgical act, the decreasing of the operative invasiveness and patient postoperative discomfort, as well as the significant reduction of surgical timings. However, still nowadays, most of the state-of-the-art planning software carry on deficiencies and flows that compromise the precision and additional safety that their use should provide.

The research accomplished during my PhD career has concerned medical imaging, and the development of an optimized software for surgical preoperative planning in particular. It has involved the study of the state-of-the-art software and technologies about, the collaboration with field experts, as well as the resulting acquisition of the necessary medical knowledge. Then, the solution of the most significant planning software common lacks and defects identified has been defined as main research objective, in order to provide to doctors a really reliable and precise work context to accomplish planning on, significantly supporting minimally invasive surgery as a result. The four most meaningful deficiencies identified, and consequently which it has been researched a solution for, concerned unreliability of measurements computed upon these tools, both for 1) misleading views and 2) lack of volume anisotropy handling, 3) significant planning errors implied by software provided working planes, and 4) absence of automatic functionalities to support the operator about fundamental anatomies recognition. The related accomplishment needed the definition of the most suitable protocol, the development of several innovative algorithms, and the application of advanced image processing and computer graphics techniques, as well as an intensive testing and experimentation.

The aim of this thesis is to report the doctorate activity performed, to explain the adopted approaches, and to describe the developed solutions. The dissertation is organized as follows.

In Chapter 1 a brief overview about the related environment is reported, followed by the presentation of the research objectives and their contextualization in a medical field in particular.

The innovative software framework developed, thought to provide a reliable and optimized fully 3D work-context, as well as the defined global approach, is described in Chapter 2, together with its most important features and the technology involved.

Chapter 3 shows the 2 passes interpolation algorithm developed in order to correctly handle anisotropy datasets, with its evaluation at the end.

Chapter 4 shows manual and automatic solutions concerning the reconstruction of correct and optimal working planes, and consequent related features, including their evaluation and validation.

Techniques and procedures used to achieve the relevant anatomy recognition, both manually and automatically, as well as their evaluations, are reported in Chapter 5.

Moreover, in Chapter 6, in order to complete the approach defined, is described the interfacing of the software with a robot, that is able to produce a surgical guide based on the accomplished planning.

Finally, Chapter 7 and Chapter 8 are respectively dedicated to a survey of related works and conclusions about the accomplished activity. Then, the dissertation ends with references and publications.

CHAPTER 1: MEDICAL IMAGING

Starting with the first X-ray Computed Tomographies (CT) devices in the early ’70, it has been possible to observe a significant evolution of techniques of acquisition, reconstruction, and improvement, as well as compression, memorization, analysis, and visualization of medical diagnostic images. From film working systems, as common radiographic devices, providing analogical, static, and two-dimensional information, it has been passed to computers based devices, that work with digital, possibly dynamic, and most three-dimensional data (Duncan & Ayache 2000). The Medical Imaging has born due to the described transition towards digital information: this field is related to the study of diagnostic imaging through the application of advanced image processing and state-of-the-art computer graphics techniques. Nowadays this discipline has great importance in several medical fields: the use of the Computed Tomography (CT) is a common practice, and it plays a fundamental role assisting pre-operative planning, due to the high resolution of images produced. As a consequence, software systems have been realized to take advantage of the CT devices and support the doctor, providing analysis and synthesis functions and helping to formulate th best diagnosis, in order to ease and optimize the related medical procedures.

.

1.1 COMPUTED TOMOGRAPHIES

Computer Tomography devices are the most used in diagnostic imaging, due to their low cost and high spreading. Data acquisition is achieved through rotation around patient's body of a X-ray emitter and some receivers, coherent each other, in correspondence of the are to be analized. Information obtained through this device consists of a series of transaxial images orthogonally aligned to the patient height/vertical axis, that is the axis that corresponds to the patient's spine. Each of those image is called *slice* because it represents a determined *thickness* cut of the patient's body. Other relevant slices properties are the *resolution*, that is defined by length and width of the image in pixels (from *picture element*, the image measure unit), the *pixel size* in millimetres, homogenous in the transaxial plane (length equal to width), and their *amount*, that depends on the constant distance among the slices (called *interslice*) and the total extent of the analyzed area. Moreover, due to the fact that these slices have a third dimension, that is the thickness, it is also possible to refer to the single slice measure unit as *voxel* (from *volume element*), that is the three-dimensional (3D) version of the two-dimensional (2D) image pixel. Every slice voxel ideally represents the absorption factor of the tiny corresponding volume of the patient's body. In order to define the amount of absorption, it has been defined a standard measure unit known as Hounsfield Unit (HU), that has its zero in the water absorption level (0 HU), and it corresponds to -1000 HU for air and above 200 HU for bones.

Although the following three-dimensional reconstruction (slices stacking) can be achieved on any slices series, correctness and precision of the final image are directly correlated to constraint set and consequently to data integrity. As a result, the parameters choice, like slice thickness and interslice value, is an important step. It has also quite relevant that, even if technically it is possible to achieve high resolution scans, and better quality images as a consequence, it does imply an higher dosage of radiation on the patient and a longer time of exposure, decreasing the operation safeness. Moreover, the time factor would also increase the chance of patient movements during the scanning, apart from possibly create greater discomfort. In this regard, it has been also developed a fast and low radiation factor technique, called Cone Beam Computed Tomographies (CBCT), due to its cone-like X-ray shape. Images achieved with CBCT scan devices are usually characterized by a lower resolution in comparison to the CT ones, however the research works hardly on it, and it is possible to wish for good-quality, low-radiant computed tomographies in the future.

1.2 DICOM 3 FORMAT

Initially, every CT scan manufacturer defined its own file format to store the digital information provided by the device. Obviously, this generate confusion and impeded the CT spread. Thus, the Association of Electrical and Medical Imaging Equipment Manufacturer (NEMA) decided to develop an industrial standard of communication for medical images, called DICOM, the last official version of which is the third (DICOM/3). This standard handles many types of medical images, above all radiological ones, including related information. Actually DICOM/3 is more like a collection of rules to define medical imaging information sharing, among which there is the classification of a series of “objects” that identify radiological data (“patient”, “image”, etc…) and how they are related each other. This is the known Object Oriented structure, in which every object includes related series of attributes (e.g. the patient object will contain personal records, hospitalization data, etc…).

It is taking advantage of this format, that CT processing software systems are able to achieve all the needed information from CT datasets, elaborating and processing them in order to support the doctor diagnosis and planning.

1.3 RESEARCH OBJECTIVES

The use of Computed Tomography images and their three-dimensional reconstruction has spread in the last decade for surgery. Image processing tools and computer graphic techniques for animation and visualization are powerful ways to achieve measure of size, distance and texture consistency. Many tools are currently used as semi-automatic ones: starting from CT images, after 3D reconstruction, the operator (radiologist or surgeon) works on a two-dimensional multi-view environment, characterized by meaningful sections of the original dataset, where measures can be computed. Some of them, besides the 2D views, also show a 3D surface rendered model of the bone (e.g., for oral implantology, SurgiCase® and SimPlant®, Materialise and CAD Implant, Praxim™). The output of these latter systems can be exploited in order to produce 3D stereolithographic models. However, these stereolithographic models correspond only to the bone structure, and do not fit with the human anatomy the implantologist does operate upon.

Even if nowadays there are several pre-operative planning software tools commercially sold, the state of the art has not completely reached a very high level of reliability yet, and this gain a particular relevance in consideration of any related surgical operation that follows. There are still some structure weak points, deceiving or imprecise working views, unreliable achievable measurements, and lacks in general. Few of the top-rated software showed to handle some of these deficiencies, and no one demonstrated to take care of many of them and to provide evidence of a very high precision to report it. The main focus of this research has been about developing of a procedure aimed at increasing precision and safeness of surgical acts and implantological applications in general, and a reliable state of the art software able to support the overall procedure, in particular. With this intention, the first step has been to analyse and define the significant problems of the current planning software in commerce. The most relevant ones that have been identified are the follows:

1. outdated common multi-view working contexts: due to tradition or habits, it may happen that cut views are provided by software independently from their being obsolete or misleading;
2. complete or partial absence of CT dataset anisotropy handling;
3. implicitly distorted working views and consequent implied imprecision in measurements computed over them;
4. lack of automatic algorithms to help the doctor to identify anatomies relevant for the related surgical operation, in order to support the overall precision.

Once defined the objectives in general (i.e. solving the four problems described), it has been decided a specific field to apply the research onto, in order to start finding solutions for real problems, leaving the opportunity to extend them to similar cases in other surgical areas. The medical field that has been chosen to focus about is oral implantology, due to the option to take advantage of a dentist study in Cattolica (RN, Italy), with its related labs, instrumentations, and materials. This possibility has been a courtesy of Dr. Franchini, the study owner, that also helped sharing its medical knowledge. Thus, the identified general problems have been concretized into the specific ones of the chosen field, and solutions found have been reported in this volume.

In the following subsections the significant lacks 1÷4 above are described in details for the case of oral implantology planning software systems.

1.3.1 COMMON MULTI-VIEW CONTEXT

The typical oral implantology planning software systems provide a quite common multi-view context of work: loaded the CT dataset, they are able to three-dimensionally reconstruct the radiographic volume, cut it following determined cut planes, and display the consequent working views in the framework of the window.

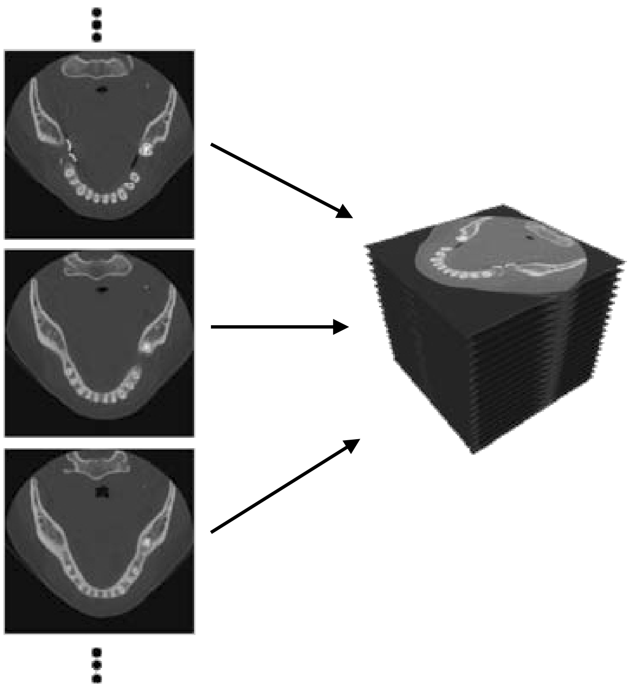

Fig. 1.1. *Radiographic volume 3D reconstruction (slices stacking)*

The common views combination, known as Dentascan in relation to the pioneer software that defined it (DentaScan, GE Medical System), consists of:

- *axial* images, those directly acquired from the instrument (or computed by interpolation, but lying on the acquisition plane);
- *panoramic* images, orthogonal to a curve (*panoramic cutting curve*) drawn on an axial image that follows the curvature of the maxillary or mandibular ridge (this curve is usually manually identified via a series of data points buccal to the midzone of the bone in an axial image);
- *cross-sectional* (or *oblique*) images, orthogonal to the previous mentioned series of images.

In Fig. 1.2 is shown the common multi-planar work context described. This multi-view approach is very much spread, and almost every oral implantology planning software provides its framework following that schema, but, after an analysis and some knowledge sharing with implantologists and dentists, it resulted to be not the best to plan surgical operations upon. Essentially, excluding the axial plane, needed to define the others planes and to accomplish diagnosis in top-down direction for mandibles and viceversa for maxillas, there is only one view on which measures should be computed and planning is actually performed: the cross-sectional images one.

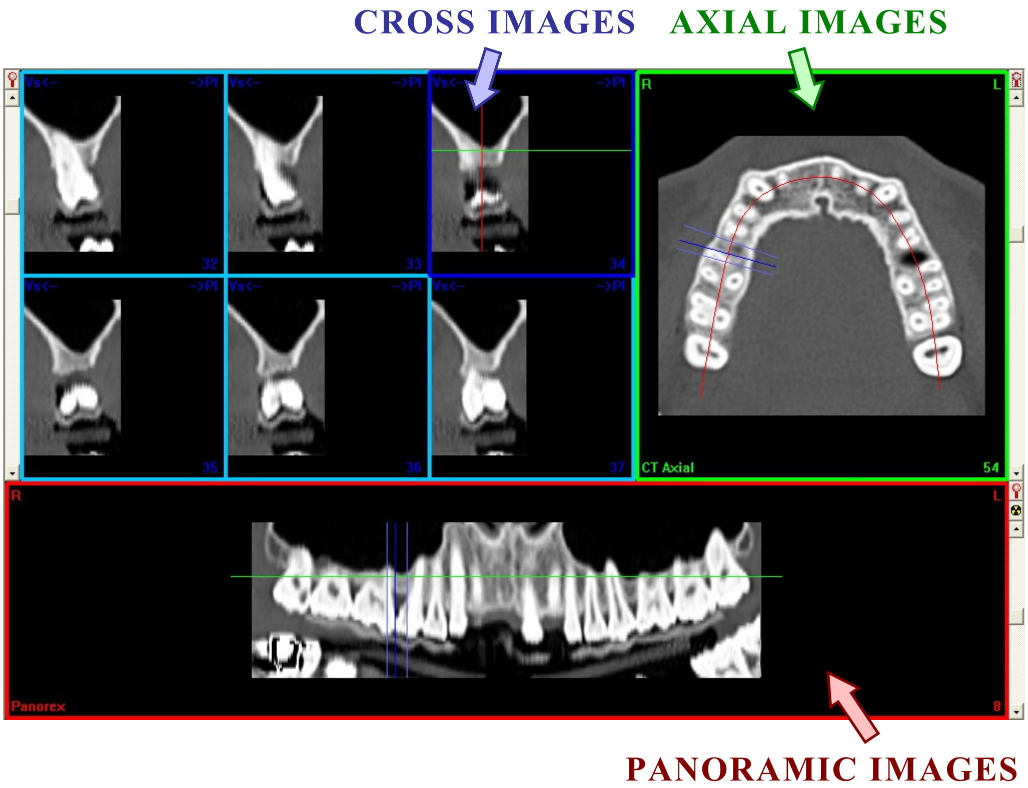

Fig. 1.2. *Common multi-view working context*

It is upon this one that implantologists compute the fundamental measurements, check areas fitting, and plan implants insertion. The panoramic view, instead, is not really used to plan anything, and surely it cannot be used to achieve important measures from, due to its misleading nature. Actually, the panoramic images are obtained through the projection of a curve plane (i.e. red curve in the top-right green-edged view in Fig. 1.2) on a two-dimensional rectangular one (bottom red-edged view in Fig. 1.2), thus implying incorrect intra-distances, and wrong measures consequently. It remains, though, an orienting view, allowing to clarify objects positions being a third point of view of the radiographic dataset, that is providing a kind of third dimension perspective, but nothing else. It could be affirmed that the panoramic view is necessary to identify some relevant anatomies, but, using the right algorithms and tools, cross-sectional and axial planes can fit to the same role. Therefore, the will to keep this view can be associated to tradition (representing the digital version of the orthopantomogram) and habits (being doctors used to this common software framework), at the cost of providing an unsafe working context to the user.

Some of the mentioned software (SurgiCase® and SimPlant®, Materialise; CAD Implant, Praxim™) are also able to provide a 3D dedicated view, in which a model of the bone structure can be three-dimensionally reconstructed throw the use of proper algorithms. Usually, this model has only the role to show the bone structure or to allow the production of a related stereolithographic model. Moreover, apart from few cases (e.g. SimPlant®, Materialise), generally the 3D view is not connected with the two-dimensional ones, depriving from the possibility to plan over it as on the first ones, or, even if it is, the communication between the contexts has necessarily to pass through approximating translations of dimensionally different coordinate systems. As a result, this approach, independently from the insertion of a three-dimensionally reconstructed surface, is still multi-view: even if a 3D rendered model of the bone structure can be presented to the user, implant planning is done in a 2D multi-planar environment.

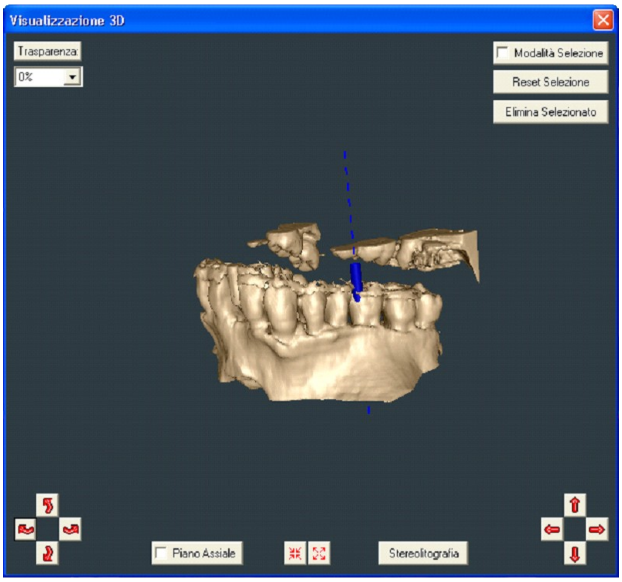

Fig. 1.3. *Ad-hoc and multi-view parted 3D model view*

In relation to the reported considerations, it appears to be clear that the commonly proposed framework is not the best on which an implantologist may work upon, surely not optimized at all, often structurally rough, and above all misleading.

1.3.2 VOLUME ANISOTROPY

Still nowadays, most of the CT scanners are not beforehand ready to the specific purpose of providing an isotropic dataset by default. Almost always is concern of the implantologist to ask to the radiology responsible about that prerequisite compliance, and even in that case the asked requirement is not granted for sure. In addition, it is not

uncommon or odd for an implantologist to receive anisotropic CBCT volumes too, even if the related scanners are prepared on purpose, and due to their different working system, to isotropy conformity.
The lack of isotropy appears when the dataset interslice value, that is the distance between the beginning of a slice and the beginning of the following, is not equal to the dataset pixel size. This parameter describes the length and width of the slice/image pixel, that, considering the dataset as a whole, correspond to the related dimensions of the voxel base (see Fig. 1.4). Notice that, actually, the pixel size value is defined by two parameters, but, following the DICOM standard in relation to computed tomographies, they are equals.

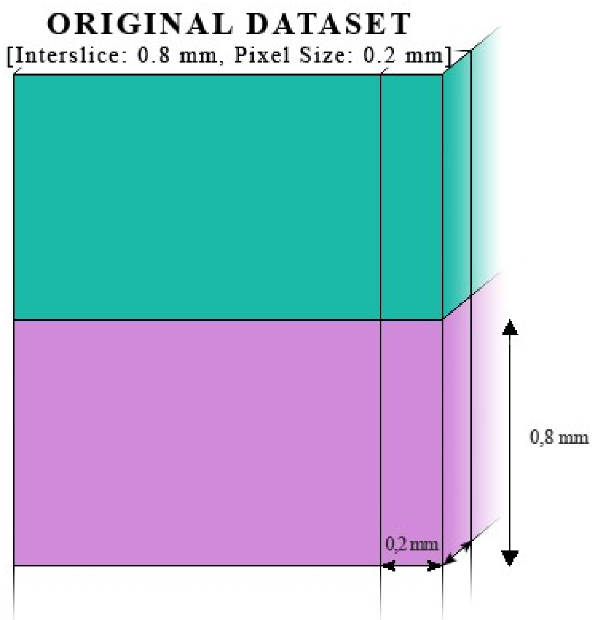

Fig. 1.4. *Example of an anisotropic dataset*

The problem related to the anisotropy concerns working on the discussed volume as if it was isotropic, and consequently getting fake results. Actually, most of the pre-operative planning/CAD software are based on an isotropic coordinate system and dataset handling environment. As a consequence, measurements computed on slices visualized in these software, achieved from an anisotropic volume, may carry on an imprecision: this is due to the fact that the user measures in relation to what is shown, but the software provides a measurement value in regard to its own isotropic coordinate system, that does not correspond to the anisotropic volume one. The implied imprecision, that can reach significant values, is inversely proportional to the angle between the measurement direction and the volume/dataset vertical axis (Fig. 1.5). This is due to the contribute of the pixel sized dimensions of the voxel (length and width) that is greater the more the measurement direction tends to be orthogonal to the voxel height axis.

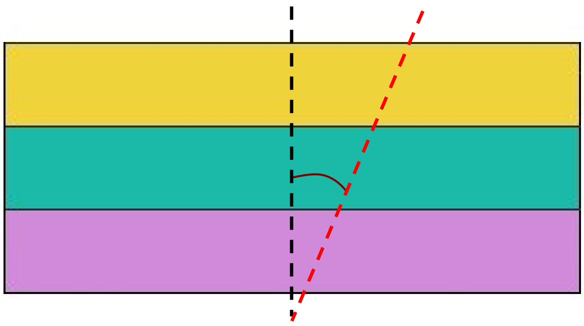

Fig. 1.5. *Angle between slices height axis (black) and measurement direction (red)*

The anisotropy systematic effect implied on a measurement can be calculated as follows:

$$M_s = I - P$$
$$S_s = \cos(\alpha)^2 * M_s$$
$$S_L = S_s * (L \div I)$$

Whereas P is the pixels-size value, I is the interslice one, α represents the angle between the measurement direction and the volume vertical axis, and L corresponds to the expected measure. Once calculated the maximum systematic effect over a slice height M_s, it is possible to obtain the real systematic effect implied over a slice height (S_s), and consequently also over a specific measurement (S_L).

1.3.3 INCORRECT WORKING PLANES

In Section 1.3.1 it has been explained the common multi-view context (DentaScan, GE Medical System) and some weak points in it. In addition to what described, there is a quite relevant fault that needs a separate description. This problem concerns the possibility to imply a significant imprecision into the measurements computed on cross-sectional planes, which are the cut planes actually used to plan (Sansoni 1999; Cucchiara et al. 2004). The cross-sectional images are not parallel each other, and converge at an accumulation line containing the accumulation point where teeth axes, in their turn, converge at (see Fig. 1.6). On these images fundamental data for endosseous implants installation are achieved.

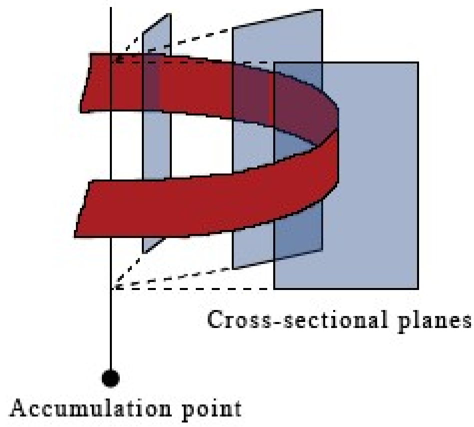

Fig. 1.6. *Cross sections converge at accumulation line (above accumulation point)*

An example of an essential measure is the bone thickness, due to the implant insertion through bone drilling, in order to perform a stable placement of the fixture and allow a good osteointegration. As mentioned before, cross-sectional images, that the software achieve through the use of interpolation algorithms, may imply a significant lack of precision on measurement computed on them: in fact, the cross-sectional plane is almost always not perpendicular to teeth axes, due to natural causes, unless the acquisition transaxial plane is perfectly orthogonal to the tooth axis of interest. However, even in that case, the cross-sectional image would be correctly parallel to that tooth axis only, and in case of a completely or partial edentulous patient, different cutting planes should be reconstructed nonetheless (one for each needed implant). Actually, due to this angle ϕ between the cross plane and the tooth axis of interest, on the provided image lies only a part of the tooth itself.

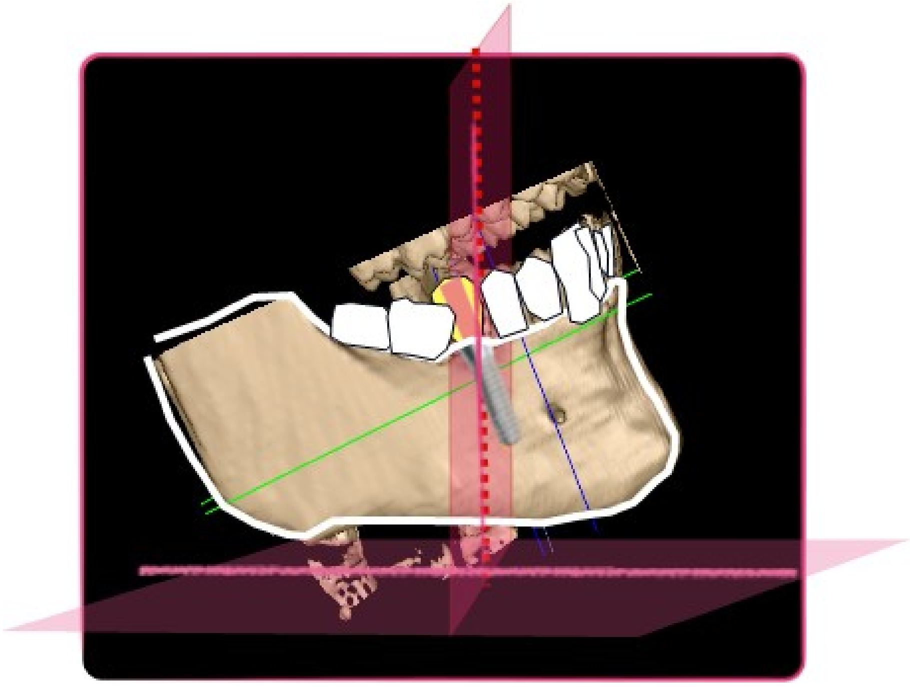

Fig. 1.7. *Cross-sectional plane (vertical) orthogonal to the axial one (horizontal)*

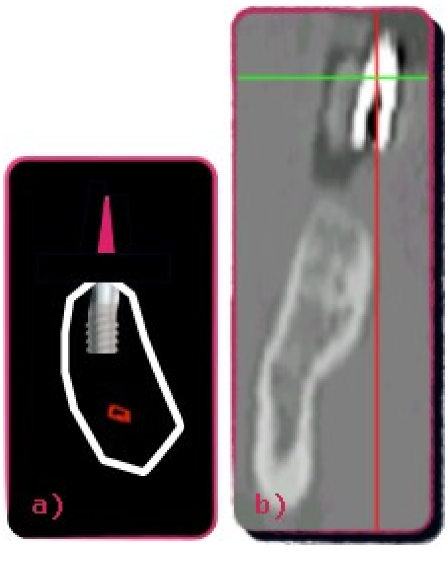

Fig. 1.8. *a) oblique cut of the axis of interest and b) a common cross cut plane*

As a consequence, measures achieved on these images carry on an imprecision, that is inversely proportional to the mentioned slope angle:

$$E = 1 \div \cos(\phi)$$
$$M' = M * E$$

Whereas *E* represents the slope distortion effect, *M* is the expected measure (or the length of the object to be measured), and *M'* is the measurement result. In Fig. 1.9 it is shown the relation between the angle ϕ and the obtained measure.

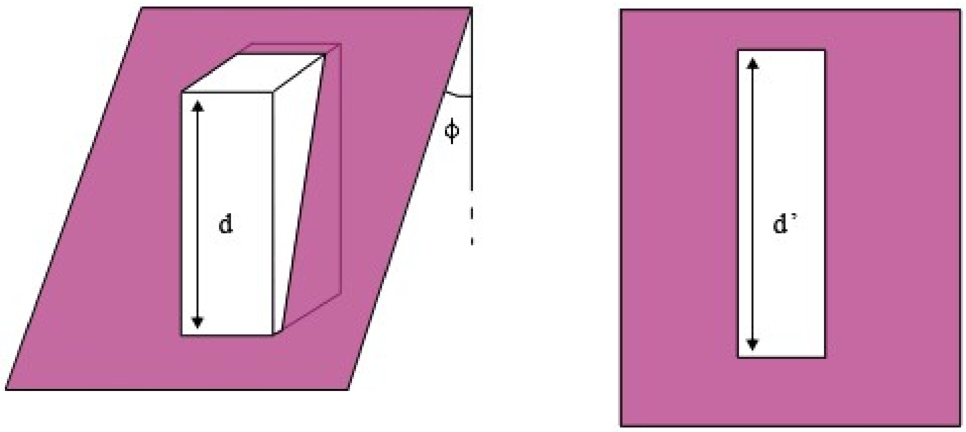

Fig. 1.9. *Cross plane slope angle and wrong measurement result d'=d*(1÷cos(ϕ))*

As reported by Sansoni (1999), it has already been demonstrated in literature that CT images are affected by a distortion and that it may consequently lead to negative effects during the surgical act. Talking back about the bone structure thickness measurement, if the measure obtained was not correct, the surgeon could risk to break through the bone during implant insertion (the error tolerance in these cases is quite less than 1 mm), possibly injuring sensitive nerve tissues seriously, prejudicing facial muscles control as a result.

The described problem could be handled using specific centering tools/ad hoc radiological stents to help the radiologist to align the acquisition transaxial plane orthogonally to the tooth axis of interest (CentraScan®, Era Scientific;). However, even if this procedure could be feasible for every radiology study, it would solve the problem for one tooth axis only, implying the need of a different CT scan of the patient for each tooth axis of interest (as mentioned before).

1.3.4 LACK OF ANATOMIES AUTO-IDENTIFICATION

When using pre-operative planning software in order to guide the following surgical act, it is always important to care about relevant related anatomies. Often, carelessness of these anatomies can cause consequences so serious that it appears vital to these kind of software to give them the right importance and to help the doctor to take them into consideration. In oral implantology the most relevant anatomy to care of, and based on which the planning has to be, is the *mandibular nerve* canal.

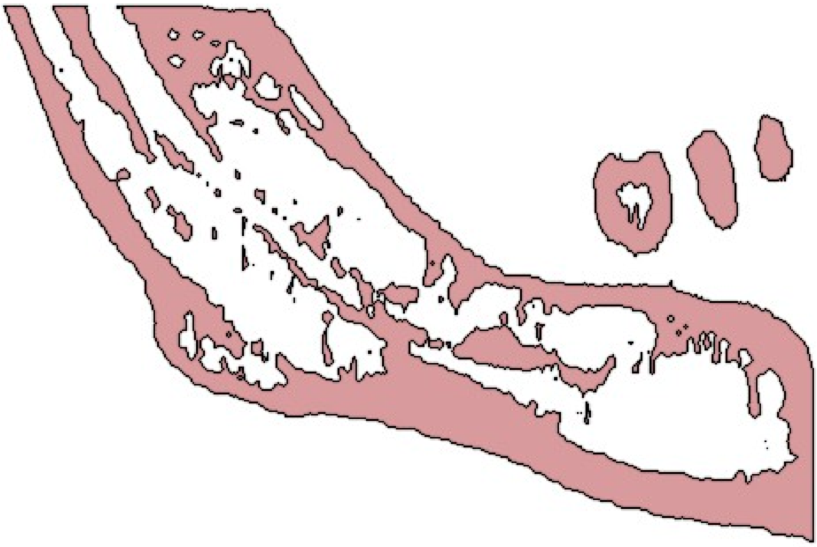

Fig. 1.10. *Mandibular nerve canal (second white canal from top-left)*

As mentioned in Section 1.3, an important deficit of common planning software is the lack of automatic identification of these kind of anatomies, and, in case of oral implantology, this lack involes the mandibular nerve recognition. Actually only a few pre-operative planning software for oral implantology are able to highlight the *mandibular canal*, and, to the best of the acquired knowledge, none is provided of an automatic feature. When the canal identification feature is present, it is purely manual: it works through interaction of the user to spot points along the slices of a view (generally the cross-sectional one), and finishes drawing the canal following the determined path. Whereas this procedure is surely good and needed, it is preferable to additionally provide an automatic algorithm, in order to assist better implantologists that have lesser computer use capabilities, improving the software safeness in general.

1.3.5 GOALS SUMMARY

In conclusion, as emerged from the contextualization of the general planning software defects in regard of oral implantology, in my PhD career I have faced the following problems:

1. Misleading work context: most of the state-of-the-art planning software for oral implantology are based on a common 2D multi-view environment. The Panoramic view, part of this work context, cannot be used to accomplish correct measurements, due to its construction nature, but it is present nonetheless, consequently leading to planning imprecision. Moreover, even when a 3D dedicated view is present, usually it is not fully integrated in the 2D work context, remaining unused, whereas the planning is achieved on the 2D multi-planar only.
2. Unhandled volume anisotropy: very often, CT datasets provided by the radiologist to the implantologist have an interslice value (the space between a slice and the one stacked immediately after) different from the pixel size one (the minimum picture element on the slice plane). When the slices are stacked to construct a 3D dataset (or volume), this results to be anisotropic, having the voxel (minimum volume element) shaped as a parallelepiped instead of a cube. Then, during the planning, when user measures sections of this volume, the resulting measurements are affected by a possibly significant imprecision, because of measure computing in an isotropic coordinate system on an anisotropic volume.

3. Unreliable cross-sectional planes: among the various views of planning software work context, cross-sectionals are the most important in regard of implant positioning. This views are achieved through an interpolation reconstruction orthogonal to both the axial plane and the panoramic curve, but almost always they are not parallel to teeth axes of interest. Consequently, whenever a doctor accomplishes the needed planning on the cross-sectional view correspondent to the tooth axis of interest, it will follow an error on the related computed measurements. This happens because the interesting area will go through the cross-sectional obliquely, resulting to be incomplete in the related cross-sectional view showed to the user. This problem could be solved asking to the radiologist a CT scan with the trasaxial plane orthogonal to the tooth axis of interest, in order to achieve cross-sectional planes parallel to the tooth axis one. However, this is not an acceptable solution, because usually these cases of study involve more than one tooth of interest, and, to proceed in the described way, it would need a different CT scan for every tooth axis of interest.
4. Lack of mandibular canal automatic recognition: rarely state-of-the-art software in commerce are able to provide functionalities to highlight the inferior alveolar nerve canal, that is fundamental for oral implant planning. When they do, however, is usually through a significant interaction of the user, exploiting manual identification. An automatic recognition feature, instead, is almost always absent from oral implantology

planning software, whereas it would be desirable. Indeed, an automatic tool able to correctly identify the relevant anatomy would significantly help the doctor, speeding up the planning and avoiding resolution-related difficulties in regard of spotting the area of interest, as well as preventing manual identification errors.

Thus, I developed and applied several methodologies and algorithms in order to solve the described problems. The adopted solutions are reported and explained in the following chapters. In Chapter 2 is described the overall approach and the framework that has been opted for, in order to have a reliable and optimized fully 3D work-context, including the technology used and the most important features implemented in. The algorithm developed aiming at correctly handling the anisotropy datasets, together with its evaluation, is reported in Chapter 3. Chapter 4 shows the solutions, both manual and automatic, adopted to manage the construction of multiple correct cross-sectional working planes, plus further related functionalities implemented; at the end of the chapter, evaluation and validation of the described features are reported. In Chapter 5 are explained the procedures developed in order to both manually and automatically recognise the mandibular canal, as well as their evaluations. The completion of the global approach is reported in Chapter 6, in regard of the interfacing of the software with a robot able to produce a surgical guide based on the accomplished planning. Finally, Chapter 7 lists related work, whereas conclusions about the doctorate activity are reported in Chapter 8. References and publications end the dissertation.

CHAPTER 2: FULLY 3D SOFTWARE

Almost all the oral implantology planning software in commerce provide a common frame of work, strongly based on the pioneering one (DentaScan, GE Medical System). This work context has been analyzed and discussed in collaboration with dentists and implantologists, in order to understand if it could be optimized and to possibly identify lacks and defects. It emerged that, as it is, it results to be misleading and not planning focus optimized, due to the deceiving projective nature of the panoramic view and its intrinsic low importance, apart from being usually bonded to a two-dimensional model, confining the 3D view to a conceptually and practically parted environment (see Section 1.3.1).

2.1 PROPOSED APPROACH

With the purpose of improving and optimizing the planning software framework, it has been necessary to define the whole approach involved, in order to be sure of being able to spread the expected optimization and improved safeness in each procedure phase, without loosing the improved precision before to reach the surgical operation.

With the described intention, it has been designed a fully three-dimensional approach, that starts from a CT scan (whereas images are in DICOM format), presents to the planning doctor the 3D surface rendered model and the needed computer-aided design (CAD) implant models, and finishes with the planning driven surgical act, keeping the coordinate system always in the same dimensional level. The user can therefore plan and simulate in a precise and reliable 3D virtual environment the setting of the most suitable implants for the corresponding 3D volume (Chiarelli et al. 2009a; Chiarelli et al. 2009b; Chiarelli et al. 2010a; Chiarelli et al. 2010b). In regard of this, it has been prospected the possibility to have relevant axes in the 3D volume, in order both to help the doctor to identify the best planning planes (see Section 1.3.3) and to provide a physical reference frame to the software. Concerning this, it has been exploited the same method described by Cucchiara et al. (2001) by executing the CT scan on a patient wearing a radiological mask with radio-opaque markers. These markers are installed in the stent following the dentist prosthetic pre-planning, and they usually represent the best directions for the final implants, anatomy impediments apart. This technique is adopted in the 3D environment especially in order to have relevant axes (i.e., those of the positioned markers) correctly and univocally identified in the 3D volume, but not only. Actually, apart from the pre-planning installed markers, two other ones, parallel each other, can be set into the outer part of the radiological stent, providing a physical reference frame inside the software 3D virtual world. This can be useful in order to univocally identify the axes of the implants planned in the 3D space, as well as their angle and depth, to transfer the planning into a surgical mask to be used during the surgical act, and therefore to avoid human mistakes in implants insertion into the bone structure. The overall approach is shown in Fig. 2.1, and it can be summarized as follows:

- during the CT scan, the patient wears a radiological mask with radio-opaque markers, to have relevant axes in the 3D space;
- 3D Environment processing is exploited for implant planning;
- for each planned implant (characterized by a position, orientation and depth), a surgical guide can be made, by properly interfacing the 3D environment with an anthropomorphic robot able to drill the surgical mask along the computed direction e for the computed depth.

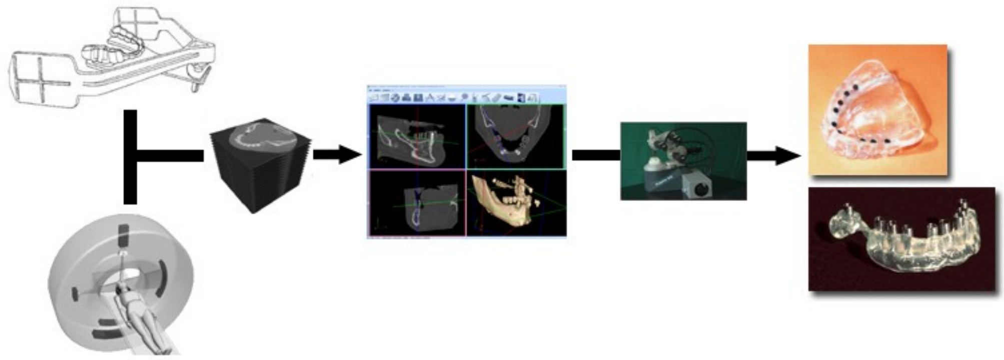

Fig. 2.1. *The proposed approach*

2.2 PLANNING ENVIRONMENT

The first step of the pre-operative planning approach consists of loading from the integrated database a case of study, which has been previously added through a built-in DICOM set importer. The proposed methodology, differently from the usual DentaScan multi-view one (SurgiCase® and SimPlant®, Materialise; Cucchiara at al. 2001; DentaScan, GE Medical System), aims at optimizing the planning operation giving the implantologist a reliable 3D environment to plan on. The whole system does not follow the common multi-view interface, which takes in consideration a bunch of 2D images context of work plus a 3D one reconstructed ad hoc (SurgiCase® and SimPlant®, Materialise; Cucchiara at al. 2001). It has been avoided this user interfacing approach due to the psychological and practical separation induced on the user and the implied lacks and difficulties of compatibility between the different contexts. Instead, the tool here discussed provides a 3D environment, based on a built-in graphic engine, achieving the multi-view interface through the use of different cameras looking the same 3D object. The context of work, then, is completely integrated, and allows to work and plan on every view, being able to see modifications in real time on each other view.

The developed application has been implemented for the Windows O.S. (XP/Vista/7) and tested on a PC with a Pentium D 3.00 GHz

CPU, 2 GB of RAM and 512 MB of VideoRAM. The software is written in C++ with the support of the following libraries:

- DCMTK© (OFFIS e.V.) to handle DICOM images;
- MITK 2.0 (Prof. Jie Tian and Medical Image Processing Group, Institute of Automation, Chinese Academy of Sciences) to manage the three-dimensionally reconstructed radiographic volume;
- MFC and ProfUIS 2.90 for the frame graphics;
- SQLite for the database to store imported study cases
- HDD/USBPhysic and zlib© (Jean-loup Gailly and Mark Adler) for devices control;
- OpenGL for the graphic pipeline control and the rendering in general.

2.2.1 GRAPHIC USER INTERFACE

The framework is fundamentally composed by two main graphic elements: a toolbar to advance in the planning procedure and to use the provided features, and the four views on the 3D world (see in detail in Section 2.2.2). Every view, in turn, presents only a sidebar, that can be a scrollbar or a threshold control depending on the view function. The results is a very simple, easy, and immediate user-friendly interface. This outcome has been looked for on purpose, aiming at simplifying the doctor planning, and consequently assuring more operational safeness and less faults due to misunderstandings.

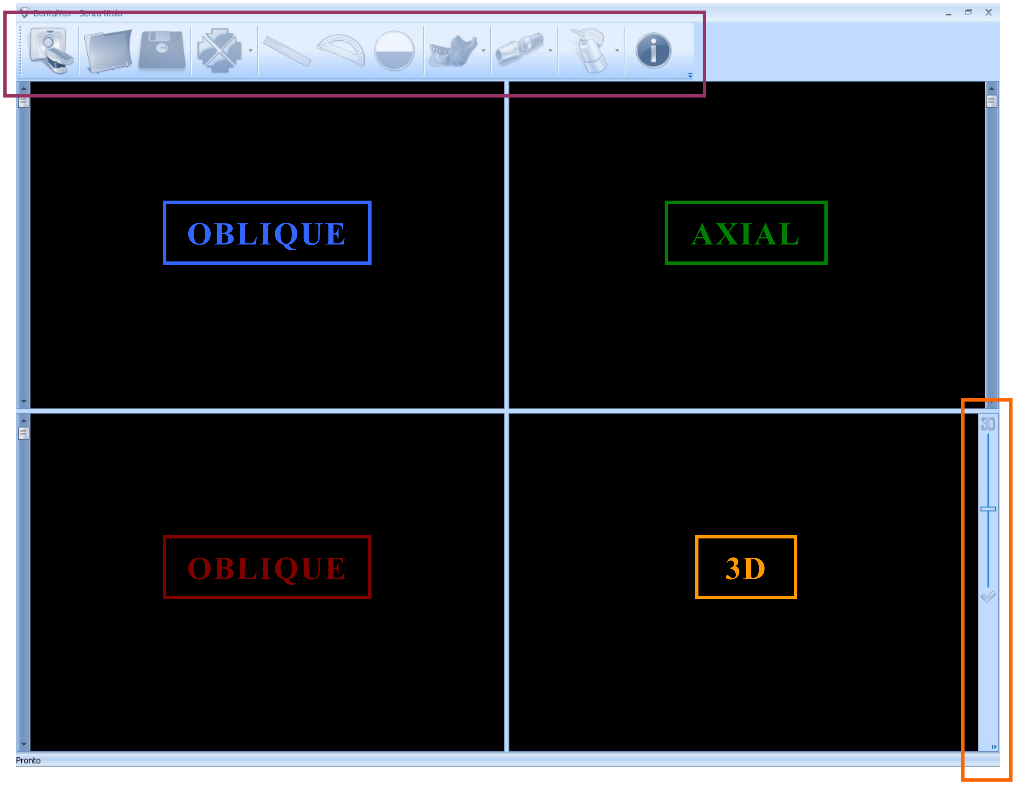

Fig. 2.2. *Two interface toolbars: main (purple) and 3D one (orange)*

Parting from the common oral implantology planning software work context, it has been decided to include three kinds of views: axial, oblique, and 3D. Whereas the panoramic view has been removed for the previously mentioned disadvantages, and the axial one has been kept for its importance (see Section 1.3.1), the three remaining views are divided in two oblique ones and a 3D one. The oblique views are actually dedicated to the cross-sectional images, as the common approach ones, but with the great difference that the discussed limit of orthogonality has been removed (see Section 1.3.3), and consequently their measurement faulting as well (see Chapter 4). Finally, the 3D view has been integrated in the main window frame to provide the three-dimensional sensation of planning, providing the sense of comfort given by the reality dimensional level.

2.2.2 3D VIRTUAL WORLD

The developed work environment parts from the common two-dimensional multi-planar one, and it focuses, instead, on a 3D setting. This has been achieved using a single 3D virtual world, and managing the views in order to allow the user to navigate it. Every view is achieved through a mobile camera in the environment, starting in a determined location and watching in a distinct direction. Each view has, moreover, a camera filter that defines the kind of lens: if it is an axial or an oblique camera, the filter will set a particular set of clip planes, in order to reproduce the slice effect, and visualize the proper slice as texture placed in front of the camera lens. In addition, the filter determines also the rendering techniques for the objects in the scene, in order to enhance their visibility and identification. As a consequence the user may navigate the radiographic dataset and visit the world using these cameras: the allowed operations are the cameras ones typical of CAD software, like panning and zooming, or the trackball rotation for the 3D view in specific. Moreover, the axial and oblique views sidebars allows to scroll the cut planes along the view’s depth axis, whereas in the 3D one there is the control bar to set the threshold for the three-dimensional reconstruction of the bone model.

The whole 3D engine, that is the base of the software technology, is built-in and it has been developed on purpose. Everything, from a 3D point definition to an object slide movement, from the shading to the texture management, from the coordinates converting functions to the visualization modes, is managed by the realized kernel. However, in relation to the focus of the research objectives, and in consideration of the extent of the engine characteristics, in the following paragraphs its main features are described, avoiding to report the whole kernel code base, in order to focus on the most interesting technologies used and functionalities implemented.

VISUALIZATION AND RENDERING

In order to improve items identification and visualization, two different types of rendering have been implemented. The radiographic filter allows to reproduce any cut plane of the axial dataset: this has been achieved using the interpolation methods provided by the MITK library (see Section 2.2), responsible for the radiographic volume handling in general, and producing textures properly attached on the view's camera lens. The toon shading-line rendering technique (plain coloured polygons without lighting effects, plus highlighted boundary edges), instead, strongly enhances objects silhouettes, emphasizing them over a complex background. The first visualization mode combines the radiographic filter with the toon shading-like rendering technique in order to optimize the planning upon axial (upper right in Fig.2.3) and oblique views (upper and lower left in Fig. 2.3). In addition, notice that, in the status bar (the bottom border of the software main frame), a panel shows in real-time both the mouse cursor correspondent position within the radiographic volume and the related Hounsfield density value, with the intention to provide a wider knowledge of the area currently hovered.

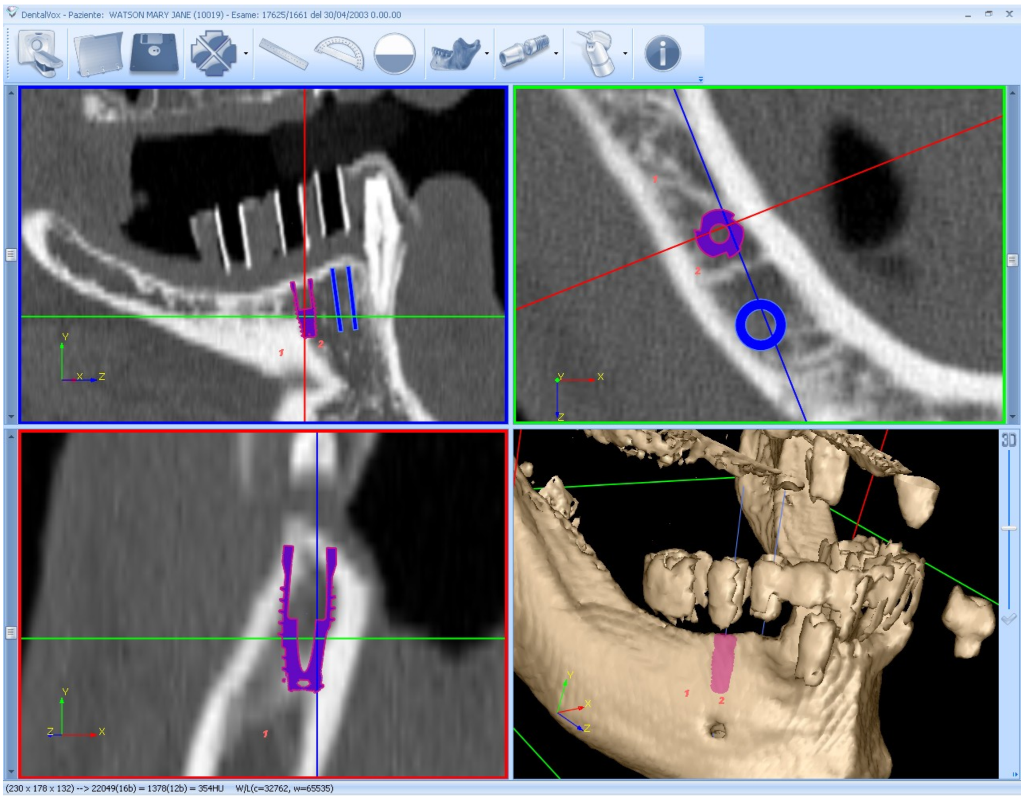

Fig. 2.3. *Visualization modes: radiographic (top, down-left) and 3D (down-right)*

The second visualization mode, instead, is used in the 3D view, and it renders the reconstructed bone model, plus every other possible item in the 3D world, using an automatic Gouraud shading (Gouraud, 1971) calculator method that has been implemented in the kernel on purpose. Moreover, with the aim of correctly managing and optimizing models transparencies and overlapping, every rendered object is processed by the developed engine sorting pipeline, before to be passed to the OpenGL one.

ROTATIONS

Another relevant built-on purpose feature of the 3D engine is the rotation system. It has been started from a common rotational system based on Euler angles, due to their immediateness and ease of implementation. However, as reported by Hughes (unpublished), Euler angles have important drawbacks:

1) Ambiguity: the rotation sequence is critical (e.g. a XYZ rotation sequence is very different from a ZYX one); due to the lack of an industry accepted standard rotation sequence, there is an inherent risk of mistaken assumption of rotation order in performing analysis and communicating using Euler angles.
2) Singularities: any set of Euler angles in which the second rotation aligns the axes of the first and third rotations causes a singularity. For an Euler Rotation Sequence where the first and third axes are the same, called a repeated axis sequence, singularities occur for second rotation angles of zero and 180 degrees; for non-repeated axis sequences, singularities occur at +/- 90 degrees.

In relation of these considerations and the need of complete freedom of movement and relocation both in oblique slice definition (see Chapter 4) and 3D camera trackball movement, it has become necessary to change the rotational system into a more suitable one: a quaternion rotational system. The quaternions have been formulated by Sir William Rowan Hamilton in 1843, as an extension of complex numbers, starting from an Euler's theorem that states that the most general displacement of a rigid body with one point fixed is a rotation about some axis. The quaternions are a noncommutative number system defined by Hamilton as the quotient of two directed lines in a three-dimensional space or, equivalently, as the quotient of two vectors. In detail, Hamilton described a quaternion as an ordered quadruple (4-uple) of real numbers, and every element of H (the *Hamilton* algebra of quaternions) can be uniquely written as a linear combination of four basis elements:

$$q_1 1 + q_2 i + q_3 j + q_4 k$$

whereas q_1, q_2, and q_3 are real numbers, and i, j, and k are literals. Sum and product of two quaternions are defined in consideration of the following relations:

$$i^2 = j^2 = k^2 = ijk = -1$$

that, in turn, imply the following relations:

$$\begin{aligned} ij &= k, \quad ji = -k, \\ jk &= i, \quad kj = -i, \\ ki &= j, \quad ik = -j. \end{aligned}$$

In particular, notice that quaternions form a four-dimensional normed division algebra over the real numbers. Furthermore, they can also be represented as the sum of a scalar and a vector. Actually, a quaternion $q = q_1 + q_2i + q_3j + q_4k$ can be described as the pair (q_1, v), whereas $v = (q_2, q_3, q_4)$ is a vector in $\Re^3$. Thus, considering the Euler theorem previously mentioned, it is possible to define a quaternion as the pair (*rotation angle*, *rotation axis*):

$$
\begin{aligned}
q &= (q_1, \quad q_2, \quad q_3, \quad q_4) \\
q_1 &= \cos(\phi/2) \\
q_2 &= e_1 \sin(\phi/2) \\
q_3 &= e_2 \sin(\phi/2) \\
q_4 &= e_3 \sin(\phi/2)
\end{aligned}
$$

with the requirement of $|q| = 1$. Whereas e_1, e_2, and e_3 are the elements of the rotation axis unit vector $\hat{e} = \{e_1, e_2, e_3\}$, ϕ is the rotation angle, and q is the quaternion composed by the four Euler parameters q_1, q_2, q_3, q_4. In Fig. 2.4 is shown the quaternion rotation concept. The need of the four parameters (the 3D vector coordinates and the scalar value) is due to the insufficiency of three numbers to correctly represent 3D rotations. As reported in literature, an analogy is a two dimensional map of the earth: there is no way for which it is possible to map the surface of the earth without distorting either angles or areas. However, once the 2D map is wrapped round a 3D sphere it becomes linear, whereas it was not: in a similar way the 3D space of rotations becomes linear when it is mapped to a quad-dimensional (4D) hypersphere.

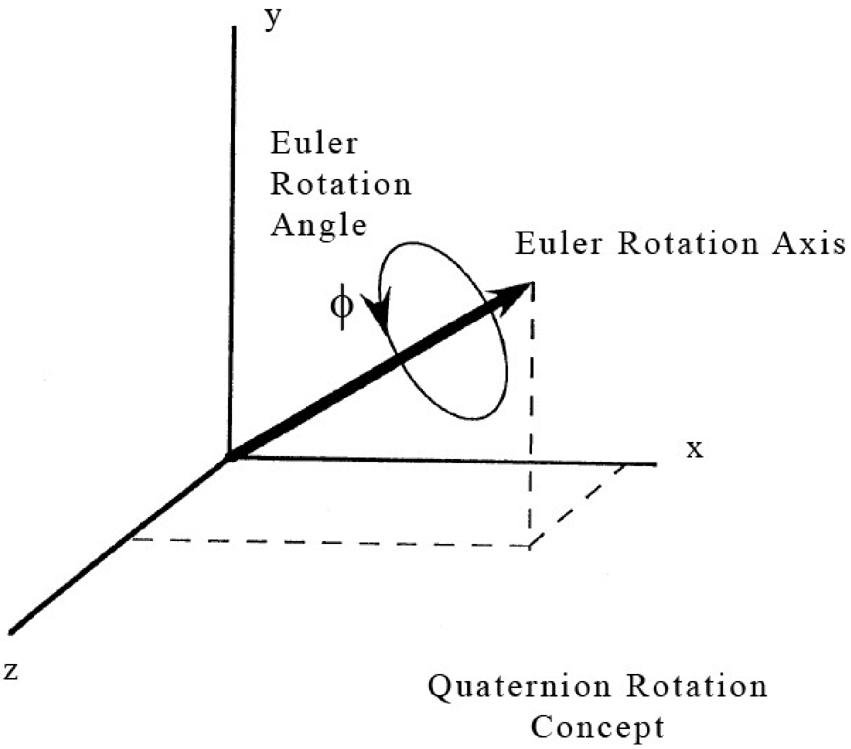

Fig. 2.4. *Quaternion axis-angle definition*

Indeed, notice that unit quaternions (quaternions with norm equal to 1), as the previous axis-angle definition one, when identified in $\Re^4$ form a 4D hypersphere:

$$S^3 = \{(q_1, q_2, q_3, q_4) \in \Re^4 \mid q_1^2 + q_2^2 + q_3^2 + q_4^2 = 1\}$$

In particular, using quaternions for three-dimensional rotations, as in 3D computer graphics, their 4D geometrical representation is an hemi-hypersphere (only half since opposite sides of the hypersphere represent the same rotation). Thus, following the quaternion arithmetic and functions, it has been developed from scratch a dedicated inner library. Using the quaternion rotations system implemented, it has been feasible to manipulate the rotation of the 3D view camera through a trackball control. In this way, it is possible to rotate the view around the 3D surface model of the bone structure located in the world center (positionally correspondent to the radiographic counterpart of the 3D reconstructed dataset).

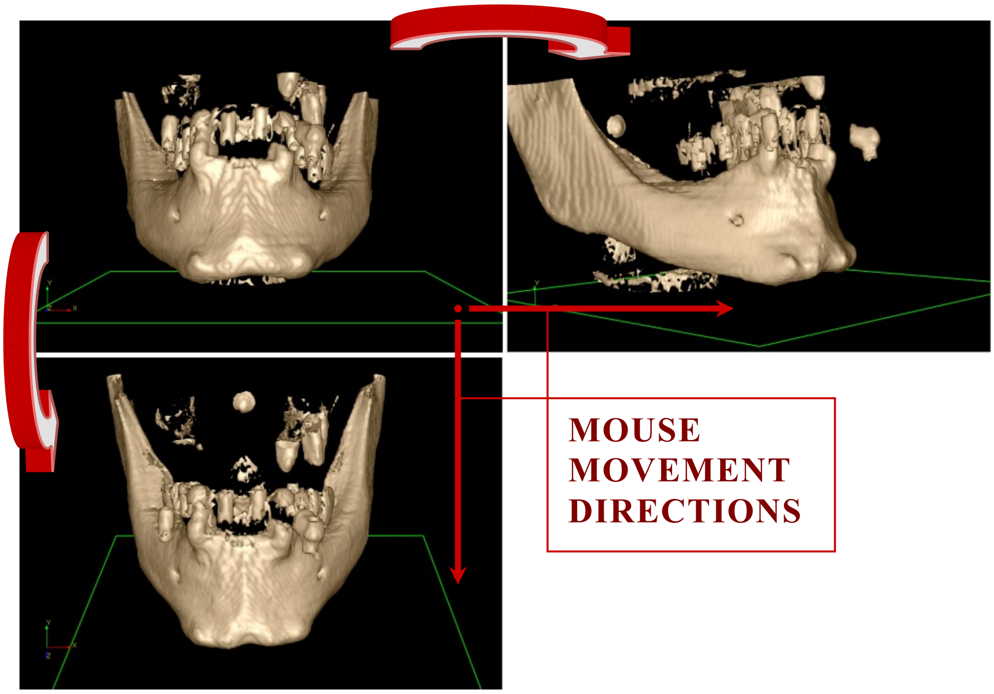

Fig. 2.5. *Quaternions powered trackball rotation*

3D BONE MODEL

The three-dimensional model of the bone is achieved starting from the radiographic dataset and applying a known algorithm of iso-surface extraction called *Marching Cubes* (Lorensen & Cline 1987), after having selected a desired threshold value from the view's sidebar (see for instance the model reconstructed with a threshold of 976 HU shown in Fig. 2.6).

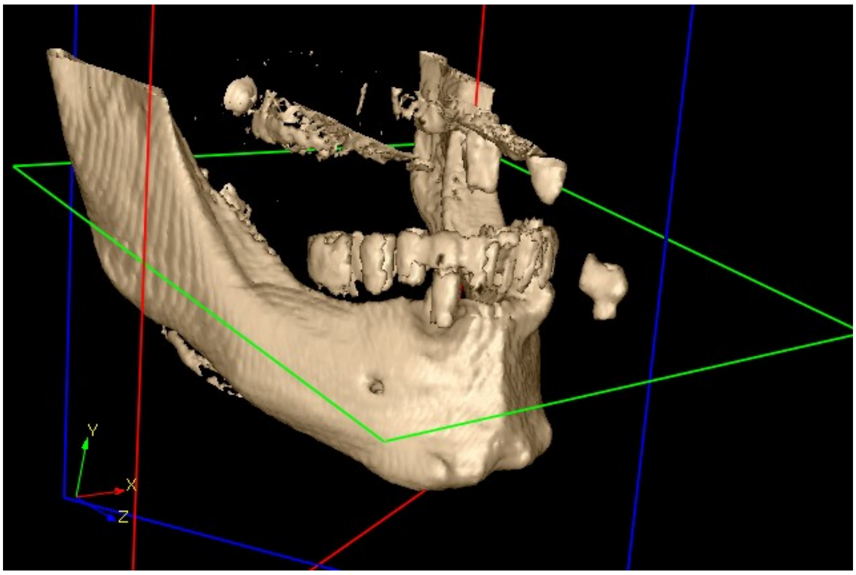

Fig. 2.6. *3D model of the bone structure*

This algorithm scans the dataset, slice after slice, and for every four adjacent pixels it builds an imaginary cube having these pixels as inferior face vertices, and the correspondent pixels in the adjacent slice as the superior face ones.

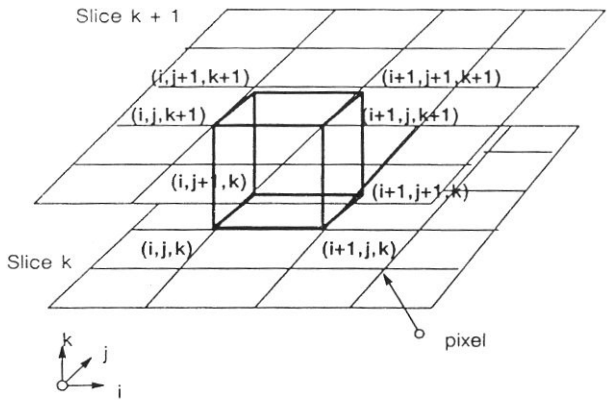

Fig. 2.7. *Marching Cube*

The next step consists of examining a cube, comparing the vertices density values with the selected threshold, and consequently understanding the inner surface shape using a pattern recognition system. Then, it passes to the next cube and repeat the procedure (therefore the name Marching Cubes).

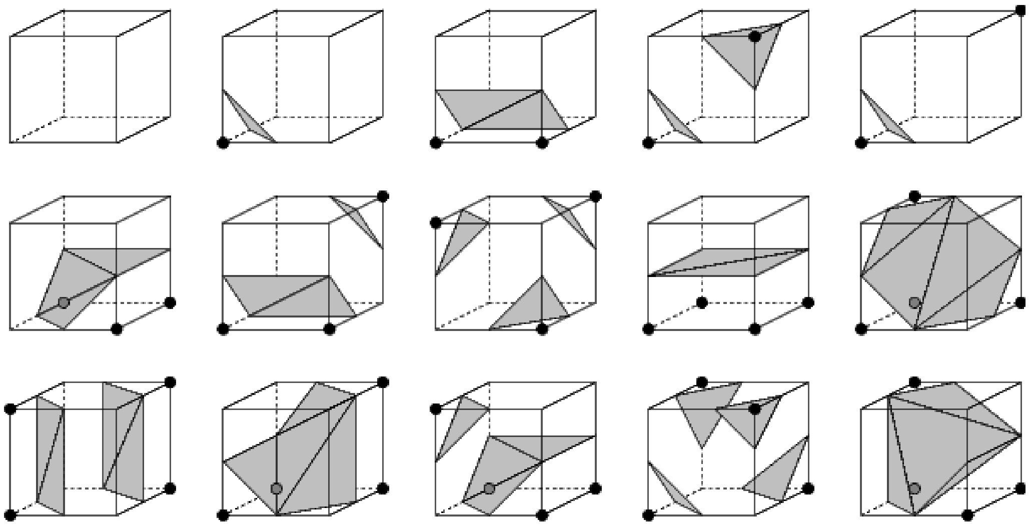

Fig. 2.8. *Representation of the 14 basic patterns plus void case*

Then the vertices interpolation points are calculated in relation to the surface shapes found, and the related surface triangular faces can be defined. The algorithm finishes providing the unit normal for each cube vertex, through normalization of the points density difference, and interpolating the achieved normal with every vertex of the related triangle.

MEMORY OPTIMIZATION

Setting the right algorithm parameters, the 3D reconstructed bone structure appears very accurate, although, on the other hand, it can slow down the application performances, due to the massive amount of vertices the 3D surface model is composed by. Thus, apart from selecting a parameters setting of compromise between quality and computer load, it has been necessary to find a way to speed up the software when operating with 3D objects in general. With this purpose in mind, it has been developed a meshes manager, a kind of active module which every request of 3D model memory loading has to pass through. This control manager, using a pointers/tickets system and sharing the same OpenGL context for all the views, is able to optimize the application performance, allowing to load in the video card memory every mesh only once and using the OpenGL display lists pre-compiled commands feature to significantly fast the rendering operations for repeated meshes, in addition of fastening the manipulation of 3D models composed by a huge number of vertices. As a consequence, also the use of many implant models becomes possible without feeling a significant performance decreasing, allowing the user to accomplish its planning easily (see Section 2.2.3).

ENHANCED INTERACTION

Therefore, everything the doctor may or would like to interact with, either an implant model or the mandibular nerve canal (see Chapter 5), is loaded into the 3D virtual world, the reference frame of which is centered on the 3D radiographic dataset. During the planning, it is possible to use the mouse device to interact with any kind of item loaded in the environment: the sliding and the rotations are easily achievable through an instinctive click and drag, whereas with the right focus on an object model the user has access to the inherent context menu and the consequent item-related permitted operations. Moreover, it has been implemented a selection state (with a related states management system), that, keeping an item selected, allows to slide/rotate it through the use of the keyboard. The main difference with the mouse counterpart resides in the accuracy of the accomplished movement: with this feature, in fact, it is possible to move objects with micrometre accuracy with the purpose to reach great precision, adding final touches after a preliminary positioning. Concerning the technology behind, in order to provide the described type of selection, it has been necessary to move on from the common projective picking, that is based on a sort of line projection into the field of view volume, starting from the viewport clicked point, and reporting every item touched along the path. This typical method can not work correctly with clipped objects: because of OpenGL pipeline functioning their cut part do exists nonetheless, and the items are consequently reported in the picking result list even if the objects have not been visibly selected. Hence, it has been developed an alternative selection methodology, that is based on the end-image color picking, being able to properly identify and distinguish every object in the scene. This feature can recognise an item class exploiting the view's colour back buffer, forcing every object to print its own reference ID over, instead of its rendering colour, immediately before the following buffer flush and the successive swap with the foreground one. Consequently the provided picking method correctly avoids clipped parts and identifies everything and only the user select by clicking.

2.2.3 IMPLANTS LOADING

As discussed in the Section 2.2.2, it has been taken in consideration the software need of being able to manage many 3D models. Actually, talking about oral implantology, and prosthesis surgery in general, and having the intention to provide a complete planning software, the possibility to insert in the environment and to manage implant 3D CAD models was a must. In consideration of this, two types of implant model loading have been implemented. Firstly, it has been supplied the option to load implant CAD models from file, in order to allow the dentist to work with the same implants types he/she is used to. In fact, several implants manufacturer provided the CAD models files of their real implants, with the intention of supporting the planning with their own ones, that have been gathered in file libraries accessible from the software.

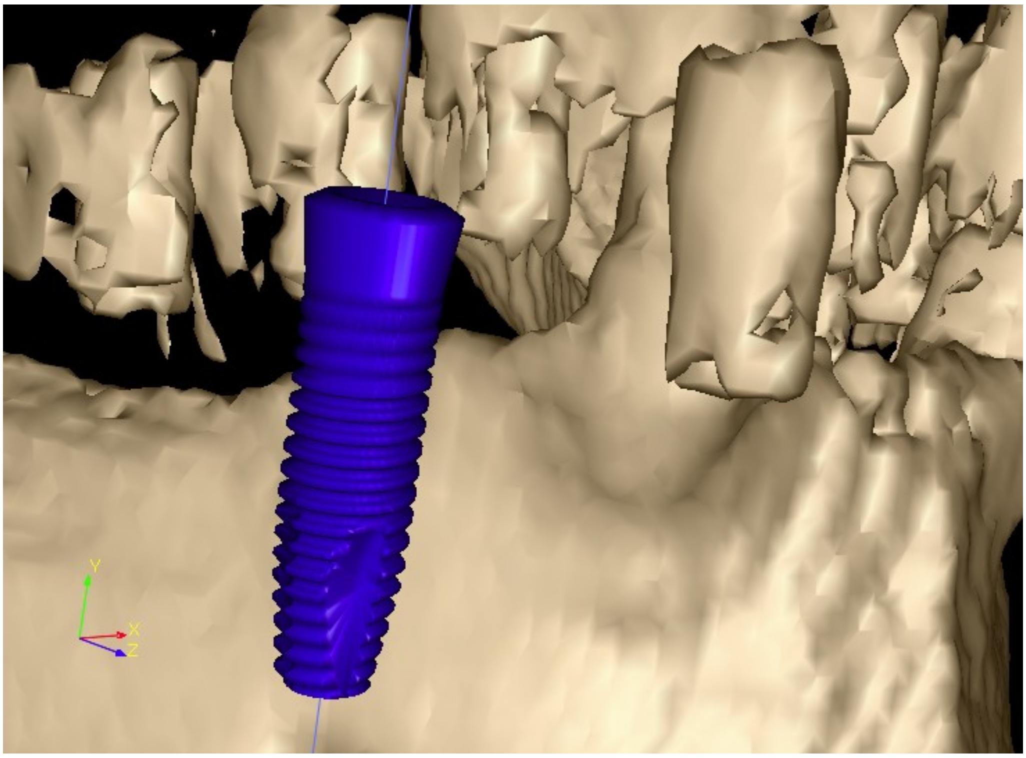

Fig. 2.9. *A 3D view rendering of an implant CAD model loaded from file*

In relation to the usual CAD file formats concerning implants models, it has been developed a file manager module, able to recognize the file format and to support the most common ones, like STL (Stereolithography) and PLY (Polygon File Format), both for the ASCII and binary versions, as well as to handle standard and not standard file headers. The second implant model loading type, instead, concerns the possibility to design custom models, with the purpose of giving the freedom to manage every planning need, even in absence of the right pre-built implant CAD model. This feature has been accomplished implementing an hollow cylinder automatic construction algorithm that will build the model on demand, using the parameters set ad-hoc by the user.

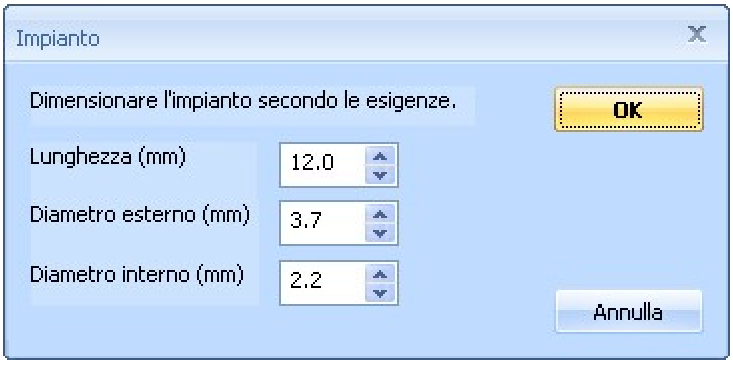

Fig. 2.10. *Custom implant model design window*

2.2.4 PLANNING MANAGEMENT

Once loaded implants into the environment, the doctor is able to move and place them, performing the desired planning. In this regard, the software offers a further feature: the option to keep track of the current planned implants. Actually, every operation on an implant in the virtual world dynamically updates its state, and consequently the software is able to know every detail about it at any moment. Thus, it provides at runtime the list of any current implant in the 3D world (see Fig. 2.11), informing about its updated position and orientation properties, and giving the possibility to center the views' cameras on it, in order to correctly check its surrounding area (for other related information, see Section 4.3).

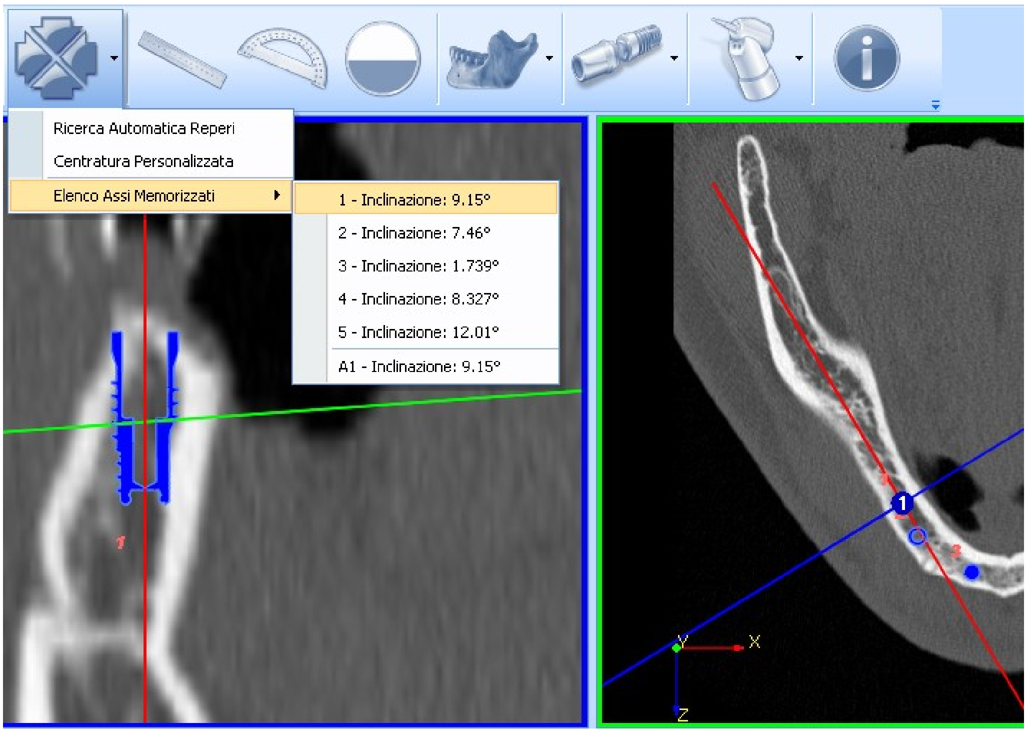

Fig. 2.11. *Implant centering from the dynamically up-to-date implants list*

It is interesting to notice that the feature to slide the views' cameras on a defined object/point is not strictly related to implants. Actually it has been implemented an utility of views synchronization, that allows the user to select any point in any view via mouse click in order to slide all the views' cameras to focus on the identified point, without changing their own orientation. Furthermore, also the centering operation, characterized by a change of orientation apart from the translation, is not necessarily bonded to implants. With the purpose of additionally easing the planning, in fact, it has been also added a feature that allows the software to keep track of the centering operations accomplished during the planning (see Chapter 4), to dynamically store them, and to provide them in a cascade menu list, giving the possibility to re-center, following the previously defined positions and orientations.

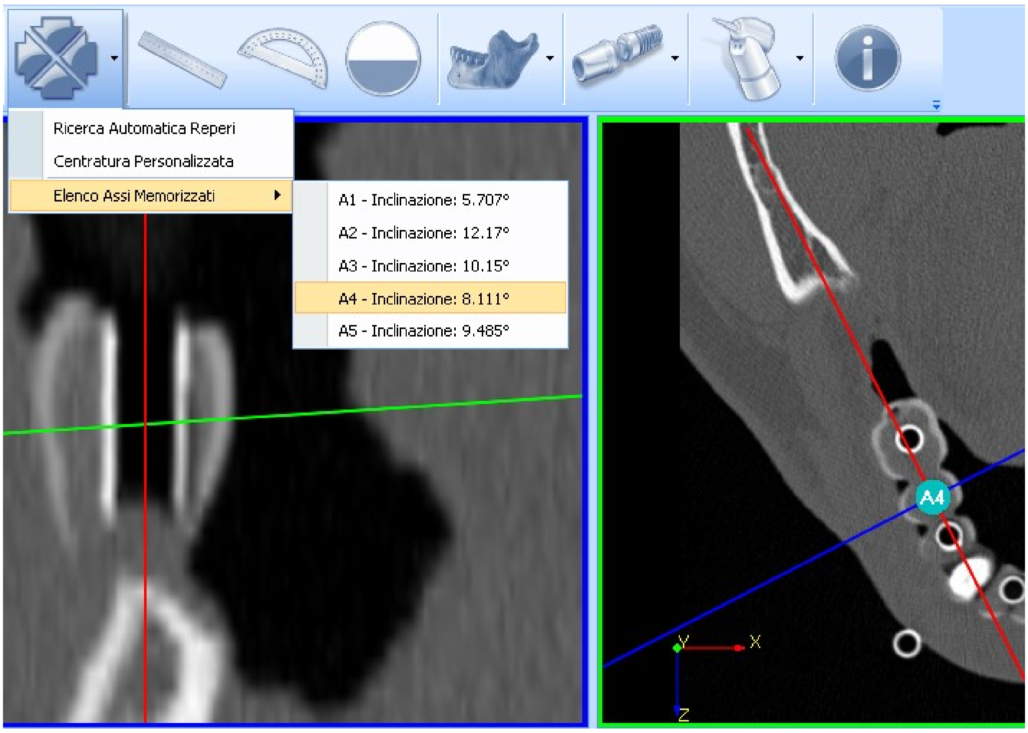

Fig. 2.12. *Selecting the desired one among the previously defined centering axes*

Thus, the software offers the utilities to achieve the work context to plan upon, although, to accomplish a surgical planning, there is also the need of tools able to support measurements. Actually, implantologists need fundamental information to operate in safety, as distances among implants and bone cavities or nerves. To this purpose and to take advantage of the correctness and precision of the provided work context and software system in general (see Chapter 3, 4), various mouse-controlled tools for measurements and visualization enhancement have been developed, like a ruler, a protractor, and a brightness/contrast modifier. Some sample measurements achieved with a measurement tool are shown in Fig. 2.13.

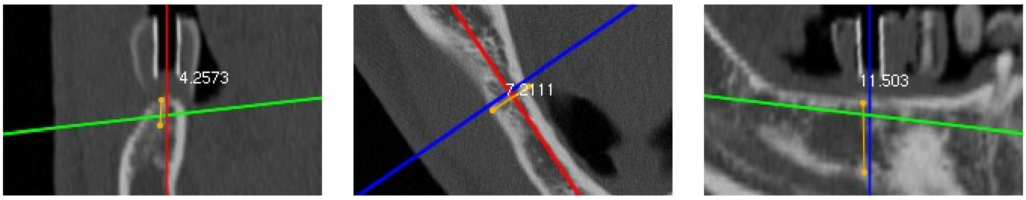

Fig. 2.13. *Example of measurements*

Finally, it has been decided to complete the software adding the option to save and share the planning. The saving option is needed to be able pause and resume the work, avoiding the discomfort of doing the whole planning in the same session or to loose it. This feature has been implemented following the usual software methodology. Then, the planning is saved into the application database using the common serialization method, which the whole 3D engine and software architecture have been designed compliant with. Concerning the sharing, instead, it has been thought to cover difficulty cases of study: the feature let implantologists to save their planning on an external file, allowing them to be able to send it to a colleague, in order to ask opinions about and/or corrections on. Thus, the functionality is divided in two parts, exporting and importing: whereas the first one copy the whole case of study, comprehensive of dataset and planning, into an external file, the second function allows to load the same file format, importing the loaded case of study into the software database. Concluding, for what concerns the technology behind, both these two utilities, as well as the saving one, works exploiting data binary serialization.

CHAPTER 3: ISOTROPIC WORK CONTEXT

In Section 1.3.2 it has been emphasized the spread problem concerning the lack of isotropy in common CT volumes, and the difficulty to obtain that requirement fulfilled in general. As explained, a difference between the dataset interslice value and its pixel size one implies a wrong correspondence of distances between real anatomies and an isotropic coordinate system, typical of software environments, and consequently an error in the measures computed on it. Actually, this systematic effect is proportional to the grade of parallelism the measurement direction has with the axial plane’s normal. Therefore, in consideration that in pre-operative planning, and oral implantology in particular, the doctor quite often plans and accomplishes measurements along the body vertical axis with a certain degree of slope, it is compulsory to solve this problem and provide a precise work context to compute measurements on.

3.1 TWO PASS INTERPOLATION ALGORITHM

With the purpose of achieving a reliable and correct environment to work upon, the software reconstructs the radiographic 3D volume under isotropic conditions, in order to have a cubic voxel as three-dimensional measure unit. This goal is obtained by interpolating the axial slices, acquired by CT scan, filling inter-slices void spaces and reconstructing the slices to fit the new height, till getting a pseudo-continuous radiographic 3D cube having dimensions multiple of the CT parameter pixel-size. In particular, the process consists of two main steps of interpolation of the axial volume.

3.1.1 FIRST STEP

Firstly, excluding the case of having an interslice value equal to the pixel-size one, it is calculated how many pixel-size high slices would fill the dataset interslice, taking in consideration only the integer part of the achieved value, and creating the correspondent number of pixel-size high slices for every interslice high slice. The redistribution of the voxels values is obtained with a simple interpolation of the original slice and the one over, uniformly changing the percentage of interpolation in relation to the amount of slices to create. Regarding this, the most significant contribution of each original slice is considered to be in its lowest part, leaving the intraslice space to be filled with new interpolated slices (see Fig. 3.2). In this way, if the original dataset interslice value is multiple of the pixel-size one, every single original slice have been expanded correctly, and the algorithm may stop.

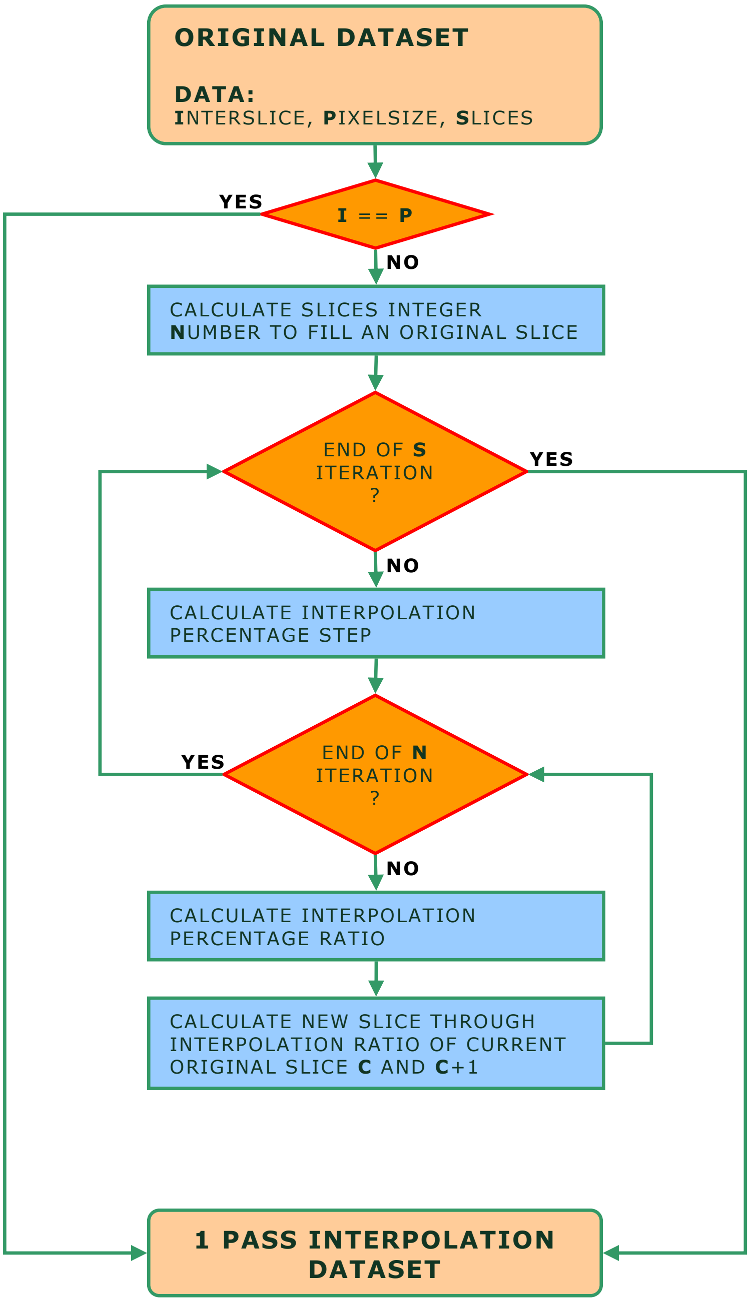

Fig. 3.1. *1st pass of the interpolation algorithm*

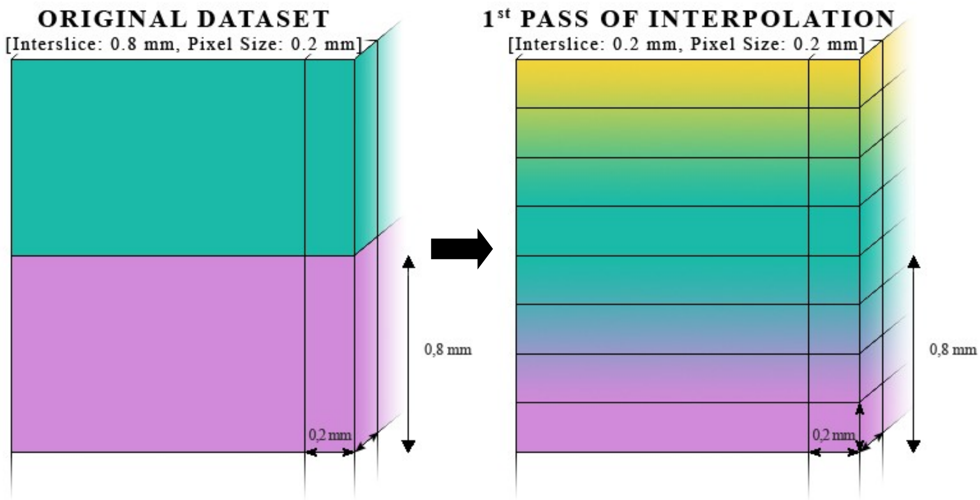

Fig. 3.2. *Example of slices integer filling and linear interpolation exploiting*

Otherwise, the overall volume is still not pixel-size formatted in height, although obviously quite more near to the isotropy than before. In this case, the interslice void spaces result to be filled with the maximum integer number of pixel-size slices, but it remains a bit of uncovered space for every original slice.

3.1.2 SECOND STEP

The second step has been added to solve this problem. It starts calculating the number of pixel-size high slices needed to bring the whole volume, created during the previous step, to have the same dimension in height as the original one, approximating to the nearest integer (the systematic effect implied by this approximation, or simply by the whole operation of interpolation, is discussed in Section 3.2, and evaluated, reported and compared in Section 3.3). Then, the volume is divided in blocks accordingly to the number of slices just achieved, and every block is interpolated, two slices at a time, to create the new block (see Fig. 3.3).

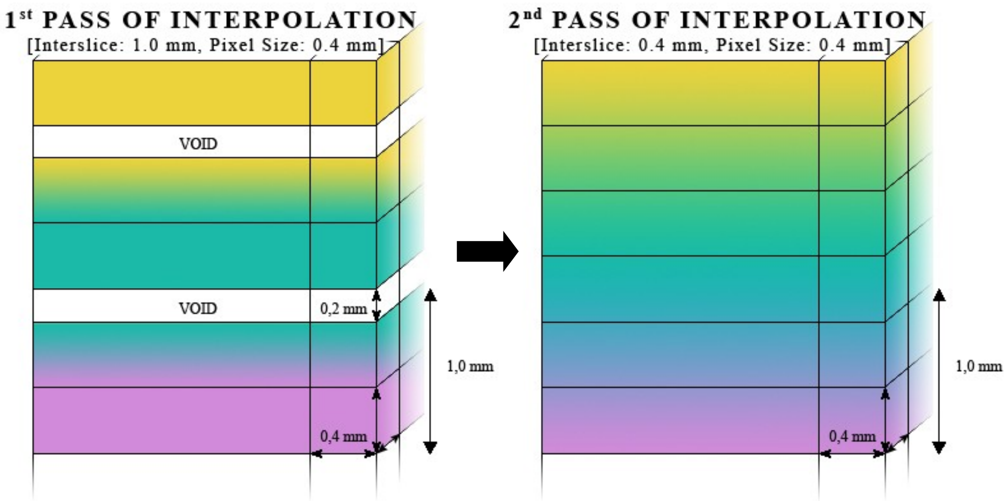

Fig. 3.3. *Example of a 5 slices block interpolated into a 6 slices new one*

This means that the slices are squeezed or stretched, using the appropriate percentage of interpolation, respectively to create space for the new one or to cover the space occupied by old ones, if any. The result of the second step is the uniform insertion or removal of slices into the previous volume, changing the slices to fit the new height, and achieving an axial volume having the same overall dimensions of the original one, but divided in height accordingly with the pixel size.

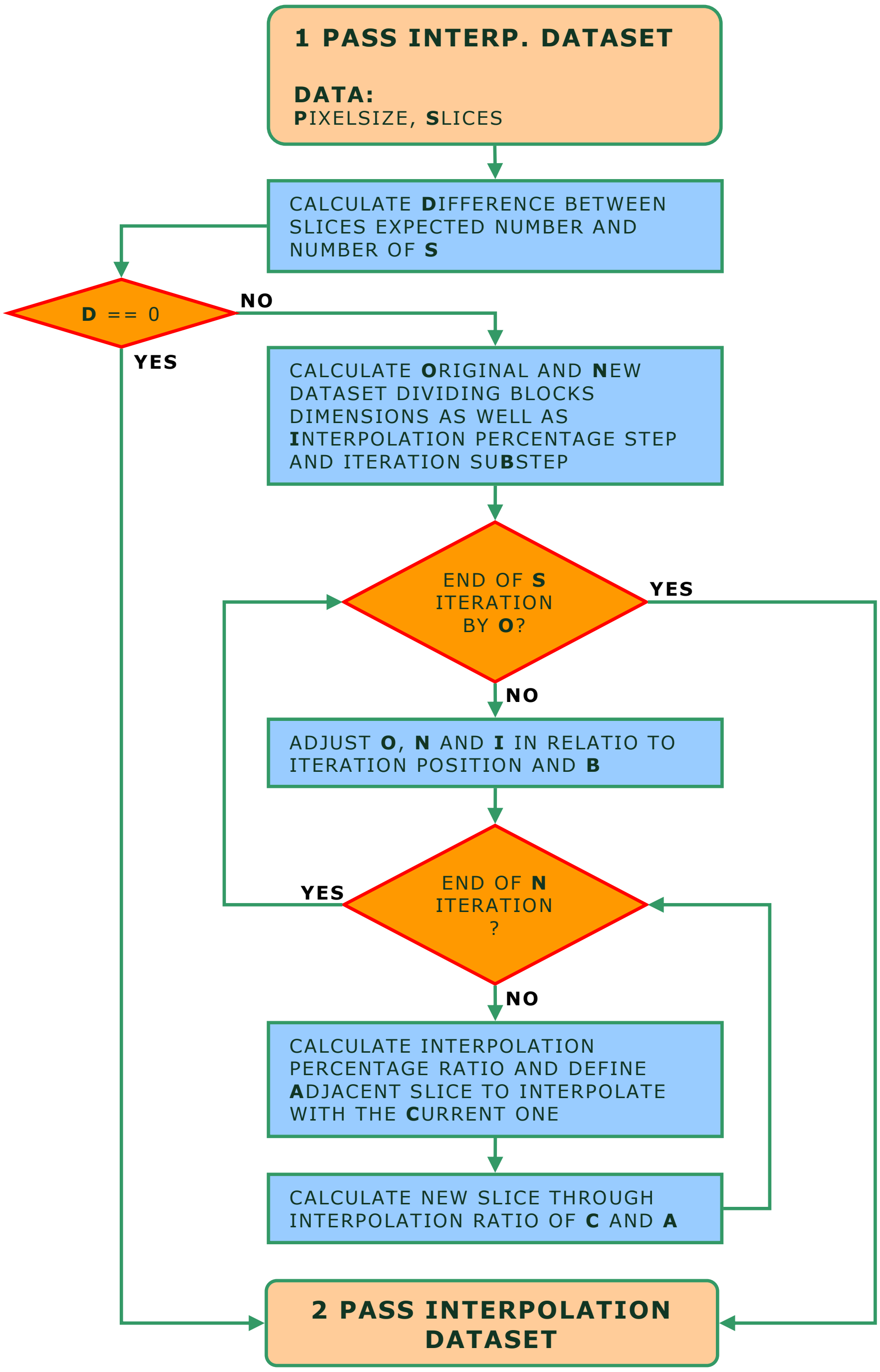

Fig. 3.4. *2nd pass of the interpolation algorithm*

In this way, it is possible to manage the three-dimensional radiographic volume without problems of anisotropy due to inter-slice values that are different or not multiple of the pixel-size one. Finally, that pixel-size is used as measure unit parameter of the software system, to manage correct measurements and proportions.

3.2 SYSTEMATIC EFFECT

It has been explained that computing measurements on anisotropic volumes in an isotropic expected environment leads to incorrect measures (see Section 1.3.2). As reported in the previous section, the problem is solvable through the use of interpolation based algorithms. However, even if the gain of precision is significant, the described solution can generate an imprecision nonetheless. This systematic effect (that, from now on, will be called improperly *error* only for the sake of brevity) may happen when the dataset interslice value is not equal or multiple of the pixel-size one. The problem is due to the fact that, after the application of an interpolation algorithm, either 1 Pass or 2 Pass one, the number of pixel-size high slices may be not perfectly contained in the dataset bounding box. This means that the height of the resulting volume would not correspond in millimetres to the original one, and consequently there would be a discrepancy in the following measurements.

The evaluation of the error implied by a particular interpolation algorithm can be realized as follows:

$$H_1 = N_1 * I_1$$
$$I_2 = P$$
$$H_2 = N_2 * I_2$$
$$D = H_2 - H_1$$
$$E = D \div N_2$$

Whereas *P* is the pixels-size value, and *H*, *N*, and *I* correspond respectively to the height of the dataset, its slices number, and its interslice value, with $_1$ being the reference to the original one and $_2$ the reference to the resulting one. The difference *D* represents the discrepancy between the datasets and consequently how much the resulting volume is stretched (positive *D*) or squeezed (negative *D*) in comparison to the first one. *E*, instead, is the sought error over the height of a single slice, being the volume discrepancy uniformly spread along its whole vertical axis. In this way it is possible to calculate the imprecision implied by the algorithm involved, and therefore to estimate the maximum error in computed measurements. As for the imprecision due to anisotropy, also in this case it is proportional to the slope angle between the volume vertical axis and the measurement direction, although significantly lesser than the first one (see Section 3.3).

3.3 ANISOTROPY CORRECTION VALIDATION

In order to validate the precision and correctness of the proposed work context, it has been evaluated the error implied accomplishing measurements on an anisotropic radiographic volume, and the consequent importance and need of the application of an interpolation algorithm (Chiarelli et al. 2010b). The testing has been done calculating the errors due to anisotropy considering measures got on an original dataset and on reconstructed ones.

Regarding the reconstructed volumes, both the cases of the application of a 1 Pass Interpolation algorithm and a 2 Pass one are presented. The first one, that is the most common among the few software that tried to face the problem of anisotropy (see for instance Cucchiara et al. 2001, 2004), concerns the use of just one pass of interpolation (the first step described in Section 3.1). The second one, instead, is what it has been developed to maximize the precision and correctness of the whole environment, adding a second step of interpolation and creating de facto a 2 Pass Interpolation algorithm (see Section 3.1). The second algorithm, that is characterized by linear complexity as the first one, has the disadvantage to double the time used by the first one. However, whereas it requires more time, it implies an error significantly inferior to the first algorithm one, as further reported. The evaluation has been done on five scans, two maxillas and three mandibles.

The first step of the adopted procedure has concerned the manufacturing and measurement of titanium reference markers in laboratory, each one of length 10 mm ± 0.03 mm (quoted uncertainty), under controlled conditions (20 °C ± 2 °C and 101325 Pa). This step has been accomplished just to have a precise a relevant comparison element to relate the error to, as for the slice height. Secondly, errors have been calculated, using the datasets parameters, as previously described (see Section 3.2).

TABLE 3.1. ANISOTROPY ERRORS WITHOUT INTERPOLATION

Tested sets				**Without Interpolation**		
#	*Maxilla / Mandible*	*Interslice value (mm)*	*Pixel size (mm)*	*Number of slices*	*Maximum error per slice (mm)*	*Maximum error on a marker length (mm)*
1	Maxilla	0.5	0.2510	140	-0.2490	-4.980
2	Mandible	0.8	0.2340	62	-0.5660	-7.075
3	Mandible	1.0	0.2500	70	-0.7500	-7.500
4	Maxilla	0.5	0.2500	107	-0.2500	-5.000
5	Mandible	0.25	0.2291	242	-0.0209	-0.836

TABLE 3.2. ANISOTROPY ERRORS WITH 1 PASS INTERPOLATION ALGORITHM

Tested sets				**1 Pass Interpolation**		
#	*Maxilla / Mandible*	*Interslice value (mm)*	*Pixel size (mm)*	*Number of slices*	*Maximum error per slice (mm)*	*Maximum error on a marker length (mm)*
1	Maxilla	0.5	0.2510	280	0.0010	0.0398
2	Mandible	0.8	0.2340	186	-0.0327	-1.225
3	Mandible	1.0	0.2500	280	0.0000	0.0000
4	Maxilla	0.5	0.2500	214	0.0000	0.0000
5	Mandible	0.25	0.2291	242	-0.0209	-0.8360

TABLE 3.3. ANISOTROPY ERRORS WITH 2 PASS INTERPOLATION ALGORITHM

Tested sets				**2 Pass Interpolation**		
#	*Maxilla / Mandible*	*Interslice value (mm)*	*Pixel size (mm)*	*Number of slices*	*Maximum error per slice (mm)*	*Maximum error on a marker length (mm)*
1	Maxilla	0.5	0.2510	279	0.00010	0.0040
2	Mandible	0.8	0.2340	212	0.00004	0.0017
3	Mandible	1.0	0.2500	280	0.00000	0.0000
4	Maxilla	0.5	0.2500	214	0.00000	0.0000
5	Mandible	0.25	0.2291	264	-0.00007	-0.0031

The number of slices of the datasets and the implied errors along the axial plane's normal, per slice and on a maker length, are shown in regard of the original dataset, the 1 Pass interpolated one, and the 2 Pass interpolated one in Table 3.1-3.3, for every tested set.

TABLE 3.4. COMPARISON OF ANISOTROPY ERRORS (SET 1)

Markers		**Without Interpolation**		**1 Pass Interpolation**		**2 Pass Interpolation**	
Tooth Number	*Marker slope angle*	*Error on a marker length (mm)*	*Error on a marker length (%)*	*Error on a marker length (mm)*	*Error on a marker length (%)*	*Error on a marker length (mm)*	*Error on a marker length (%)*
11	11.39°	-4.786	-47.9	0.038	0.38	0.004	0.04
12	17.84°	-4.513	-45.1	0.036	0.36	0.004	0.04
13	13.69°	-4.701	-47.0	0.038	0.38	0.004	0.04
14	14.48°	-4.669	-46.7	0.037	0.37	0.004	0.04
15	13.94°	-4.691	-46.9	0.038	0.38	0.004	0.04
16	12.78°	-4.736	-47.4	0.038	0.38	0.004	0.04
21	17.19°	-4.545	-45.5	0.036	0.36	0.004	0.04
22	18.64°	-4.471	-44.7	0.036	0.36	0.004	0.04
23	19.33°	-4.434	-44.3	0.035	0.35	0.004	0.04
24	13.69°	-4.701	-47.0	0.038	0.38	0.004	0.04
25	10.11°	-4.827	-48.3	0.039	0.39	0.004	0.04
26	7.208°	-4.902	-49.0	0.039	0.39	0,004	0.04

TABLE 3.5. COMPARISON OF ANISOTROPY ERRORS (SET 2)

Markers		Without Interpolation		1 Pass Interpolation		2 Pass Interpolation	
Tooth Number	*Marker slope angle*	*Error on a marker length (mm)*	*Error on a marker length (%)*	*Error on a marker length (mm)*	*Error on a marker length (%)*	*Error on a marker length (mm)*	*Error on a marker length (%)*
31	21.69°°	-6.109	-61.1	-1.058	-10.6	0.002	0.02
33	21.60°	-6.116	-61.2	-1.059	-10.6	0.002	0.02
34	23.04°	-5.991	-59.9	-1.037	-10.4	0.001	0.01
35	19.44°	-6.291	-62.9	-1.089	-10.9	0.002	0.02
41	19.40°	-6.294	-62.9	-1.090	-10.9	0.002	0.02
43	22.90°	-6.004	-60.0	-1.040	-10.4	0.001	0.01
44	19.69°	-6.272	-62.7	-1.086	-10.9	0.002	0.02
45	19.40°	-6.294	-62.9	-1.090	-10.9	0.002	0.02
47	21.56°	-6.120	-61.2	-1.060	-10.6	0.002	0.02

TABLE 3.6. COMPARISON OF ANISOTROPY ERRORS (SET 3)

Markers		Without Interpolation		1 Pass Interpolation		2 Pass Interpolation	
Tooth Number	*Marker slope angle*	*Error on a marker length (mm)*	*Error on a marker length (%)*	*Error on a marker length (mm)*	*Error on a marker length (%)*	*Error on a marker length (mm)*	*Error on a marker length (%)*
31	3.046°	-7.429	-74.8	0.000	0.00	0.000	0.00
34	12.53°	-7.147	-71.5	0.000	0.00	0.000	0.00
35	11.10°	-7.222	-72.2	0.000	0.00	0.000	0.00
36	13.56°	-7.088	-70.9	0.000	0.00	0.000	0.00
41	6.013°	-7.418	-74.2	0.000	0.00	0.000	0.00
44	9.462°	-7.297	-73.0	0.000	0.00	0.000	0.00
45	7.548°	-7.371	-73.7	0.000	0.00	0.000	0.00
46	9.757°	-7.285	-72.9	0.000	0.00	0.000	0.00

TABLE 3.7. COMPARISON OF ANISOTROPY ERRORS (SET 4)

Markers		**Without Interpolation**		**1 Pass Interpolation**		**2 Pass Interpolation**	
Tooth Number	*Marker slope angle*	*Error on a marker length (mm)*	*Error on a marker length (%)*	*Error on a marker length (mm)*	*Error on a marker length (%)*	*Error on a marker length (mm)*	*Error on a marker length (%)*
15	3.270°	-4.984	-49.8	0.000	0.00	0.000	0.00
16	5.856°	-4.948	-49.5	0.000	0.00	0.000	0.00
17	5.279°	-4.958	-49.6	0.000	0.00	0.000	0.00

TABLE 3.8. COMPARISON OF ANISOTROPY ERRORS (SET 5)

Markers		**Without Interpolation**		**1 Pass Interpolation**		**2 Pass Interpolation**	
Tooth Number	*Marker slope angle*	*Error on a marker length (mm)*	*Error on a marker length (%)*	*Error on a marker length (mm)*	*Error on a marker length (%)*	*Error on a marker length (mm)*	*Error on a marker length (%)*
32	8.930°	-0.816	-8.16	-0.816	-8.16	-0.003	-0.03
34	3.814°	-0.832	-8.32	-0.832	-8.32	-0.003	-0.03
35	6.785°	-0.824	-8.24	-0.824	-8.24	-0.003	-0.03
42	10.52°	-0.808	-8.08	-0.808	-8.08	-0.003	-0.03
43	10.62°	-0.808	-8.08	-0.808	-8.08	-0.003	-0.03
44	6.633°	-0.825	-8.25	-0.825	-8.25	-0.003	-0.03
45	4.086°	-0.832	-8.32	-0.832	-8.32	-0.003	-0.03
46	0.000°	-0.836	-8.36	-0.836	-8.36	-0.003	-0.03

In Table 3.4-3.8, instead, the anisotropy implied errors for every marker installed are reported, calculating the value of the error in relation to the slope angle of the teeth/markers axes. Again, the values achieved without interpolation and with interpolation procedures are compared, showing the considerable improvement obtained through the proposed method.

Regarding the tested datasets, the mean of absolute values of errors on a marker length (10 mm) achieved with the 2 Pass Interpolation algorithm is about 0.03% (0,003 mm) where the 1 Pass one is about 5.74% (0.574 mm) and 40.7% (4.070 mm) without interpolation, excluding the cases of interslice value multiple of pixel-size one. Concerning the overall mean, instead, the value of the error implied by the 2 Pass Interpolation algorithm decreases to 0.02% (0.002 mm) where the 1 Pass one is about 4.16% (0.416 mm), growing to 47.8% (4.781 mm) without interpolation. Results achieved demonstrate the precision obtained through the use of the additional interpolation step presented, solving the anisotropy problem and outperforming the more simple 1 Pass Interpolation algorithm.

CHAPTER 4: CORRECT CROSS PLANES

As discussed in Section 1.3.3, through common DentaScan multi-view approaches (SurgiCase® and SimPlant®, Materialise; Cucchiara at al. 2001; DentaScan, GE Medical System), achieved cross-sectional planes are orthogonal to coronal and axial ones (see Fig. 4.1), but almost always not parallel to the tooth axis of interest (the one or one of them the implantologist has to work on). Consequently, measures obtained in cross-sectional images can be affected by a systematic effect, which depends on the angle ϕ between the axis of the tooth and the plane of the cross-sectional image (see Section 1.3.3). On the contrary, in Fig. 4.3 is shown how a correct cross-sectional plane should cut the radiographic volume, that is parallelly to the axis of interest, allowing to achieve a correct view of the neighbouring area (see Fig. 4.4). Thus, in order to be able to compute correct measurements, the best cut plane to work upon can not be orthogonal to the axial and panoramic planes, unless, before exploting the dataset through a planning software, the transaxial plane of the scan is set orthogonally to the axis of interest on purpose.

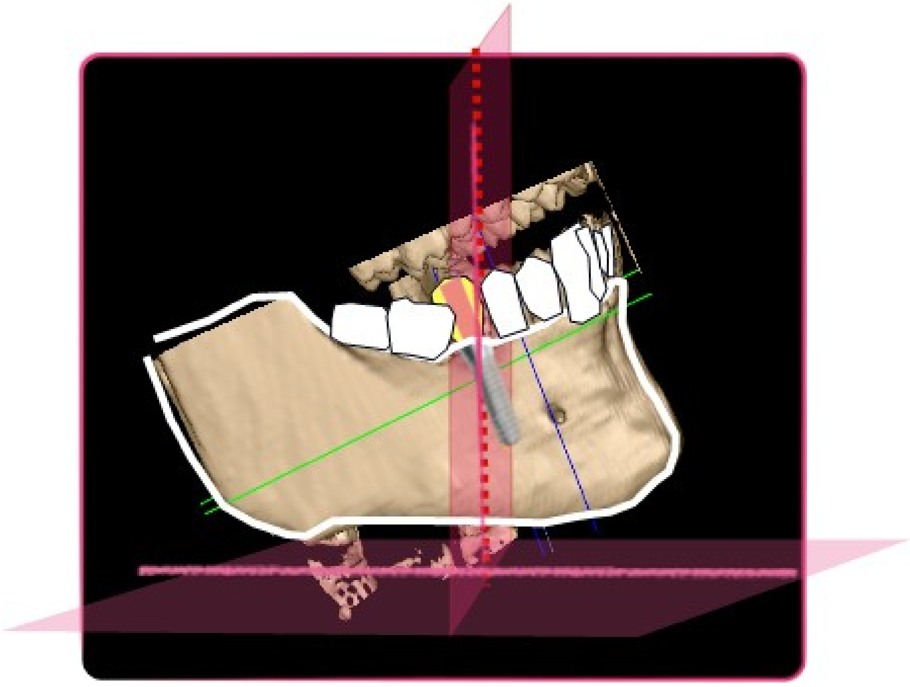

Fig. 4.1. *Cross-sectional plane (vertical) orthogonal to the axial one (horizontal)*

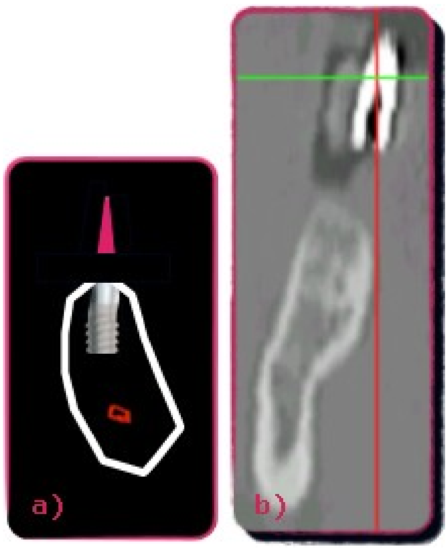

Fig. 4.2. *a) oblique cut of the axis of interest and b) a common cross cut plane*

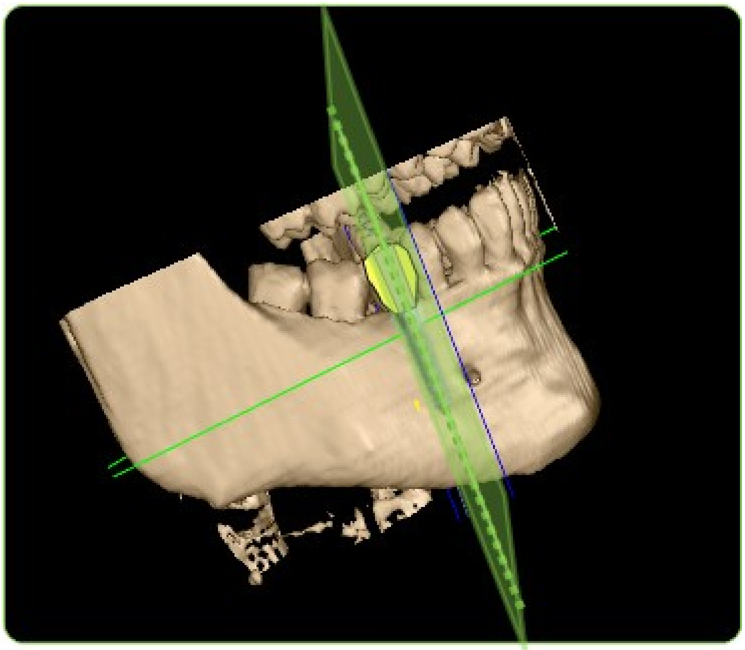

Fig. 4.3. *Cross-sectional plane parallel to the axis of interest*

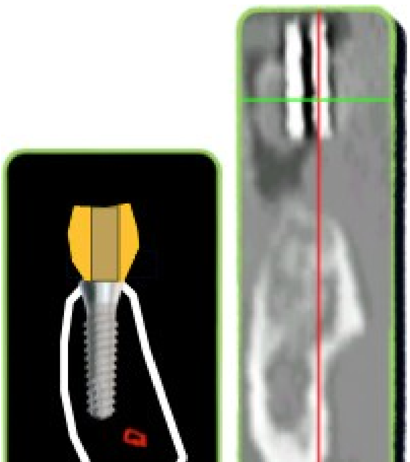

Fig. 4.4. *a) axis of interest parallel cut and b) a correct cross cut plane*

However, the problem is not limited to a single axis. Actually, even taking in consideration to obtain a CT scan with the transaxial plane orthogonal to a tooth axis of interest, the resulting cross-sectional planes will be suitable only for that axis. Thus, knowing that the teeth axes are not parallel each other, due to their directional convergence towards a dental-arch related specific point (see Fig. 4.5), if a patient requires more implants, different cutting planes should be reconstructed.

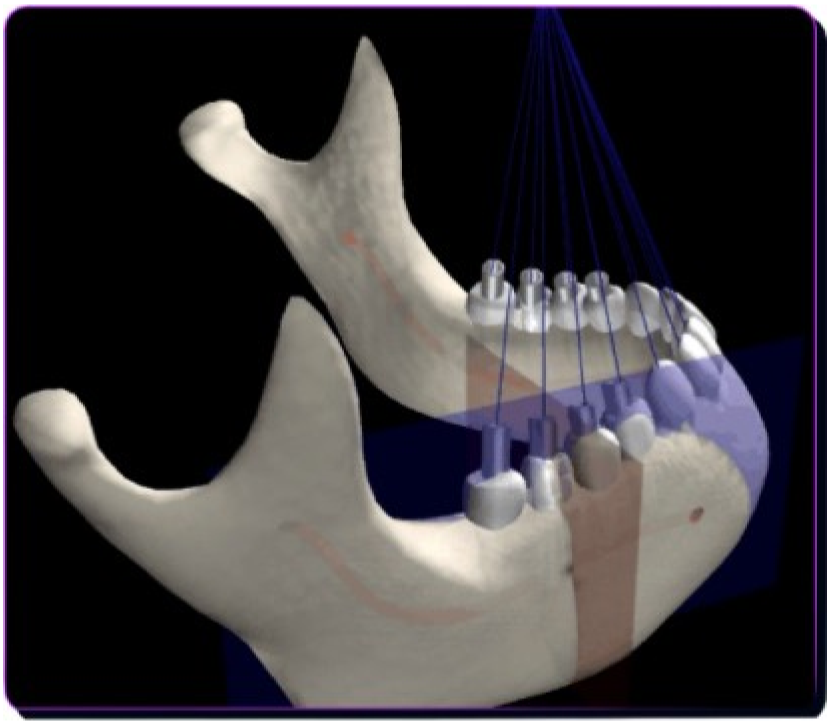

Fig. 4.5. *Teeth axes convergence towards a specific point*

4.1 RUNTIME CUSTOM RECONSTRUCTION

In order to solve the problem described, Cucchiara et. al (2001; 2004) proposed to re-orient the original CT dataset according to a computed relevant direction, usually equal to the axis of a radio-opaque marker (e.g., titanium hollow cylinders) inserted in a radiological mask worn by the patient during the CT scan. The importance of that pre-planned axis is due to the fact that the radio-opaque marker is installed to represent the best orientation for the prosthesis, and therefore, when it is clinically possible, it is the preferred drilling direction. As a consequence, in order to get cross-sectional planes parallel to the chosen planned implant, it has been decided to follow the idea of Cucchiara et al., but with a procedure diversion, taking advantage of the software 3D work context. In fact, in order to allow the freedom to manage any cut plane needed during the same planning session, it has been discarded the marker-strictly-related dataset re-orienting, in favor of a run-time completely custom cross-sectional reconstruction feature. This functionality operates on the axial view and allows to choose at run-time, thus dynamically, an arbitrary cutting plane in the radiographic volume. In Fig. 4.6 is shown a comparison between a radiographic section seen through a common cross-sectional view and the same section corrected with the developed tool.

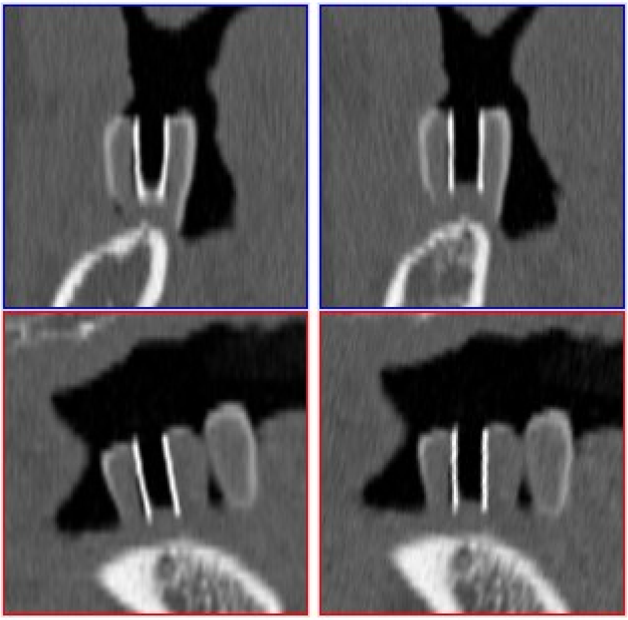

Fig. 4.6. *Common cross cut (left) and its corrected version (right)*

The procedure consists of identifying a line, for example the wanted tooth axis, selecting two points in the axial volume by two simple mouse clicks, and then choosing the desired plane from a sheaf of planes through mouse selection as well (see Fig. 4.7).

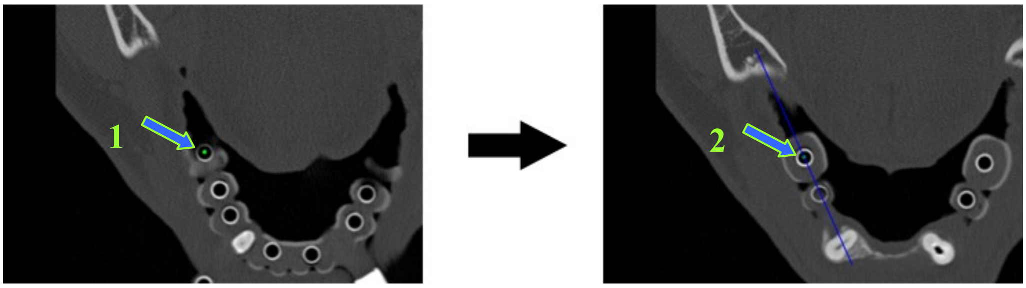

Fig. 4.7. *Axis of interest identification and cut plane selection (blu line)*

Automatically and in real-time the software provides, through library demanded interpolation, the desired cross-sectional plane and its orthogonal one (in order to have a wider prospect of the area of interest) in two different views. The external library used to interpolate the radiographic volume is the same to which is demanded its handling (see Chapter 2).

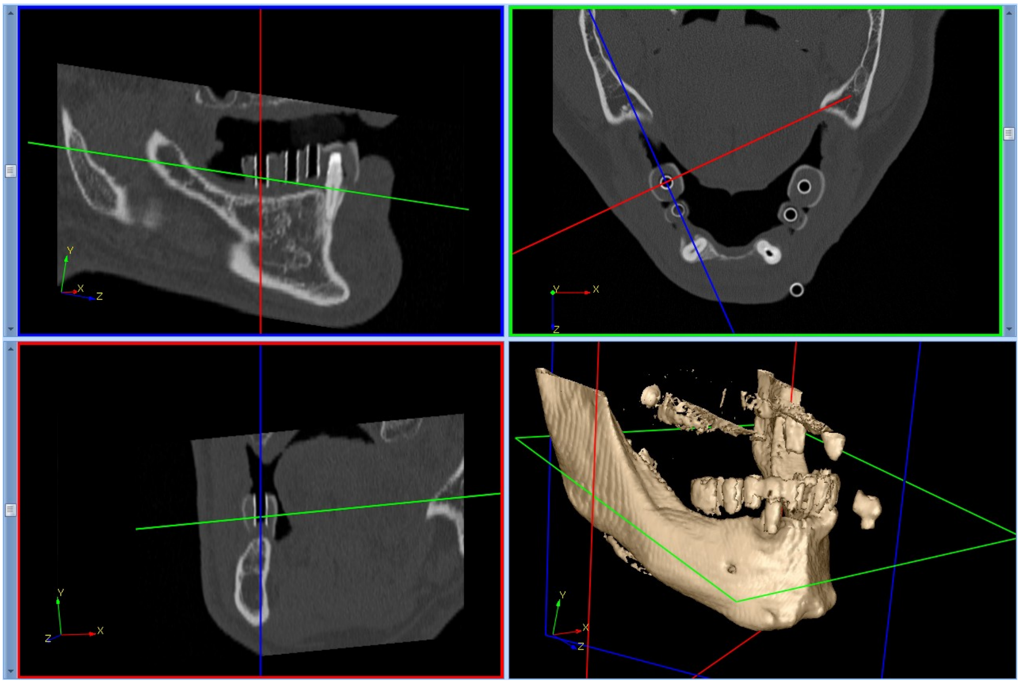

Fig. 4.8. *Interpolation reconstructed custom cross-sectional*

4.2 RUNTIME AUTOMATIC RECONSTRUCTION

In order to speed up and simplify the planning operations, and contemporarily to improve the precision of the marker axes identification, it has been added the possibility to reconstruct the best cross-sectional planes automatically. Exploiting this feature, the user does not need to trace any axes to identify the pre-planning marker ones, instead, the software will automatically recognize and provide them, together with the related oblique planes. Apart from simplifying the work of the user, this feature has the advantage to avoid any error due to the manual identification process. The procedure consists of informing the software about the markers diameter and length (see Fig. 4.9), that can be measured with the provided measurement tools (see Chapter 2), and letting it searches the markers axes.

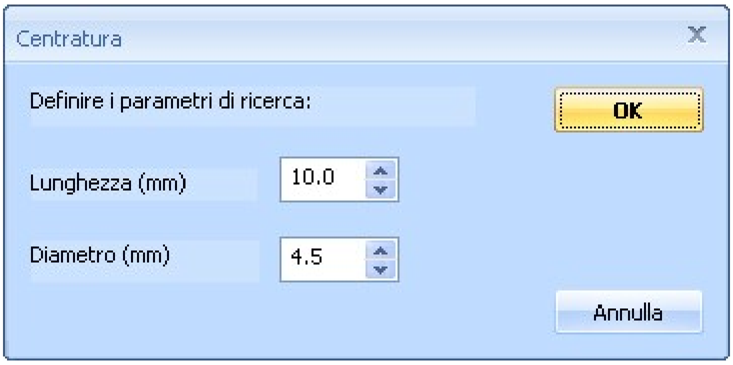

Fig. 4.9. *Markers parameters definition window for automatic identification*

The markers are then automatically found scanning the axial slices through the use of the Hough Transform technique for the objects recognition in images. The whole operation is at run-time, so it is possible to automatically identify markers of different widths repeating the procedure, after having changed the diameter value. When it has finished, the system provides the list of the found axes: at this point the implantologist has just to choose the preferred one and the desired plane from the related sheaf of planes (see Fig. 4.10). Consequently, as for the manual best cross-sectional reconstruction, the software immediately provides the chosen cut plane and its orthogonal one.

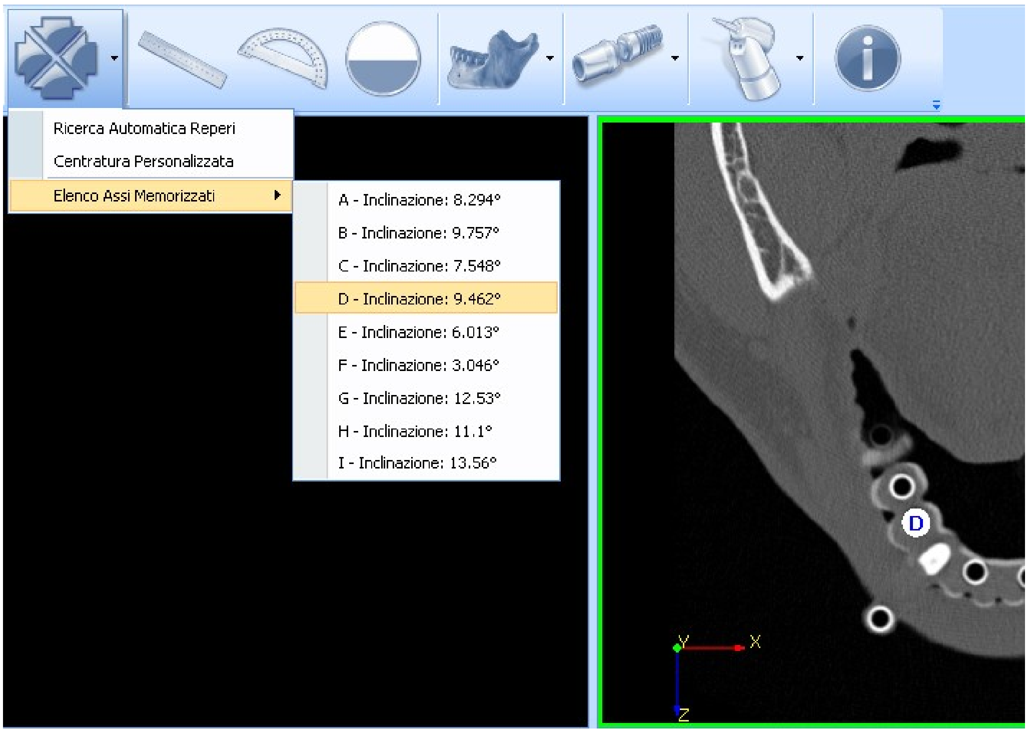

Fig. 4.10. *Selecting the desired one from the automatically identified axes list*

4.2.1 AUTOMATIC IDENTIFICATION INTEGRATION

The described automatic identification feature has been achieved integrating the algorithm explained by Cucchiara et al. (2004) in the software. They propose a pattern recognition solution that avoids to face the marker identification through its 3D solid rotation analysis, and consequently its computationally high cost too. On the contrary, they exploit the hollow cylindrical marker subdivision among the dataset slices, searching for groups of circular patterns sharing the same geometrical properties, like centers belonging to the same axis and common or similar shape and area. The described process is defined in two steps:

I. circular objects identification;
II. model based clustering.

In the first step, every circular object has to be detected, and then, in the second one, they will be grouped following the clustering model constraints. Concerning the circular objects recognition step, it is possible to divide it in two major phases: the edges extraction and the circulars shape identification. To accomplish the first duty it has been used the Canny Edge detector (Canny 1996), an algorithm able to find closed edges, above all the ones characterized by one pixel of thickness. The second task, instead, is delegated to the Hough Transform for circle in the Edge Feature space, that is part of a class of algorithms for parametric shape detection widely used in pattern recognition (Illingworth & Kittler 1988). Finally, the detected circular sections are grouped by the model based clustering in relation to some constraints like distances between each other, slope angle of related axes, or maximum extension permitted by the model dimensions, finishing with the confirmation of the most probable markers and the calculation of their axes. In Fig. 4.11 is shown the described procedure.

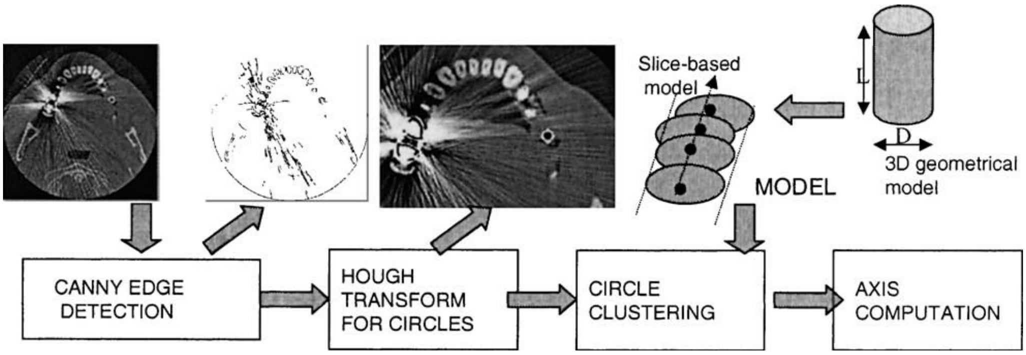

Fig. 4.11. *Implant before (left) and after (right) having centered the views on it*

4.3 RUNTIME IMPLANTS CENTERING

With the aim of completing the slice reconstruction tool, it has been extended the functionality regarding the cut planes of the planned implants. This feature allows the user to choose at run-time to reconstruct the cross-sectional planes parallelly to the height axis of the desired planned implant, simply right-clicking on the implant and selecting the centering operation on the related context menu. After having chosen the preferred plane from a sheaf of planes, the software will automatically provide the requested cut planes trough the same interpolation procedure used for the custom reconstruction (see Fig. 4.12). This functionality allows to know, at any particular time, the surrounding area of the implant, providing the possibility to achieve fundamental and correct distances between the borders of the implant and the rest of the environment.

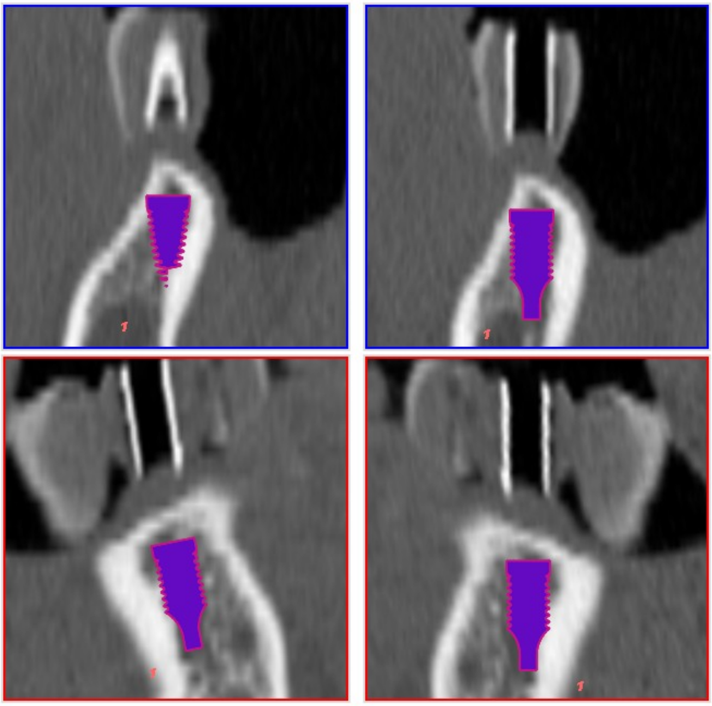

Fig. 4.12. *Implant before (left) and after (right) having centered the views on it*

4.4 CROSS RECONSTRUCTION EVALUATION

In order to evaluate the correctness of CT images elaborated with the proposed approach, measures achieved by the developed software have been compared, using the custom reconstruction of the best cross-sectional plane, with the ones obtained by other DentaScan based software tools for oral implantology (Chiarelli et al. 2010a).

The first step of the measurement procedure concerns the manufacturing and measurement of the titanium reference markers in laboratory, under controlled conditions (20 °C ± 2 °C and 101325 Pa). Secondly, the markers are installed in a support (e.g. a human mandible) and scanned by a CT scanner set with defined parameters. Then, after having imported and loaded the achieved data in the presented software, the last step consists of measuring the radiographic representation of the markers in the reconstructed best cross-sectional view (see Section 4.1), through the software measuring tool (see Chapter 2).

It has been tested the approach on a data set of CT images obtained by scanning a dried human partially edentulous mandible where there were posed radio-opaque cylinders, each one of length 10 mm ± 0.03 mm (quoted uncertainty) with a level of confidence of 99.9% (measurements accomplished by micrometer). The scanning was achieved by a CT scanner Toshiba Xpress with the following parameters: 135 kVp; 150 mA; scanning time of 1 s for each axial acquisition; 5 min as time of secondary reconstruction; image reconstruction matrix of 512x512 pixel; 1 mm of pixel thickness; 1.2 mm/s as table speed; back-reconstruction of 0.8 mm. The lower border of the mandible was chosen as reference plane. Five different sets of scans were taken for the jaw: the first with the transaxial scans parallel to the lower border of the mandible (as it is usual in practice), and the others by varying the direction of the scans of 10°, 15°, 20°, and 30°.

TABLE 4.1. COMPARISON OF MARKERS POSITIONS

Interval $x_1 \leq x < x_2$		**Length**
x / mm	***x / mm***	***x / mm***
9.900	9.925	9.923
9.925	9.950	-
9.950	9.975	9.969; 9.969; 9.970; 9.971
9.975	10.000	-
10.000	10.025	10.016; 10.016; 10.016; 10.016; 10.016; 10.016; 10.016; 10.017; 10.019
10.025	10.050	10.042
10.050	10.075	10.062; 10.063; 10.063; 10.065; 10.065
10.075	10.100	-

With the purpose of reporting the achieved results with completeness, it has been evaluated their value of uncertainty in accordance with the ISO Guide to the Expression of Uncertainty in Measurement (GUM, © Joint Committee for Guides in Metrology), following the related guidelines. First of all, it has been defined the output estimate as the sum of two input components, the uncorrected result of the measurement and the correction for the interpolation systematic effect, although it has been ignored the second one to the uncertainty calculation procedure because it does not contribute a significant component of uncertainty to the result of the measurement. Then, chosen a marker (i.e. n. 47), we have estimated the uncorrected result of the measurement as the mean of 20 repeated observations (see Table 4.1). With the resulting average (10.016 mm) it has been evaluated the Type A standard uncertainty, according to the GUM rules and formulas. The calculated experimental variance and experimental standard deviation are respectively 0.0015 mm and 0.0387 mm, while the experimental variance of the mean (Type A variance) and experimental standard deviation of the mean (Type A standard deviation), which is the standard uncertainty of the calculated mean, are respectively 0.000075 mm and 0.0087 mm. Finally, it has been determined the combined standard uncertainty of the measurement result, that is equal to the Type A standard uncertainty, so 0.0087 mm, in consideration of the previous observation regarding the exclusion of the interpolation systematic effect component. At this point, it has been taken in consideration the cylinders manufacturer specifications to calculate the uncertainty of the measurand stated length, that is the comparison value. Having a coverage factor of 3, the Type B standard uncertainty of the provided length results to be 0.01 mm: adding this component to the uncertainty of the measurement result obtained, the comparison value becomes a true value of the measurand equal to 10 mm, giving the possibility to compare the achieved result directly to 10 mm. Notice that it has been ignored any sampling systematic effects of the CT scanner, either they are randomized on voxels or uniformly applied, due to the subjectivity of measurements on radiographies via software (random wrong pixels are instinctively ignored) and because lengths and distances do not change if the whole volume is uniformly moved. Said that, it has been taken the assumption that the evaluated uncertainty may be assigned to every accomplished measurement, due to the significant similarity of both conditions of measurement and measurands. Consequently, the reported corrected measurement results (Table 2-4,8-12) have to be considered having an uncertainty of 0.019 mm and degrees of freedom equal to 19. Moreover, to provide a complete definition of the conditions of measurement, it is the case to specify that the measurand is a radiographic digital representation, achieved as CT or CBCT and visualized and measured via software, of a titanium maker, and that measurement results, errors and systematic effect values are determined to micrometre accuracy.

In Table 4.2-4.4, it has been reported the corrected results for some computed measures, referring respectively to the reference markers installed by the second lower right molar (tooth n. 47), by the lower right incisor (tooth n. 41), and by the second lower left premolar (tooth n. 35). Notice that, by reconstructing the best cross-sectional plane through the proposed tool feature, the absolute value of error of measurement has been significantly reduced, from even 40% to 0.21%.

TABLE 4.2. COMPARISON OF MEASUREMENT ERRORS FOR MAKER N.47

Marker n. 47	**DentaScan cross-sectional**			**Custom reconstructed best cross-sectional**		
Angle between acquisition plane and lower jaw border	***Angle between visualized object and real object axes***	***Measured reference marker length (mm)***	***Error of measurement (%)***	***Angle between visualized object and real object axes***	***Measured reference marker length (mm)***	***Error of measurement (%)***
0°	20.2°	9.04	-9.6	0°	10.014	0.14
10°	42.6°	6.81	-31.9	0°	10.028	0.28
15°	33.9°	7.50	-25.0	0°	10.023	0.23
20°	44.9°	6.92	-30.8	0°	10.041	0.41
30°	44.2°	5.91	-40.9	0°	10.021	0.21

TABLE 4.3. COMPARISON OF MEASUREMENT ERRORS FOR MAKER N.41

Marker n. 41	**DentaScan cross-sectional**		**Arbitrary reconstructed best cross-sectional**	
Angle between acquisition plane and lower jaw border	***Measured reference marker length (mm)***	***Error of measurement (%)***	***Measured reference marker length (mm)***	***Error of measurement (%)***
0°	10.74	7.4	10.025	0.25
10°	N/A	N/A	N/A	N/A
15°	10.92	9.2	10.060	0.60
20°	9.95	-0.5	10.063	0.63
30°	10.64	6.4	10.026	0.26

TABLE 4.4. COMPARISON OF MEASUREMENT ERRORS FOR MAKER N.35

Marker n. 35	**DentaScan cross-sectional**		**Arbitrary reconstructed best cross-sectional**	
Angle between acquisition plane and lower jaw border	***Measured reference marker length (mm)***	***Error of measurement (%)***	***Measured reference marker length (mm)***	***Error of measurement (%)***
0°	10.70	7.0	10.028	0.28
10°	6.55	-34.5	10.065	0.65
15°	8.42	-15.8	10.058	0.58
20°	6.08	-39.2	10.053	0.53
30°	6.55	-34.5	10.023	0.23

TABLE 4.5. COMPARISON OF INTERPOLATION SYSTEMATIC EFFECTS

Tested sets		**Interpolation error**	
Angle between acquisition plane and lower jaw border	***Number of slices per set***	***Interpolation error per slice (mm)***	***Interpolation error on a marker length (mm)***
0°	62	0.00004	0.0017
10°	74	0.000008	0.00034
15°	76	0.00015	0.0066
20°	80	0.0004	0.018
30°	90	0.0002	0.01

For every set, it was also calculated the error implied by the operation of interpolation during the isotropic reconstruction of the three-dimensional radiographic volume, so prior to the human measurement random effect (i.e., the choice of a pixel instead of another when defining the extremities of the segment to be measured). It results that on an original dataset having an average of about 76 slices and a pixel size of 0.234 mm, the value of the systematic effect per slice due to interpolation is about 0.00016 mm, while the value of the same systematic effect calculated on the length of a tested marker (10 mm) is about 0.007 mm. In Table 4.5 we report the interpolation errors on the tested sets.

In Table 4.6, instead, are shown found performances and requirements about data processing and memory usage regarding the five radiographic set analyzed. Calculating averages it results that for a set of about 76 slices, the application uses about 18 seconds to create the isotropic volume and about 2.8 seconds to extract the polygonal model, requiring about 285 MB of RAM and 36 MB of VideoRAM.

TABLE 4.6. COMPARISON OF PERFORMANCES AND REQUIREMENTS

Tested sets		**Application performances: reconstruction times**		**Application requirements: memory usage**	
Angle between acquisition plane and lower jaw border	***Number of slices per set***	***Volume reconstruction time (s)***	***3D Model reconstruction time (s)***	***RAM usage (MB)***	***Video RAM usage (MB)***
0°	62	15	2.8	256.400	35.77
10°	74	17	2.5	278.496	35.77
15°	76	18	3	286.396	35.89
20°	80	18.5	2.5	284.572	36.01
30°	90	22	3	320.328	37.10

4.5 AUTOMATIC IDENTIFICATION VALIDATION

It has been also tested the reliability of the markers automatic identification feature. The evaluation has been done testing the functionality concerning the two main aspects: markers identification and correctness of the found axes. Firstly, it has been used the automatic identification feature on several cases of study, under different conditions, to analyze the efficiency of the functionality; then, the measurements obtained through the use of both the manual and the automatic tools have been compared to validate the correct axes identification. Regarding the efficiency, it has been used the automatic identification feature on fifteen scans of human mandibles and maxillas, having assorted slices amounts and number of markers, and different interslice and pixel-size values, coming from various manufacturers. Some study cases, moreover, were affected by extreme noises, like the partial blending of the markers with the surroundings, due to reflections, or their partial hiding, due to shadow effects.

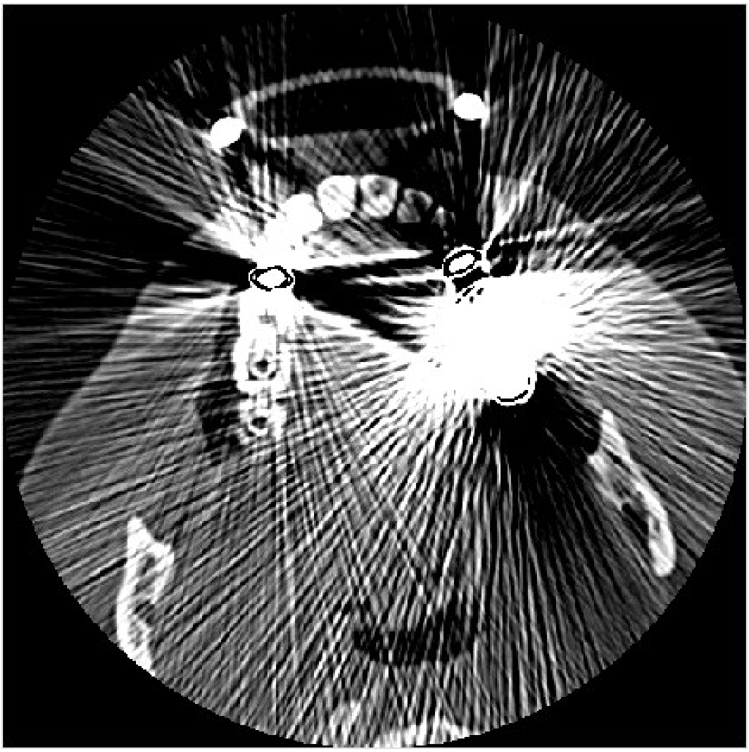

Fig. 4.13. *Example of extreme scattering effect*

Tests pointed out that these extreme noises may affect negatively the identification algorithm, decreasing significantly the percentage of success. Excluding the extreme noise affected cases, the tested efficiency of the functionality for the automatic identification of the markers is 93%, while the overall efficiency average of the fifteen cases is 74%.

In Table 4.7 are reported the discussed results, while in Table 4.8 is shown the comparison of the measurements got through the two markers identification functionalities, taking as example the set no.2 of the tested datasets (see Table 4.7).

TABLE 4.7. EFFICIENCY EVALUATION FOR THE AUTOMATIC IDENTIFICATION ALGORITHM

Tested sets								Feature Performances		
#	*Maxilla / Mandible*	*Slices per set*	*Interslice value (mm)*	*Pixel size (mm)*	*CT Scanner*	*High noise*	*Number of markers*	*Num of found markers*	*Search time (s)*	*Efficiency (%)*
1	Maxilla	140	0,5	0,251	Toshiba	N	12	9	17	75
2	Mandible	62	0,8	0,234	Toshiba	N	9	8	5	89
3	Mandible	59	1,0	0,250	Philips	Y	9	4	8	44
4	Maxilla	48	1,0	0,250	Philips	Y	9	2	7	22
5	Mandible	70	1,0	0,250	Philips	N	8	8	8	100
6	Mandible	51	1,0	0,250	Philips	N	5	4	7	80
7	Mandible	75	0,8	0,234	Toshiba	N	4	4	8	100
8	Maxilla	107	0,5	0,250	Toshiba	Y	3	0	13	0
9	Maxilla	45	1,0	0,250	Philips	Y	2	2	6	100
10	Mandible	50	1,0	0,250	GE M.S.	Y	2	1	6	50
11	Mandible	56	1,0	0,250	Philips	Y	2	1	7	50
12	Maxilla	47	0,8	0,234	Toshiba	N	1	1	6	100
13	Maxilla	112	0,5	0,250	Philips	N	1	1	14	100
14	Mandible	62	0,8	0,234	Toshiba	N	1	1	7	100
15	Maxilla	32	1,0	0,250	Toshiba	Y	1	1	4	100

The validation of the correctness for the identified axes has been accomplished measuring the markers on the cross-sectionals reconstructed through both the custom and automatic functionalities, and comparing the achieved measures.

TABLE 4.8. COMPARISON OF MARKERS POSITIONS

Markers	Custom reconstructed cross-sectionals		Automatic reconstructed cross-sectionals	
Tooth Number	*Measured reference marker length (mm)*	*Measure error (%)*	*Measured reference marker length (mm)*	*Measure error (%)*
31	9,950	-0,50	9,951	-0,49
33	9.998	0,02	9,950	-0,50
34	9,951	-0,49	9,952	-0,48
35	9,950	-0,50	N/A	N/A
41	9,927	-0,73	10,067	0,67
43	10,045	0,45	9,975	-0,25
44	9,952	-0,48	10,046	0,46
45	10,068	0,68	9,928	-0,72
47	10,041	0,41	9,974	-0,26

As shown (see Table 4.8), the measures obtained through the automatic reconstruction are comparable with the custom reconstruction ones. In particular, regarding the second tested dataset, the average error on the measurement of a marker of 10 mm is about 0.48%, equal to 0.048 mm, differing from the manual reconstruction of just 0.1%.

4.6 CBCT IMAGES COMPATIBILITY

Finally, in order to support the validation of the proposed work, we have also evaluated measurements achieved through the software tool on Cone Beam Computed Tomography images. It has been tested the proposed approach on four datasets, respectively two maxillas and two mandibles, measuring the radio-opaque cylinders installed in. The scans, obtained by a CBCT scanner CEFLA GROUP – MYRAY, are characterized by an Interslice value of 0.25 mm and a Pixel size of 0.2291 mm, and have been achieved with the following scanning parameters: 90 kV; 6.5 mA; image reconstruction matrix of 512x512 pixel; 0.25 mm of pixel thickness. The maxillas datasets are composed of 170 and 175 slices, whereas the mandibles ones consist of 242 and 257 slices. The measures have been achieved on cross-sectionals reconstructed through the arbitrary slice reconstruction functionality: the CBCT images have resulted too blurred for the markers automatic identification feature. Concerning the tested datasets (see Table 4.9-4.12), it results that the mean of absolute values of errors of measurement on a length of 10 mm is about 0.33%, equal to 0.033 mm, validating the usability of CBCT images for our software system and global approach consequently.

TABLE 4.9. COMPARISON OF MEASURES FOR CBCT MAXILLA 1

Markers		**Arbitrary reconstructed cross-sectionals**	
Tooth Number	***Real reference marker length (mm)***	***Measured reference marker length (mm)***	***Error of measurement (%)***
14	10	10.031	0.31
15	10	10.031	0.31
16	10	10.030	0.30
17	10	9.938	-0.62
24	10	10.032	0.32
25	10	10.033	0.33
26	10	10.034	0.34
27	10	10.033	0.33

TABLE 4.10. COMPARISON OF MEASURES FOR CBCT MAXILLA 2

Markers		**Arbitrary reconstructed cross-sectionals**	
Tooth Number	***Real reference marker length (mm)***	***Measured reference marker length (mm)***	***Error of measurement (%)***
14	10	9.992	-0.08
15	10	9.987	-0.13
23	10	10.034	0.34
24	10	9.987	-0.13
25	10	9.987	-0.13
26	10	9.987	-0.13

TABLE 4.11. COMPARISON OF MEASURES FOR CBCT MANDIBLE 1

Markers		**Arbitrary reconstructed cross-sectionals**	
Tooth Number	***Real reference marker length (mm)***	***Measured reference marker length (mm)***	***Error of measurement (%)***
32	10	10.084	0.84
34	10	10.039	0.39
35	10	10.084	0.84
42	10	10.038	0.38
43	10	9.992	-0.08
44	10	10.038	0.38
45	10	9.992	-0.08
46	10	10.061	0.61

TABLE 4.12. COMPARISON OF MEASURES FOR CBCT MAMDIBLE 2

Markers		**Arbitrary reconstructed cross-sectionals**	
Tooth Number	***Real reference marker length (mm)***	***Measured reference marker length (mm)***	***Error of measurement (%)***
31	10	10.047	0.47
32	10	10.028	0.28
41	10	10.038	0.38
42	10	9.984	-0.16

CHAPTER 5: ANATOMY RECOGNITION

The *inferior alveolar nerve*, or mandibular nerve, is the largest of the three branches of the *trigeminal nerve*, and it passes through the mandibular canal, a bone longitudinal cavity within the mandible. This canal starts with the *mandibular foramen*, an opening in the inner side of the back of the mandible, and emerges in the *mental foramen*, an opening in the outer side of the anterior part of mandible. The inferior alveolar nerve, including its branches, provides sensory innervation to the lower teeth, the lower lip, and some skin of the lower face. As previously mentioned (see Section 1.3.4), injuring something in this area is particularly dangerous: apart from the risk to break some of the vessels that pass inside the same canal, like the *inferior alveolar artery*, that would lead to a possibly serious loss of blood, hurting the mandibular nerve implies the paralysis of the whole mandible. Thus, considering the importance of this anatomy in oral implantology, it appears obvious the need of an identification system to help the user to bear in mind it during the planning, better if the system is an automatic recognition feature.

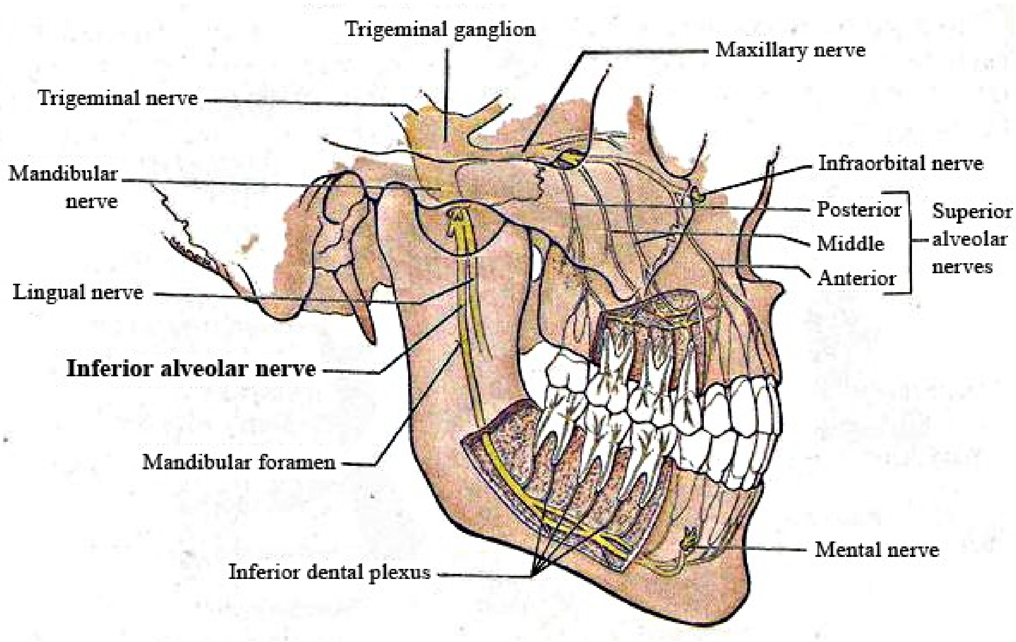

Fig. 5.1. *Inferior alveolar nerve*

5.1 MANDIBULAR NERVE CANAL DRAWING

The first step to the path towards the automatic recognition feature, it has been to implement the option to draw it manually. This choice has been determined by two factors:

- automatic identification features and pattern recognition algorithms base their efficiency on the quality of the image, apart from the reliability of the algorithm itself obviously; knowing this and the fact that possibly computed tomography images can be disturbed by patient movement noise and scattering, it is wise to provide the manual alternative;

- the class structure that would have been represented the canal object and the feature module that would have handled the drawing of the canal would have been needed in the automatic functionality as well, and could be exploited without additional work as a consequence.

5.1.1 CATMULL-ROM SPLINES

In order to implement the drawing, it has been initially necessary to decide the mathematical function to be used to define the curve shape of the canal. As it is popular in computer graphics, it has been opted for a spline, a special function defined piecewise by polynomials, due to its typical advantages, like the simplicity of construction and the design interactivity. However, differently from the common spline choice, it has been decided for a cubic Hermite spline rather than a B-spline. The chosen spline, also called cspline, that is usually used in aeronautic design, is a third-degree spline with each polynomial of the spline in Hermite form, that is having two control points and two tangents for each polynomial. In particular, among the cspline types, it has been chosen the Catmull-Rom one. Quoting Twigg (2003), Catmull-Rom splines are a family of cubic interpolating splines formulated such that the tangent at each point p_i is calculated using the previous and next point on the spline, $\tau(p_{i+1} - p_{i-1})$. Their geometry matrix is given by:

$$p(s) = \begin{bmatrix} 1 & u & u^2 & u^3 \end{bmatrix} \begin{bmatrix} 0 & 1 & 0 & 0 \\ -\tau & 0 & \tau & 0 \\ 2\tau & \tau-3 & 3-2\tau & -\tau \\ -\tau & 2-\tau & \tau-2 & \tau \end{bmatrix} \begin{bmatrix} p_{i-2} \\ p_{i-1} \\ p_i \\ p_{i+1} \end{bmatrix}$$

Whereas $p(s)$ is a single Catmull-Rom segment, p_{i-2}, p_{i-1}, p_i, and p_{i+1} are the 4 control points that define $p(s)$, and u is the variable of its polynomial form:

$$p(s) = c_0 + c_1 u + c_2 u^2 + c_3 u^3 = \sum_{k=0}^{3} c_k u^k$$
$$c_0 = p_{i-1}$$
$$c_1 = \tau(p_i - p_{i-2})$$
$$c_2 = 3(p_i - p_{i-1}) - \tau(p_{i+1} - p_{i-1}) - 2\tau(p_i - p_{i-2})$$
$$c_3 = -2(p_i - p_{i-1}) + \tau(p_{i+1} - p_{i-1}) + \tau(p_i - p_{i-2})$$

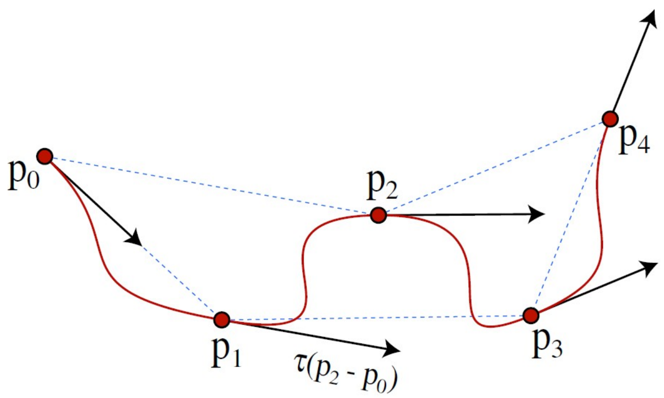

Fig. 5.2. *A Catmull-Rom spline*

The parameter $\tau \in [0,1]$ is known as *tension* and it affects how sharply the curve bends at the (interpolated) control points (see Fig. 5.3). As it is usually set to, it has been opted for 0.5 also in the implemented case, in relation to the curve sharpness needed.

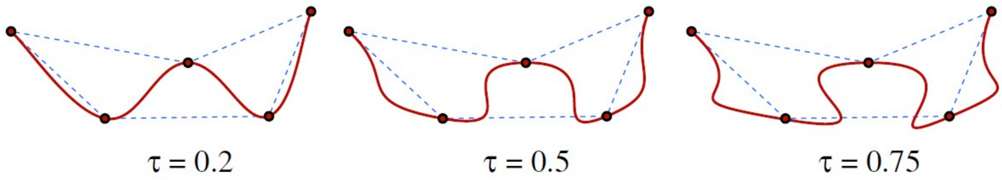

Fig. 5.3. *The effect of the tension τ*

As common splines, Catmull-Rom ones have C^1 continuity, local control, and interpolation, although, differently, they do not lie within the convex hull of their control points. However, they have an important characteristic: Catmull-Rom splines always pass through their control points. This feature is, actually, the main the reason of this choice, instead of B-splines, due to the need of having the drawn curve passing through the user interactively identified control points.

Thus, spline classes have been developed and integrated in the 3D engine, and the Catmull-Rom version has been used in the mandibular canal drawing feature.

5.1.2 CURVE DESIGN

Using the Catmull-Rom spline and exploiting its characteristic of passing through its control points, the design operation has been simplified the most possible. Actually, the proposed procedure consists of the following simple steps only:

1. scrolling the oblique view to reach the mandibular foramen (the software automatically chooses the best oblique cut plane when the feature is selected), and mouse clicking over it;
2. moving forward (scrolling the oblique view) following the mandibular canal, and clicking again, from time to time, identifying its position along its path;
3. clicking at last on the mental foramen when reached it.

The software interprets every click as the identification of a control point, and, consequently, it is able to achieve the needed curve function, passing through the user defined points and corresponding to the mandibular canal path.

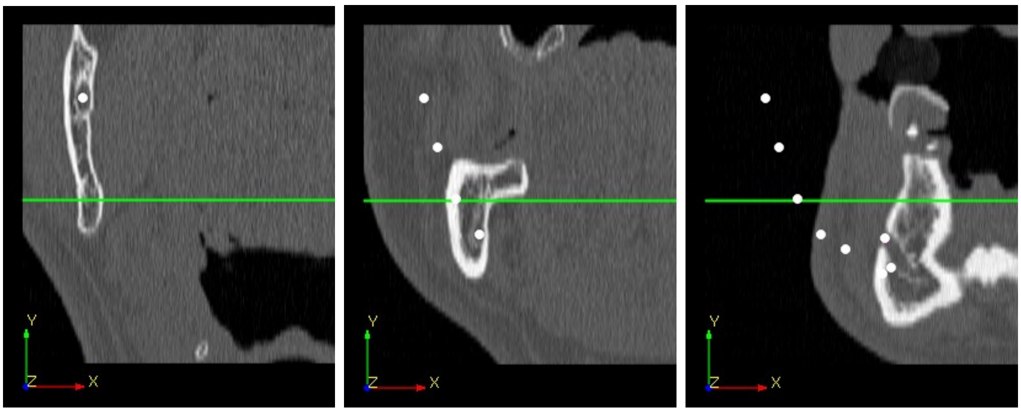

Fig. 5.4. *Control points spotting from mandibular (left) to mental foramen (right)*

As mentioned, it is not necessary to set many selection points (e.g. a sufficient number could be 6 or 7) assuming they are distributed quite uniformly along the the whole path, as the procedure requires. This advantage is due to the implicit smoothness of the Catmull-Rom spline and to its capability to easily approximate complex shapes. Moreover, the feature updates the spline control points dynamically, for every new point identified, thus also the construction of the spline is dynamic, and follows in real time the user decisions. Concerning the building of the related mesh, instead, it has been developed an automatic constructor that, for each pair of adjacent curve line points (the ones achieved from the cspline object in response to the control points provided), assemble an hollow cylinder of specified diameter, attached to the previous adjacent pair one, closing, at the end, the very top and the very bottom of the curve tube model. Naturally, the canal model builder updates itself together with the cspline, in order to keep up-to-date the rendering, letting the user to visualize the mandibular canal dynamically change as a result.

Furthermore, in order to allow the planning doctor to handle possible canal designing errors (e.g. clicking in an undesired point due to a distraction), it has been implemented the option to modify the mandibular canal after having drawn it. At any time, once finished the canal drawing procedure, the user may select to the mandibular canal via mouse click, accessing consequently to its control points and properties (see Fig 5.5), and modify its shape at will, moving, adding, and removing control points.

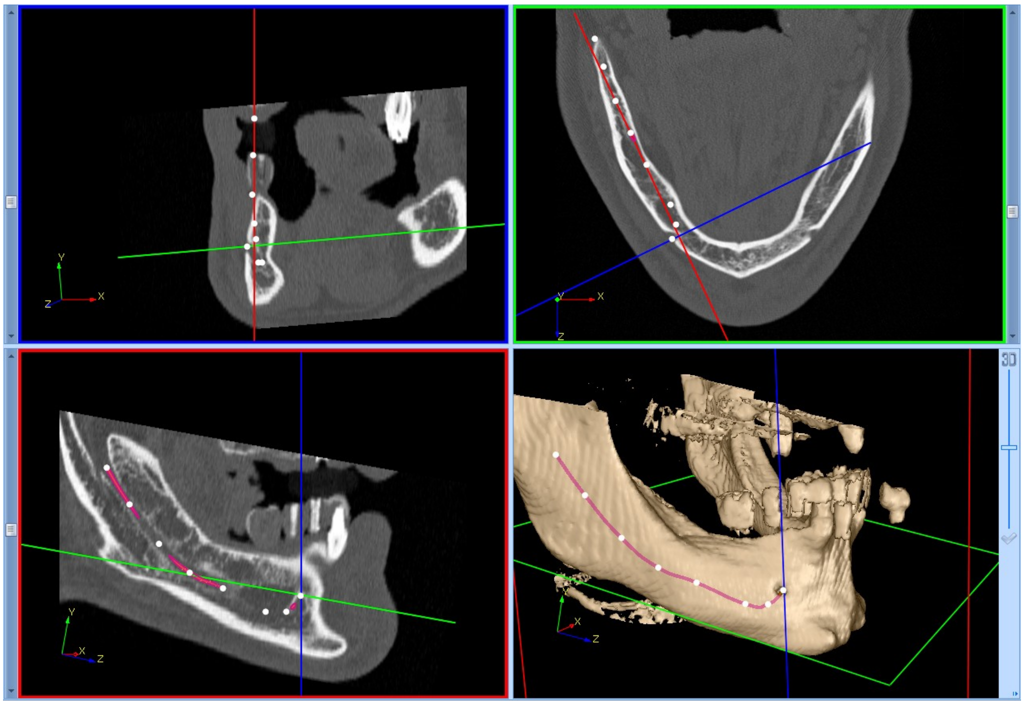

Fig. 5.5. *Selected mandibular canal (fuchsia) with its control points (white dots)*

The technology behind its customizability is the same used for the canal building, thus, also in this case, the user is able to observe its modifications while applying them.

5.2 AUTOMATIC RECOGNITION

Once implemented the mesh canal building technology, thus having the base to support the prospected automatic identification algorithm, it has been defined the methodology to be used in regard of the recognition. Firstly, it has been reviewed the literature about. Two main types of algorithm have been identified: template matching algorithms (Rueda et al. 2006) and self-sufficient ones. An interest approach belonging to the second category is the one proposed by Yau et al. (2008).

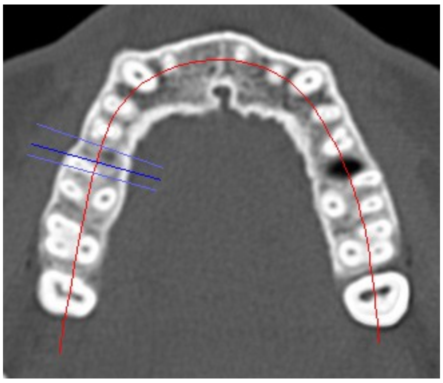

Fig. 5.6. *Panoramic curve (red line)*

The described algorithm is based on the planning software typical multi-view environment (see Section 1.3.1), and consists of automatically scrolling the cross-sectional planes along the panoramic curve (the line that cross-sectional slices are orthogonal to; see Fig. 5.6), starting from the user identified mandibular foramen, and finishing in correspondence of an user defined endpoint (e.g. the mental foramen), analysing each scrolled slice to extract the inferior alveolar nerve region.

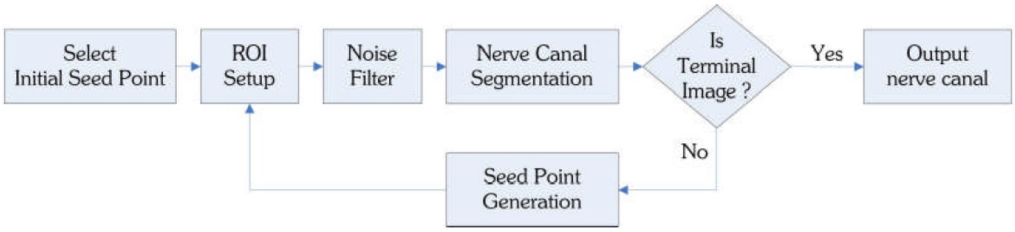

Fig. 5.7. *Flowchart of the adaptive region growing method of Yau et al. (2008)*

The adopted methodology is characterized by the repetition of following steps for each slice analysed:

- Soft tissue definition: a *region of interest* (ROI) is established around a specific point (e.g. the mandibular foramen), called *seed point* (see Fig. 5.8), and the canal inner soft tissues greyscale values are statistically determined using local area based thresholds, thus adaptively:

$$\overline{X} = \frac{1}{N}\sum_{i=1}^{N} x_i \qquad x_i \in ROI$$

$$\overline{x} = \frac{1}{n}\sum_{i=1}^{n} x_i \qquad x_i < \overline{X}$$

$$\sigma = \sqrt{\frac{1}{n}\sum_{i=1}^{n} (x_i - \overline{x})^2}$$

Whereas N is the number of pixels in the ROI, x_i is the greyscale value, $\overline{X}$ is the average of greyscale values in the

ROI, and $\bar{x}$ and σ are respectively the average of greyscale values in the ROI after having removed the influence of the high greyscale values of the bone region and its standard deviation. With the last two parameters is possible to achieve the upper and lower thresholds to identify the soft tissues, respectively $\bar{x}+\sigma$ and $\bar{x}-2\sigma$.

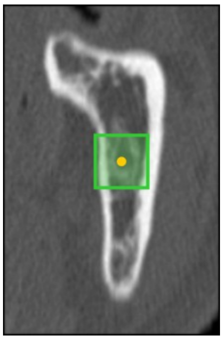

Fig. 5.8. *A region of interest (green) around its center/seed point (yellow)*

- Nerve canal segmentation: the mandibular canal section is determined exploiting the application of a region growing algorithm, starting from the seed point, and using the soft tissue definition range as threshold. The growing filter works analysing the eight neighbours of the starting pixel, and adding to the nerve region the ones that fall within the threshold range, or rejecting them otherwise. Then, this step is repeated from a pixel to another, until all the pixels in the image have been checked.

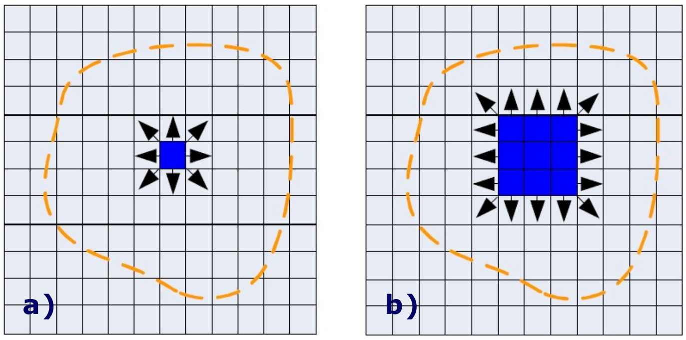

Fig. 5.9. *Region growing algorithm at initial (a) and expansion state (b)*

- Seed point generation: whereas the seed point to begin with is the first point identified by the user (i.e. the mandibular foramen), the subsequent ones are achieved immediately before stepping to the following slice. In order to get the next seed point, that is the seed point on the next cross-sectional image, it is accomplished an intersection between the nerve region of the current ROI and the expected nerve region of the equally positioned ROI in the next slice. The expected region is obtained applying the soft tissue range threshold and keeping every pixel that falls within. The center of the consequent intersected region is the next seed point.

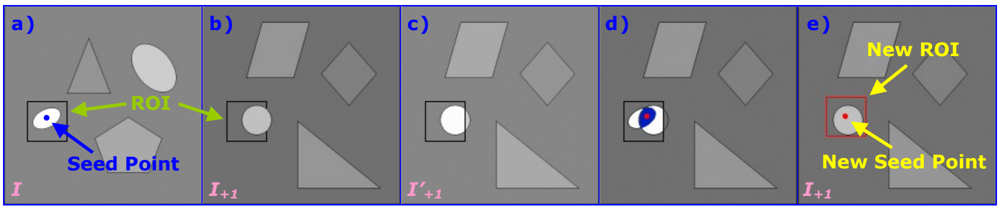

Fig. 5.10. *Seed point generation. a) Current slice nerve region. b) Next slice. c) Threshold filter on next slice. d) Intersected region. (e) New seed point and ROI.*

In consideration of the immediateness and self-sufficiency of this algorithm, and consequently its independence from the application of templates and related training, it has been chosen to start from its approach.

In relation to the different work environment (see Chapter 2), it has been opted for an image processing algorithm able to scan the canal avoiding the need of following the panoramic curve path. This has been achieved building undersized oblique slices orthogonal to the axial ones, characterized by a normal parallel to the view's depth axis (the mandible back-to-front axis) and a starting seed point positioned in correspondence of the user defined mandibular foramen. Then, at each scrolling step, the new oblique slice is centered in relation to the related seed point identified at the end of the previous step. In addition, also the region growing algorithm has been modified. Firstly, the expansion starting area has been extended to the seed neighbourhood neighbourhoods, rather the seed neighbourhood only, in order to increase the probability to pick valid pixels, remaining within a reasonable limit nonetheless (i.e. without risking to unwillingly select pixels outside the canal). Then, the neighbour validation check has been based on its neighbourhood greyscale values mean, instead of its own only, with the purpose of increasing the selection strictness (exploiting the great relevance that the bone high radio-density has in relation to the soft tissues upper threshold definition).

However, whereas the general approach proposed by Yau et al. (2008) is good in theory, it resulted to be not in practice. In fact, after having implemented it in accordance with the described adjustments, and having tried it, an important flaw emerged: during the oblique slices scrolling, the ROI was used to quit the canal in order to wander around within the mandible. As the authors mentioned in the conclusion of their work, this effect may occur in mandibular situations which involve holes and openings along the canal bone surface, and it is due to subsequent ROI shifting towards the canal outer space. In particular, this event happens because the soft tissues outside the mandibular canal share the same Hounsfield radio-density values (see Section 1.1) with the inner ones, therefore the intersection of a ROI nerve region and the expected one on the next slice will relocate the new ROI towards the soft tissues grey density richest area, that is, naturally, outside the thin canal. Notice that this can happen only in absence of bone parts, because otherwise the region growing algorithm would be stopped by the canal surface, preventing to include outer soft tissues in the intersection that identifies the next slice ROI. Yau et al. claim also that this problem is solvable using the ROI itself as boundary area, but, actually, it does not help so much: even using the ROI as boundary constraint, it would allow the new ROI center to be in the same slice related position of the previous one at most, that, after several trials, demonstrated to be enough to fall outside the canal, loosing its track while scrolling forward as a consequence. Consequently, after having studied and verified that those holes and openings are quite common in human mandibles, it has been decided to develop a new algorithm able to manage the mandibular canal irregularities.

5.3 MANDIBULAR CANAL ANALYSIS

The subsequent step towards the development of the algorithm has concerned the analysis of the area of interest, in order to discover the most significant irregularities of the inferior alveolar canal, and its nature in general.

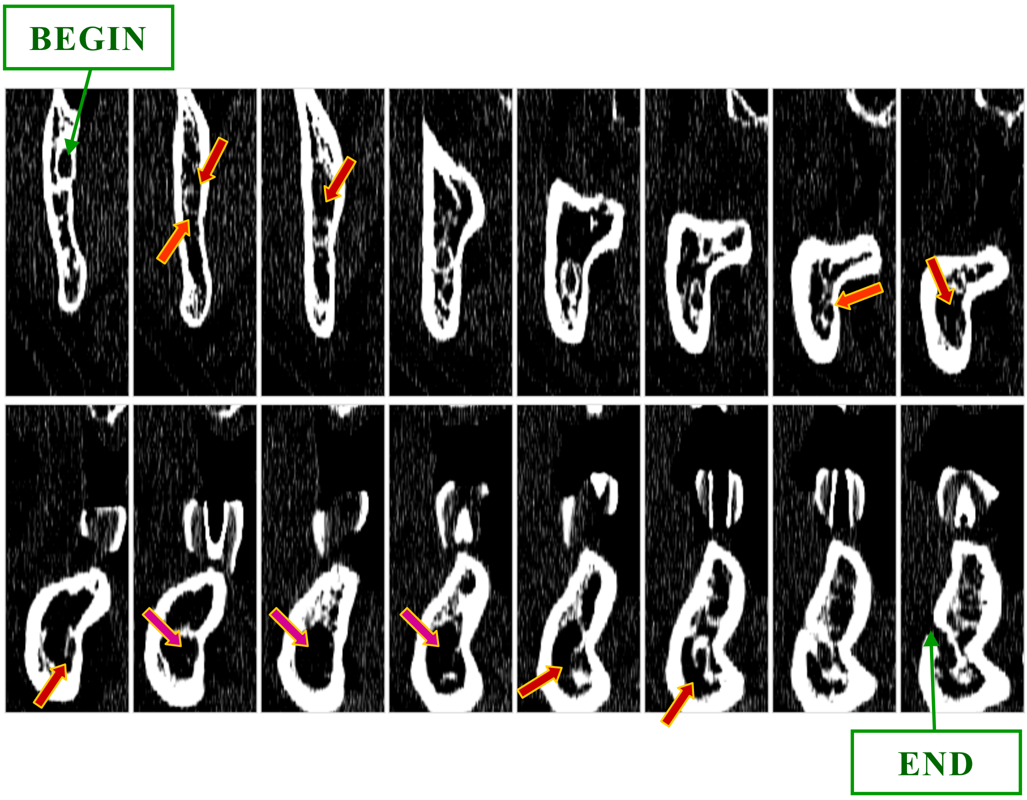

Fig. 5.11. *Irregularities: holes (red), low densities (orange), interruption (purple)*

Analysing many cases of study it has emerged that the mandibular canal it is a quite irregular bone structure, rather than a cylindrical curve one. In general, it retains the tubular shape, but it has not a fixed one, changing from an elliptic-like shape to a circle-approximating one, while varying its size along its path. However, as showed in Fig. 5.11, the most significant irregularities identified are the follows:

- Holes and openings to sub-canals (e.g. it can be *bifid*): gaps of various dimensions can be present along the canal surface, in every direction, and in any number; as previously mentioned, the lack of a bone surface part implies a probable deviation of a path tracking algorithm, due to the misleading soft tissues shared density values.
- Misleading radio-density: the radiographic density values of some portions of the canal surface can be less intense, probably as a consequence of a thinner bone layer; this event may lead to a density misunderstanding, whereas the ambiguous part falls within the defined soft tissues greyscale values range, and consequently to the same situation described about holes.
- Canal interruption and surface disappearance: at a certain point of the mandibular canal path, in almost every mandible, the conduct vanishes, only to reappear in proximity of the mental foramen; the complete absence of the mandibular canal, or rather the big cavernous cavity it fades into, implies the sudden lost of the reference canal walls, becoming an area in which is

unknown how to move through, and consequently it leads almost surely to wrong directions and results.

In conclusion, the inferior alveolar canal resembles more like a wrapping bone surface of variable thickness, rather than an enclosed conduct.

5.4 ALTERNATIVE APPROACH

In consideration of the mandibular canal analysis accomplished, it has been necessary to develop an algorithm able to overcome the problems implied by the conduct irregularities (see Section 5.3). Thus, the prospected path recognition system had to:

1. Remain within the canal also when encountering surface openings (or soft-tissues-like intensity edges in general): this means that it had to move towards grey values richer density areas as before, in order to follow the canal curves, but without departing too much from the conduct path.
2. Manage the complete canal disappearance at an approximately fixed point: this means moving blindly through the following soft tissues pool, and rejoining the conduct path after.

Moreover, the algorithm could not rely on the bone canal surface shape or thickness, as well as to its size, due to its unpredictable and shapeshifting nature. Finally, both of the two prospected tasks implied the need of knowing the conduct path, or an approximation of it, prior to recognise it. Consequently, in order to not change completely the algorithm passing to a template matching one, an alternative solution had to be found.

The idea behind the finally developed algorithm has born comparing the situation to natural and physical phenomena. In particular, it has been compared the recognition system moving along the canal path as a submarine within an underwater caves system, or, better, to a starship inside a burrows system within a space asteroid (due to the lack of any relevant strength vector like Earth's gravity). Furthermore, this starship is able to investigate the neighbouring area only, as if its headlights have a short range and the rest of the cave is wrapped in the darkness. Actually, imaging this, it has been more clear that, for the recognition-algorithm/starship, encountering an hole on the canal surface means simply to run into a crossroads, and, ignoring the path of the conduct, it is a guess the tunnel to enter into. Notice that this is true even knowing the mental foramen location, because not necessarily the canal follows the shortest path to the endpoint, and usually it does not. Thus, the starship would need something that points out the canal path somehow, something to light up the cave, but not from the exit point, because it is hidden and relies in an area reachable only after an ascent (see Fig. 5.12).

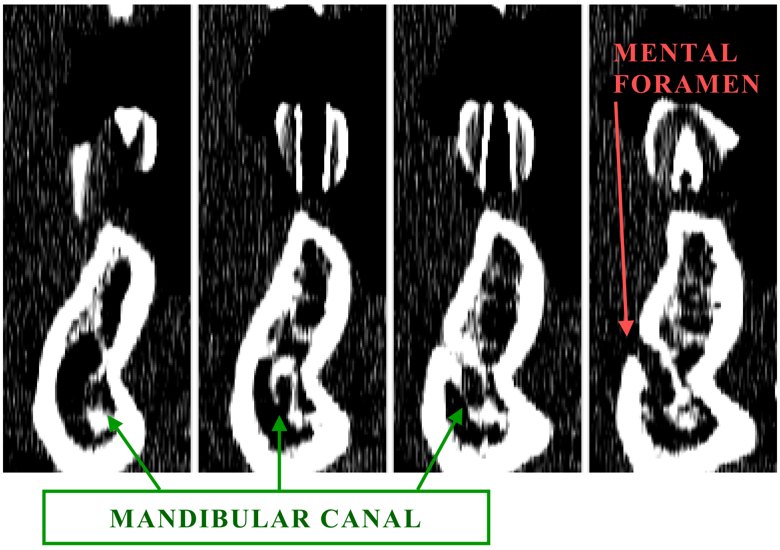

Fig. 5.12. *Mandibular canal ascent towards the mental foramen*

Thinking about the mental foramen ascent, it has been possible to shape the last part of the approach, that actually exploits the climb, but on the other direction. In fact, it has been thought to use the canal ending to insert something into, like throwing a flare down for a well or a subterranean burrow. This idea can be feasible because almost every mandible has that ascent, and even if one has not, the flare would fall near the foramen nonetheless. Moreover, the lighting device has to move for a brief period only, in order to reach the bottom of the ascent, without going lost in the canal interrupting big cavity (see cross-sectional images pointed out by fuchsia arrows in Fig. 5.13).

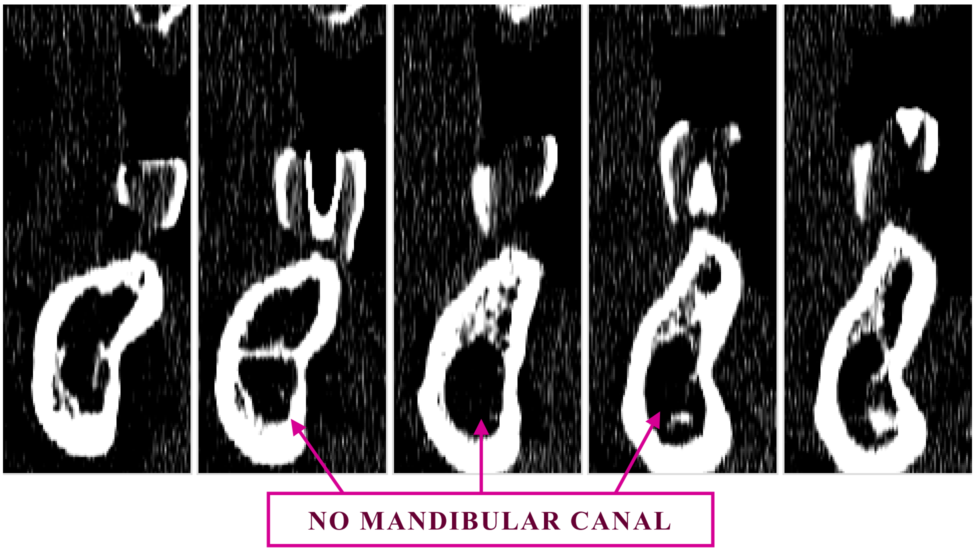

Fig. 5.13. *Canal interruption*

In relation to these considerations, it could be possible to use the thrown flare to identify the bottom checkpoint, achieving a flare-checkpoint current-starship-location difference vector to interpolate with the seed-point to next-seed-point direction, smoothing the starship curves path and keeping it closer the canal lane. However, a simple checkpoint indicator was not enough, because the situation needed different degrees of interpolation, rather than the application of a constant one. In fact, the interpolation effect acted more like an attractive force, but whereas in the final part of the mandibular canal it could be useful, in the first part, on the contrary, it could be disadvantageous. Actually, the first trunk of the canal is often characterized by a turn that cuts the shortest starting-point to checkpoint path, and an attractive force that crosses the bend pathway could lead towards the canal walls, if it is too strong. On the other hand, in order to overcome the cavernous concavity the canal fades into, being attracted by the great density of the soft tissues pool, the starship needs a strong attractive directional force. In regard of this, the flare-like idea has consequently moved toward a magnetic probe or a signal emitter one, for which the attraction force or the radio wave is weaker the farther and stronger the nearer.

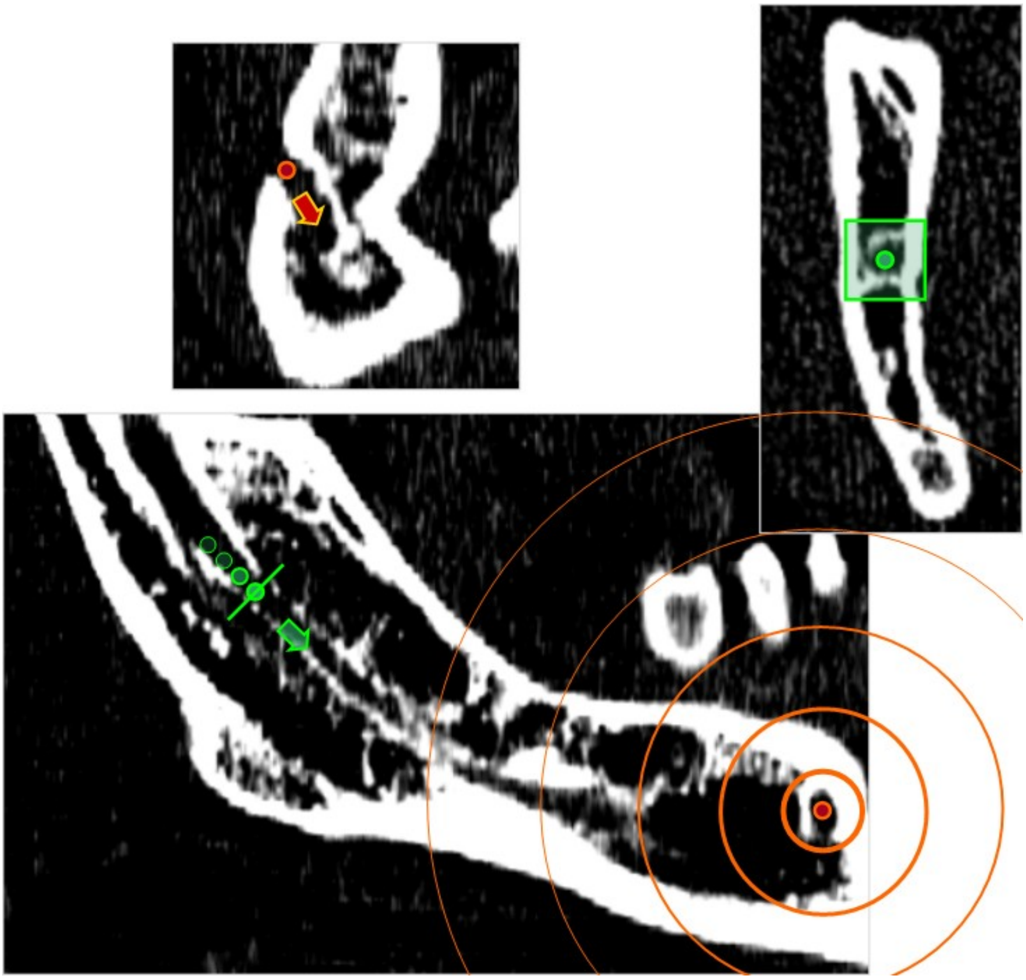

Fig. 5.14. *New approach: the normal probe (green) follows the magnetic one (red)*

5.5 DISCOVERING PROBE ALGORITHM

Following the ideas reported in Section 5.4, it has developed an automatic recognition algorithm that can be divided in two parts: the insertion of a magnetic probe to acquire a checkpoint at the bottom of the exit ascent, and an iron-attracted-like rolling one thrown into the mandibular foramen (see Fig. 5.15). The approach starts acquiring the starting and final points (i.e. the mandibular and mental foramina).

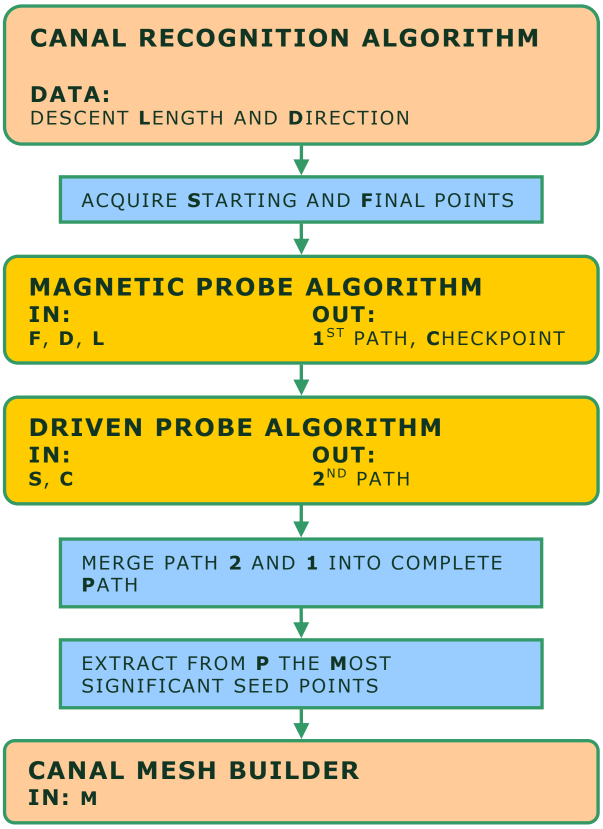

Fig. 5.15. *Canal recognition algorithm*

Then, the first step consists of throwing the magnetic probe into the canal exit: its movement within the canal it is managed similarly to the previously described methodology (see Section 5.2), but with some significant differences. Whereas the algorithm keeps the soft tissues definition procedure, it differs on several aspects:

- Slice sequence: the first slice is centered on the second point identified by the user, and its normal aims at the mental foramen entrance, the direction of which has been achieved as interpolation of the related directions of several cases of study. Then, at each slice scrolling step, the direction is updated with the normalization of the difference vector between the next seed point and the current one. As a consequence, the recognition system is able to move freely, avoiding directional constraints like the previous slice scrolling fixed path, and to follow the lane more precisely as a result.
- Nerve canal segmentation: the region growing method is replaced by a flood labelling one. The first has been abandoned since it can cause the main algorithm to fail in certain situations; in particular, it needs to grow a region from a specific point (i.e. the center of the current ROI) or neighbourhood, analysing its neighbourhood and deciding what to ignore and what to keep, but there is no guarantee that the center area of the current ROI is characterized by soft tissues. Usually, a part of the mandibular canal lane is characterized by a tiny section, but keeping its surface thickness: when this happens, the region growing algorithm has good probability to

pick a bone area in the ROI center, instead of the thin soft tissue one, impeding the algorithm to continue. Instead, a flood labelling algorithm, that consists of labelling closed threshold-defined areas in one full image scan iteration, has not this fault. It scans each pixel of the image, and check if it is not labelled yet and if it satisfies the defined threshold. If the control fails, it passes beyond, otherwise it uses that pixel as starting point for a growing filter: similarly to the region growing algorithm, it checks the neighbours, labelling the threshold-satisfying ones, ignoring the others, and repeating the procedure in the neighbourhood of each labelled one. Then, it continues the scan, in order to find other threshold-fulfilling regions, labelling them with different tags. Practically, it acts flooding the image, filling every interesting area like a pool as a result. This algorithm, finally, has been adapted to the situation. Firstly, the threshold has been defined as the range of soft tissues greyscale values. Then, the algorithm has been concluded with the selection of the labelled area nearer to the ROI center, that represents the soft tissues region looked for.

- Seed point generation: similarly to the previously adopted methodology (see Section 5.2), the seed point to begin with is the first point identified by the user (i.e. the mandibular foramen), whereas the subsequent ones are achieved immediately before stepping to the following slice. Also in this case, in order to get the next seed point, that is the seed point on the next cross-sectional image, it is accomplished an

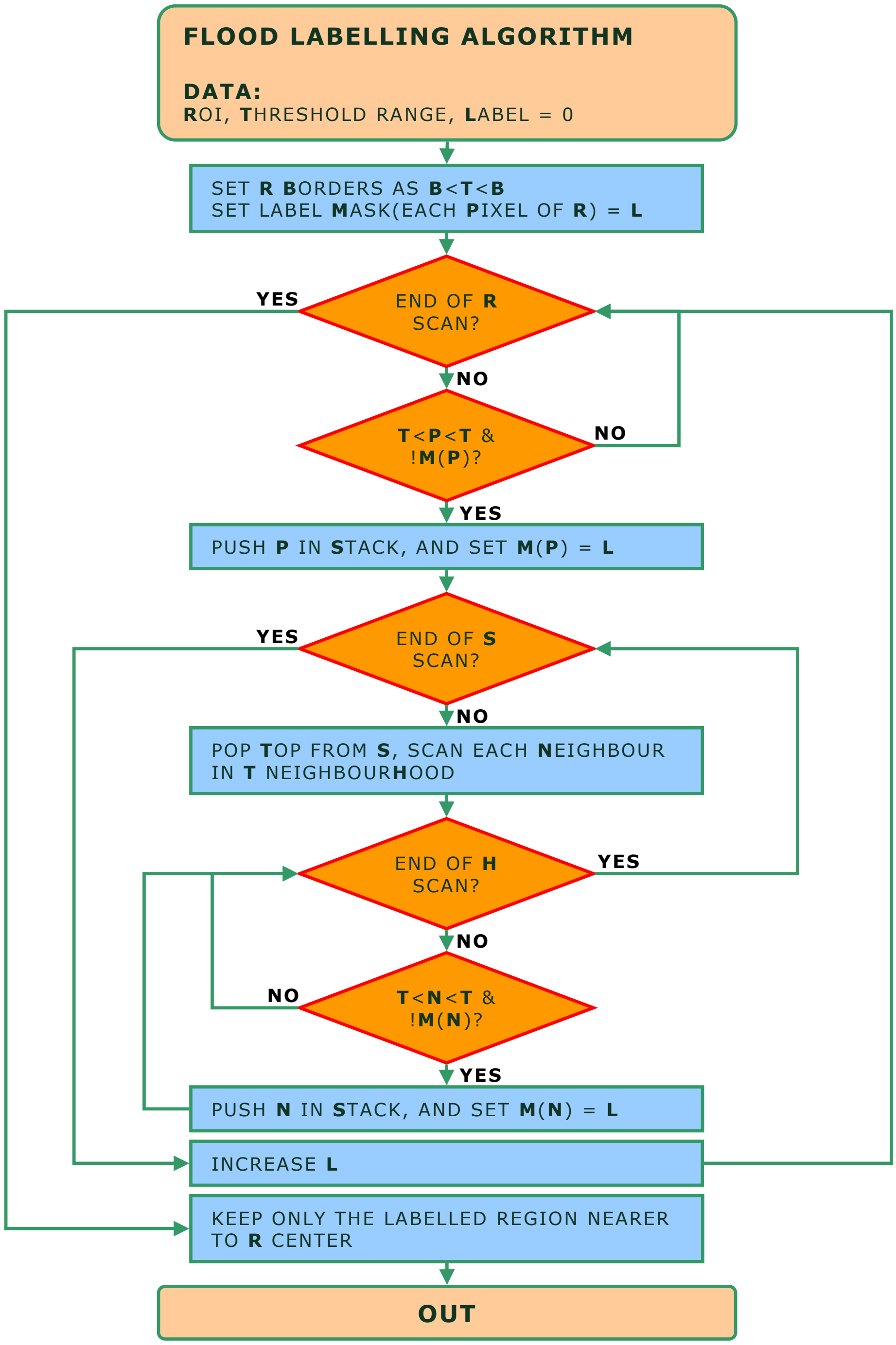

Fig. 5.16. *Flood labelling algorithm*

intersection between the nerve region of the current ROI and the expected nerve region of the equally positioned ROI in the next slice. However, differing from the previous approach, the expected region is not obtained applying a simple threshold filter, rather, instead, a flood labelling segmentation, calculating and using the expected ROI soft tissues greyscale values range as threshold parameter. This substitution has been performed to impede that soft tissues out of the canal may influence the intersection center (it can happen in presence of thin canal edges), and the slice scrolling direction as a result. The center of the consequent intersected region is the next seed point.

- Small noises handling: it has been implemented a simple system to handle small image noises along the canal, in order to improve the algorithm possibility to not be blocked. Actually, image artifacts are not unusual in computed tomographies, like scattering (white bright areas due to radio-reflecting materials) or incongruent densities (e.g. patient moving during the scan), and encountering them could impede the algorithm to proceed (e.g. a sudden scattering through the canal would be identified as bone area from the algorithm, preventing it to continue in that direction); to this regard, two handlers have been implemented. Concerning the nerve canal segmentation, the algorithm may undo an image analysis step, and repeat it using the previously stored direction. About the next-seed-point generation, instead, the algorithm is able to move forward with very short leaps, in order to overcome sudden unexpected noises.

- Travel extent: the advance of the probe is limited to a short stretch, in order to not overcome the foramen ascent bottom, avoiding to finish in the soft tissues pool as a consequence. The length of the distance to be travelled has been calculated as mean of the mental foramen ascents of several cases of study, and then converted in number of steps to progress.
- Step length: the step pass is significantly longer; this is necessary to prevent hairpin turns, whereas in the previous approach could not happen due to the compulsory scrolling of the slices towards the front of the mandible.

In this way, the probe rolls down along the descent, only to stop approximately at its bottom, generating the needed checkpoint. After that, the approach contemplates to throw the second type of probe into the mandibular foramen (pointed out by the first user defined point). This probe works similarly to the magnetic one, but for few differences:

- Slice sequence: the first slice is centered on the first point identified by the user (i.e. the mandibular foramen), and its normal is defined by the difference versor between the final and the starting point. Then, at each slice scrolling step, the direction is initially updated with the difference versor between the next seed point and the current one, and then interpolated with the current-seed-point-to-checkpoint normalized vector. During this interpolation, however, the second vector is modified by a ratio factor $r = 1.0 - \left| d_{mc} \div d_{ms} \right|$, whereas d_{mc} and d_{ms} are the distances respectively between the magnetic probe and the current seed point, and the magnetic probe and the starting point, consequently achieving different attraction forces in relation to the position within the canal. Finally, the next seed point is updated in relation to the new direction got. As a result, the recognition system is able to remain within the lane and to overcome the canal interruption area, reaching the checkpoint pointed out by the magnetic probe.

- Travel extent: the length of the route the probe has to travel is calculated exploiting the distance between the magnetic probe and the mandibular foramen (the entrance of this second probe), in order to reach at least the interruption of the canal and at most the checkpoint, and then it is converted in number of steps to progress. Thus, the obtained length is an approximation, but it is enough for the algorithm need. In fact, when the probe travel is concluded, the algorithm is able to finish the uncovered path connecting this second probe to the magnetic one along the straight line between them, that is, actually, the only way the probes could correctly join anyway.

As a result, the attraction force implied by the magnetic probe allows the rolling one to keep itself along the canal lane, impeding to quit through holes (or soft-tissues-like density edges), and it becomes strong enough to guide it towards the checkpoint after the canal disappearance. When the second probe finishes its route, the algorithm merges their respective paths, achieving the mandibular canal one.

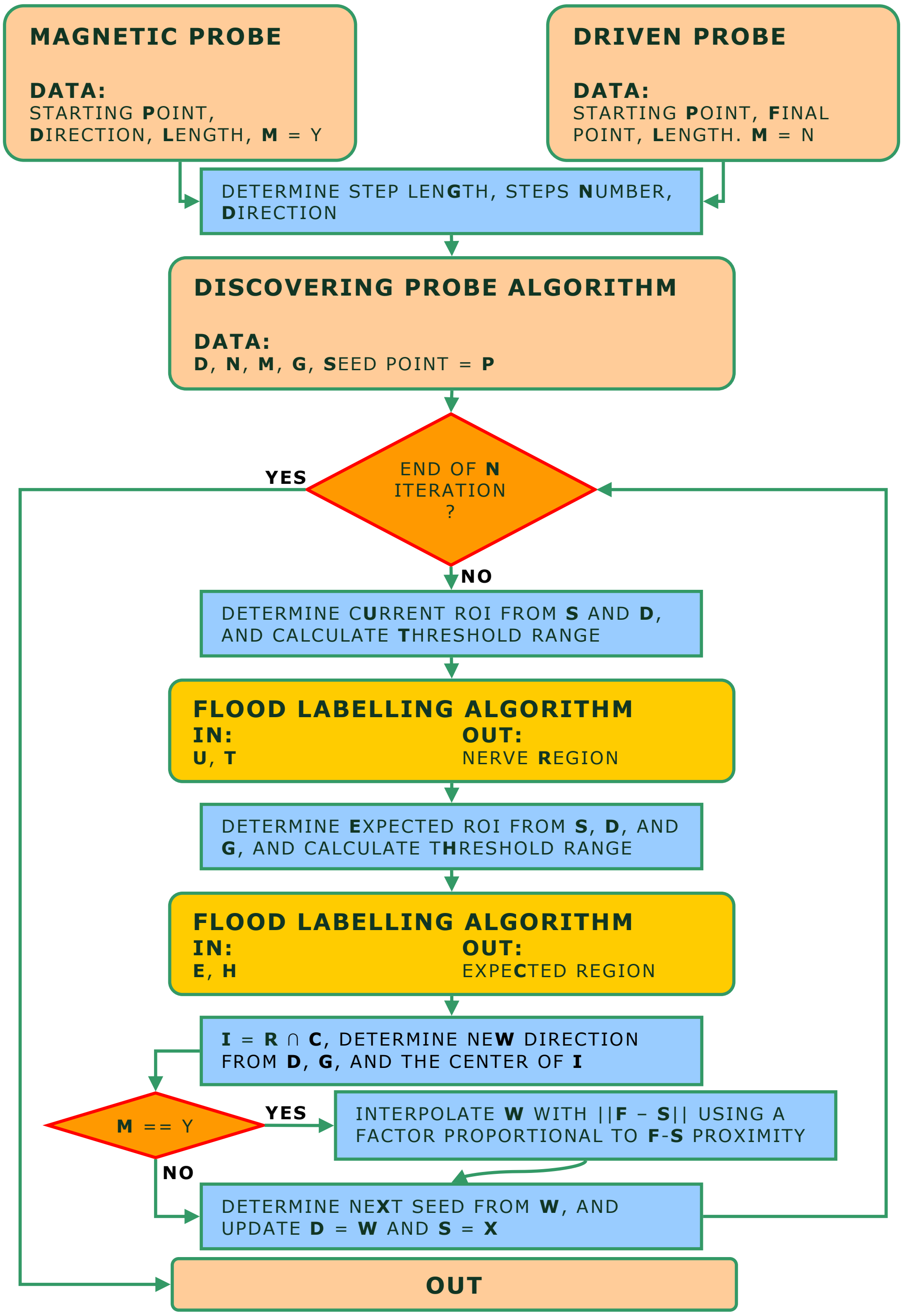

Fig. 5.17. *Discovering probe algorithm*

Finally, the whole list of seed points, that actually define the path, is processed by a proper procedure that selects the most significant ones, providing them as algorithm results. These points, then, are passed to the canal mesh builder (the same used in the manual recognition) as cspline control points (see Sections 5.1.1, 5.1.2), obtaining the reconstructed model and its rendering as a consequence.

5.6 CANAL RECOGNITION EVALUATION

In order to evaluate the correctness and reliability of the automatic recognition algorithm, it has been decided to ask an implantologist to try the developed functionality on some cases of study, in order to achieve his/her evaluation about it. In particular, this task has been assigned to Dr. Franchini, renowned for his knowledge about and important contributions to the oral implantology field, taking advantage of the availability he offered (see Section 1.3).

The first step of the adopted procedure, before the evaluating phase, has concerned the *windowing*. Quoting from literature, windowing is the process of using the calculated Hounsfield Units (HU) to make an image. A typical display device can only resolve 256 shades of grey, some specialty medical displays can resolve up to 1024 shades of grey. These shades of grey can be distributed over a wide range of HU values to get an overview of structures that attenuate the beam to widely varying degrees. Alternatively, these shades of grey can be distributed over a narrow range of HU values (called a "narrow window") centered over the average HU value of a particular structure to be evaluated. In this way, subtle variations in the internal makeup of the structure can be discerned. This is a commonly used image processing technique known as contrast compression. For example, to evaluate the abdomen in order to find subtle masses in the liver, it is possible to use liver windows. Choosing 70 HU as an average HU value for liver, the shades of grey can be distributed over a narrow window or range. 170 HU can be used as the narrow window, with 85 HU above the 70 HU average value; 85 HU below it. Therefore the liver window would extend from -15 HU to +155 HU. All the shades of grey for the image would be distributed in this range of Hounsfield values. Any HU value below -15 would be pure black, and any HU value above 155 HU would be pure white in this example. Using this same logic, bone windows would use a "wide window" (to evaluate everything from fat-containing medullary bone that contains the marrow, to the dense cortical bone), and the *center* or *level* would be a value in the hundreds of Hounsfield units. To an untrained person, these window controls would correspond to the more familiar "Brightness" (*Window Level*) and "Contrast" (*Window Width*). Actually, the functionality to manage and decide image brightness and contrast (see Section 2.2.4) has been implemented in the software with this purpose, that is to allow the user to highlight/enhance the visibility of image areas in which he/she is interested in. However, this feature has a greater importance in regard of image analysis and recognition algorithms, like the automatic markers identification algorithm (see Section 4.2.1) and the mandibular canal recognition one, because their effectiveness and the goodness of their results strongly depend on the quality of the image. Thus, because the inferior alveolar nerve canal is not necessarily well highlighted with the software default Window Width/Level (W/L) setting, it is essential to adjust it, in order to emphasize the canal edges. Consequently, many windowing settings have been tried, for each tested case of study, with the intention of framing each dataset range of working W/L pair. In Table 5.1 are shown the maximum and minimum W/L pair combinations which the canal is well identified for, in regard of each one of the seven mandible-concerning CT datasets the recognition feature has been tested on.

TABLE 5.1. CANAL EMPHASIZING MAXIMUM AND MINIMUM WIDTH / LEVEL COMBINATIONS

Tested sets				W/L Combinations			
#	*Number of slices*	*Interslice value (mm)*	*Pixel size (mm)*	*Min W / Min L*	*Max W / Max L*	*Max W / Min L*	*Min W / Max L*
1	70	1.0	0.250	2500 / 24500	65535 / 45500	26000 / 16500	6000 / 26500
2	61	0.8	0.234	5500 / 25500	28000 / 45500	18000 / 20500	500 / 35500
3	50	1.0	0.250	7500 / 27500	28000 / 45500	18000 / 20500	500 / 35500
4	108	0.5	0.250	7500 / 24500	3500 / 29500	20000 / 20500	500 / 27500
5	62	0.8	0.234	5500 / 22500	13000 / 28500	26000 / 14500	500 / 27500
6	107	0.5	0.250	7500 / 23500	23000 / 35500	20000 / 20500	2500 / 33500
7	51	1.0	0.250	500 / 25500	60000 / 42500	26000 / 16500	500 / 29500

After having accomplished this task, many other W/L combinations have been tried in order to define a single W/L pair that worked with every tested dataset, exploiting the previously achieved W/L boundary values to circumscribe the search. The obtained W/L pair, positively shared by all the seven datasets, has been to 9000/27500. These values have been set as default W/L pair to be used by the software's canal automatic recognition functionality, with the purpose of easing the tester evaluation task, and aiming at possibly cover a good amount of CT cases in regard of correctly emphasizing the inferior alveolar nerve canal.

The results of the feature testing have been reported in Fig. 5.18-5.32. The mandibular canals shown have been achieved by the assigned implantologist through the use of the automatic recognition feature developed. For each tested dataset, both the right and the left inferior alveolar nerves identifications have been accomplished, and, for each one of them, at least two views have been presented. The oblique ones approximately cut the canal longitudinally, with the aim of showing the most possible of its path, and are characterized by the software default W/L pair (65535/32762), the same presented to the user during the planning (but customizable through the brightness/contrast modifier functionality, see Section 2.2.4). The 3D views, instead, show the selected mandibular canal model (purple line plus white control points) within the 3D reconstructed surface of the bone structure. An exception has been done in regard of the oblique view shown in Fig. 5.26, that has been achieved through a W/L pair of 9000/27500 (the values set to be used by the recognition algorithm), in order to highlight the shadow effect that implied the recognition algorithm to depart from the canal (red circumscribed area on the left of Fig. 5.26). This effect is a consequence of the strong scattering, due to a radio-reflective material, that is possible to observe in the 3D surface reconstruction on the right of Fig. 5.26 (explosion-like area on the top of the mandible model). In regard of this effect, other two views, concerning the same area, have been reported, with the aim of clarify better the problem caused by the noise (see Fig. 5.27).

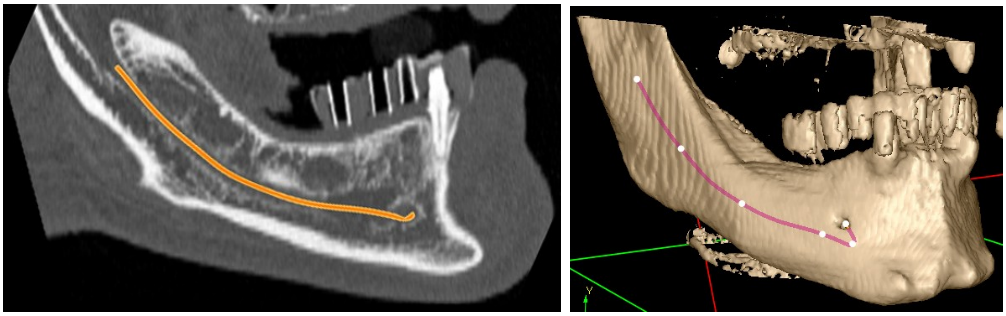

Fig. 5.18. *Right mandibular canal automatic recognition (Set 1)*

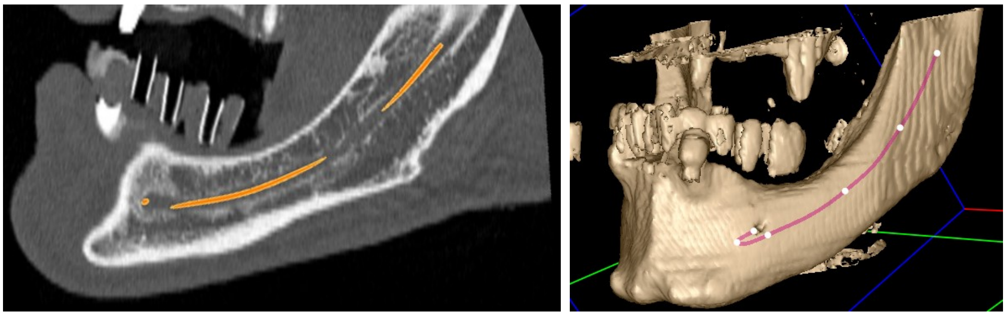

Fig. 5.19. *Left mandibular canal automatic recognition (Set 1)*

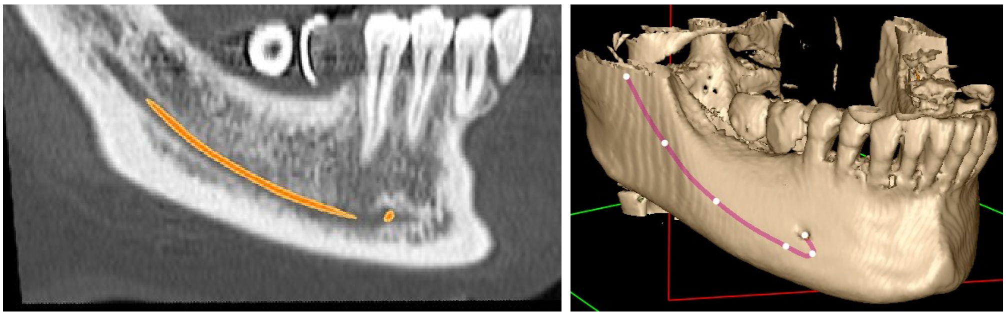

Fig. 5.20. *Right mandibular canal automatic recognition (Set 2)*

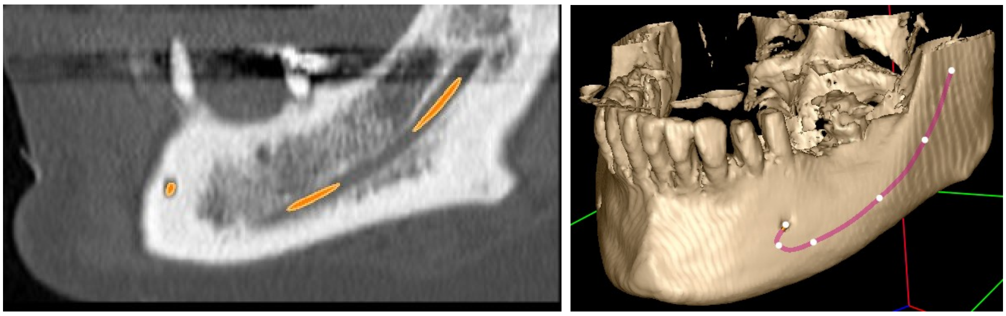

Fig. 5.21. *Left mandibular canal automatic recognition (Set 2)*

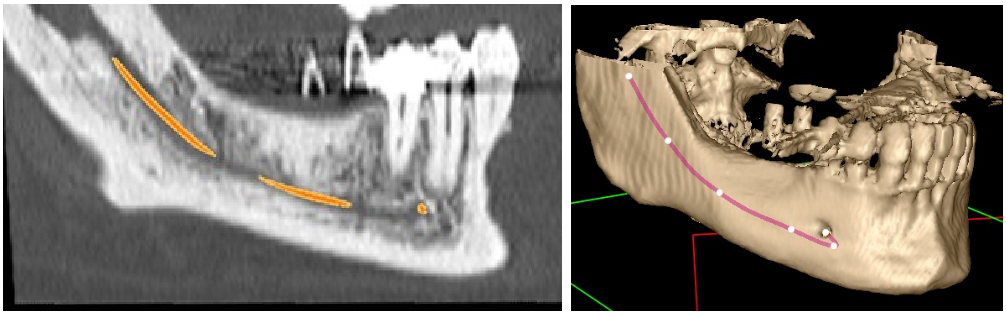

Fig. 5.22. *Right mandibular canal automatic recognition (Set 3)*

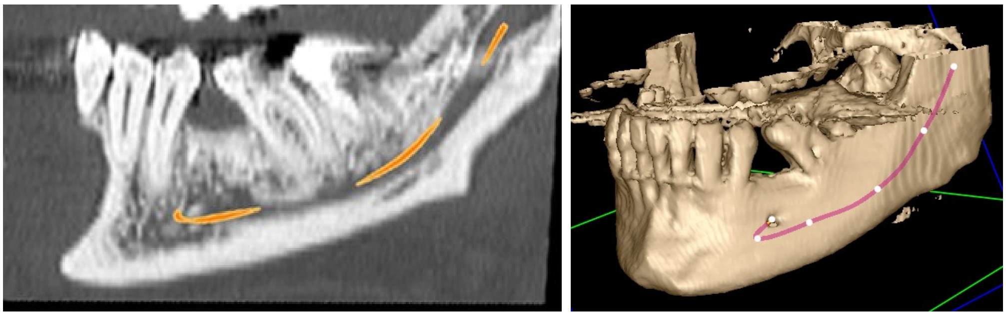

Fig. 5.23. *Left mandibular canal automatic recognition (Set 3)*

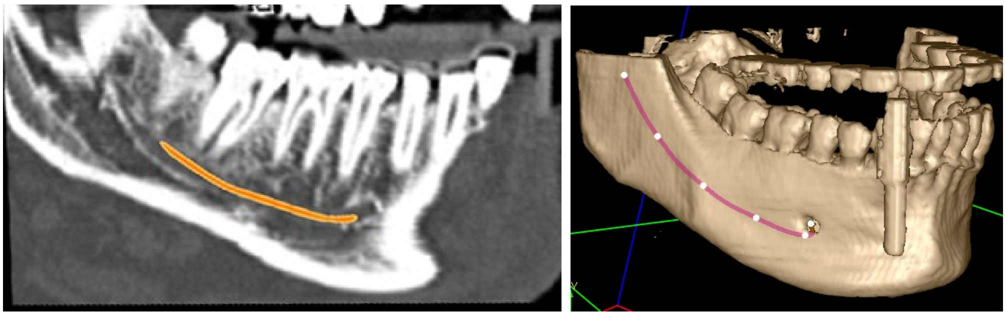

Fig. 5.24. *Right mandibular canal automatic recognition (Set 4)*

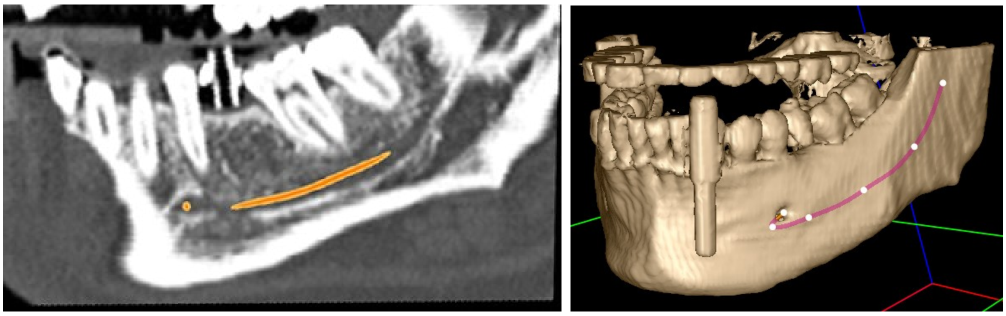

Fig. 5.25. *Left mandibular canal automatic recognition (Set 4)*

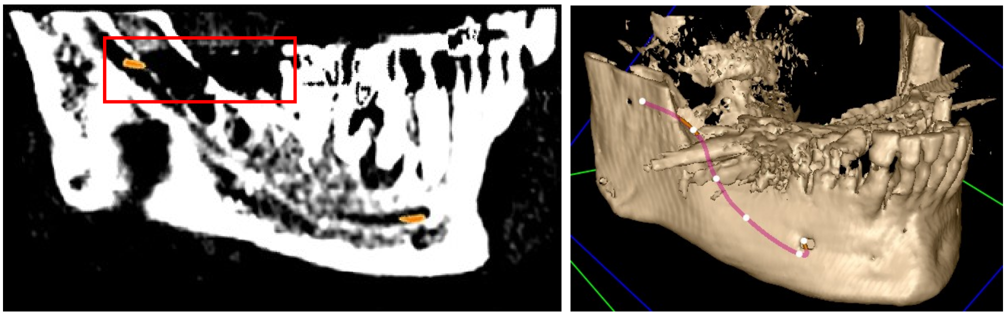

Fig. 5.26. *Right canal automatic recognition (Set 5) and shadow noise (red)*

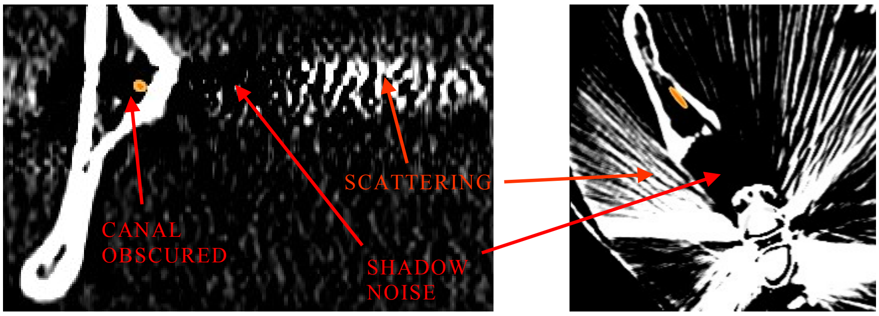

Fig. 5.27. *Oblique (left) and axial view (right) of the canal hiding shadow effect*

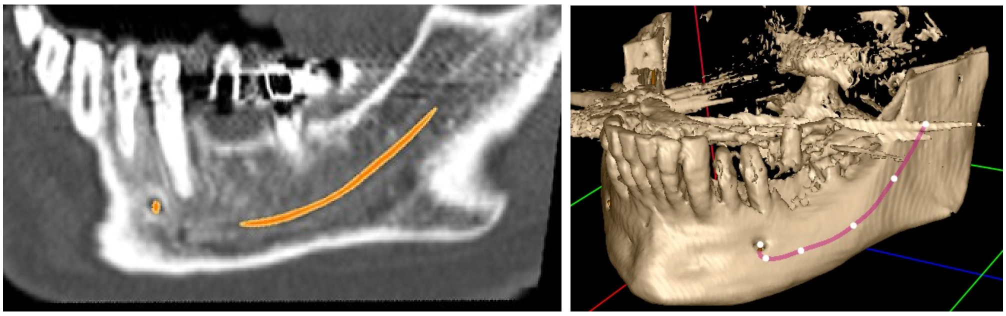

Fig. 5.28. *Left mandibular canal automatic recognition (Set 5)*

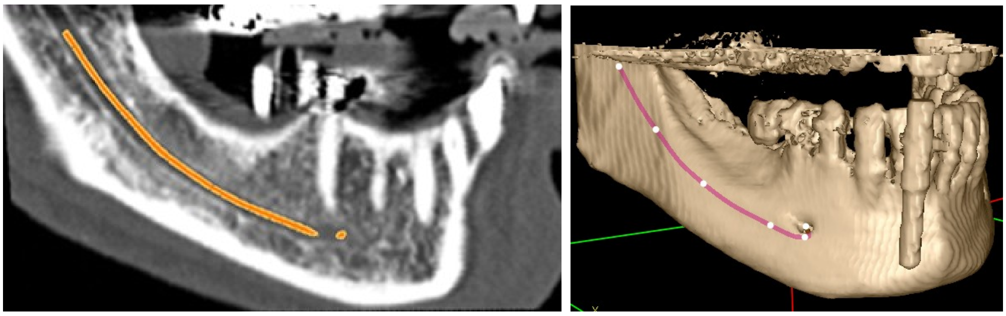

Fig. 5.29. *Right mandibular canal automatic recognition (Set 6)*

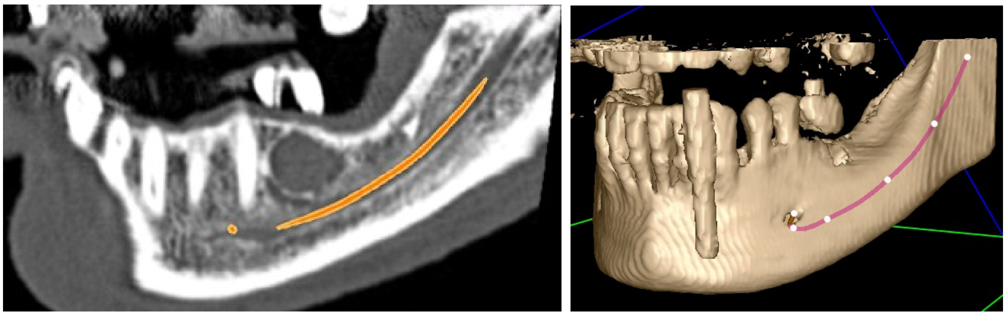

Fig. 5.30. *Left mandibular canal automatic recognition (Set 6)*

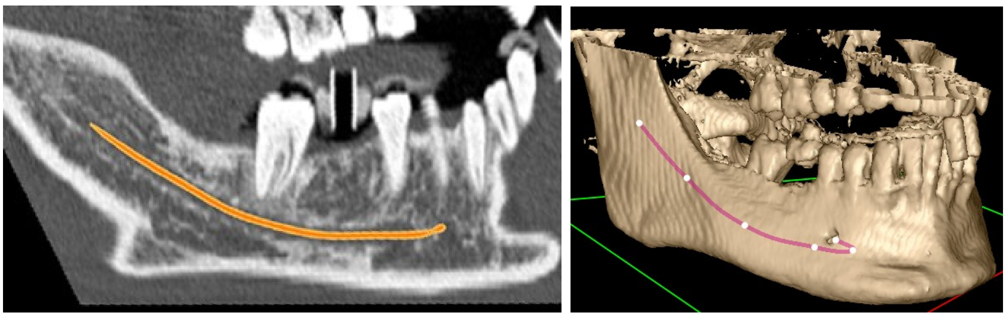

Fig. 5.31. *Right mandibular canal automatic recognition (Set 7)*

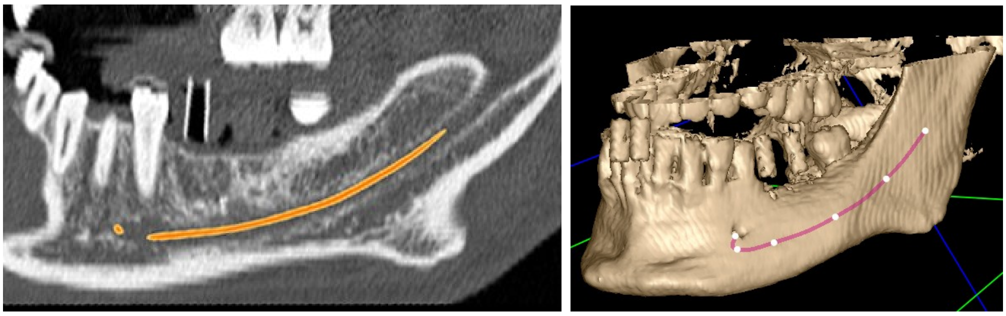

Fig. 5.32. *Left mandibular canal automatic recognition (Set 7)*

As showed and mentioned before, only one mandibular canal on 14 could not be properly recognised, due to an extreme noise effect that obscured it. It is in regard of this kind of situations that the possibility to manually identify or modify the inferior alveolar nerve assumes a relevant importance, and in prevision of which it has been implemented for (see Section 5.1). Concerning the 13 successful tests, instead, the assigned implantologist confirmed the correctness of the mandibular canals automatically recognised by the functionality. Finally, he reviewed the automatic recognition feature as a very useful tool, that allows the user to highlight a fundamental anatomy, letting to perform a safe and correct planning, easing and speeding up the operations needed to its identification.

CHAPTER 6: ROBOT INTERFACING

In order to complete the overall approach, the application has been interfaced to an anthropomorphic robot. The whole procedure, in fact, aims at giving the user the possibility to analyse the mouth of patients without the need of invasiveness, but keeping the freedom of planning through 3D simulation functionalities. The approach, however, does not finish with the diagnosis part, and, as mentioned in Section 2.1, it has been thought to bring the complete implant planning, along with the software precision (Chiarelli et al. 2010b), to the surgical act. Actually, the step beyond the implantological simulation consists of building a surgical template through the use of a drilling bur driven by a 5-axes robot. Then, the surgical guide achieved, based on the dentist implant planning, will be exploitable during the surgical phase to guide with precision the hands of the surgeon. In the following, the methods needed to design the described procedure and develop the most proper solution are discussed.

6.1 STENT-ROBOT INTERFACING DEFINITION

Nowadays, the possibility to achieve a reliable physical reproduction of the bone model of a dental arch through rapid prototyping is an important chance (Barker et al. 1994; Bianchi et al. 1997; Bouyssié et al. 1997; Choi et al. 2002; Klein et al. 1992; Kragskow et al. 1996; Lill et al. 1992). Excluding any metal scattering presence, the prototyped object correspond to a perfect replica of the patient anatomy. In a correlated previous research, Sansoni (1999) states that any prosthodontist can use that prototype as a model, being able to produce a very precise bone-supported stent, perfectly wearable on the patient arch after soft tissues detachment, and, consequently, that it is viable to use that solid model to transfer planned data onto.

Fig. 6.1. *Bone-supported surgical stent with milling vectors oriented guides*

It results that it is possible to obtain a surgical template equipped with metal hollow cylinders orientated along their own milling vector and correctly calibrated on the bur-probe diameter that the surgeon will use during the surgical act (see Fig. 6.1). However, Sansoni also reports that, despite the advantage of the system to transfer to the surgical act the precision achieved through a correct implant planning on a proper and isotropic work context, there are some clear disadvantages:

- the stent is bone-supported, implying a certain amount of surgical *invasiveness*, above all in multiple edentulism cases;
- if any metal scattering is present (particularly near the occlusal plane), the prototyped model is consequently quite less reliable due to the lack of anatomical data;
- the production cost of the anatomical model is significant in relation to the overall cost of an implant-prosthetic operation.

In relation to these considerations, Sansoni switched the system approach on an alternative solution, that returns an ideal stent as a result (not invasive, precise, and cheap). The described method is based on the use of a mechanical (robotized) utensil, whose arm bur equipped handpiece is intended to drill a "virgin" stent, properly placed in the utensil explorable volume, in order to reproduce physically the software simulated relation between anatomy and implants. The virgin stent is obtained replicating the mucosa-supported radiological one on the same diagnostic wax-up, thus it will be mucosa-supported too, and consequently not invasive as well. Moreover, the independency of the surgical stent from the bone structure radiography allows to avoid the scattering problem as well as the stereolitography production cost. Sansoni explains that the critical side of this approach it has been about the virgin stent placing within the working volume of the arm, and the related stent-robot alignment definition, reporting the necessity to match the robot coordinate system origin to a correspondent reference frame, in the dataset, which the anatomical model within can be correlated to. The adopted solution has consisted in installing two parallel titanium solid cylinders into the radiological mask, providing, as a consequence, a coordinate system which the milling cylinders can be defined in relation to.

Fig. 6.2. *Radiological stent equipped with reference titanium markers*

Then, a virgin replica of the radiological stent, equipped with the same pair of titanium markers, has to be placed on the robot reference origin, completing the needed coordinate systems matching (the milling cylinders will have the same space coordinates and the same rotation scalar values in relation to both the robot reference zero and the origin of the titanium markers reference frame within the volumetric dataset). As a consequence, Sansoni determines that, concerning the robot, the discussed system can be reduced to an handpiece positioning problem in accordance to coordinates (x,y,z) and rotations (tilt and turn). At last, he designs a proper 5-axes robotized anthropomorphic arm (see Fig. 6.3) able to accomplish the required drilling, demonstrating also its task feasibility (proving solution existence and uniqueness for the *Inverse Cinematic* problem involved).

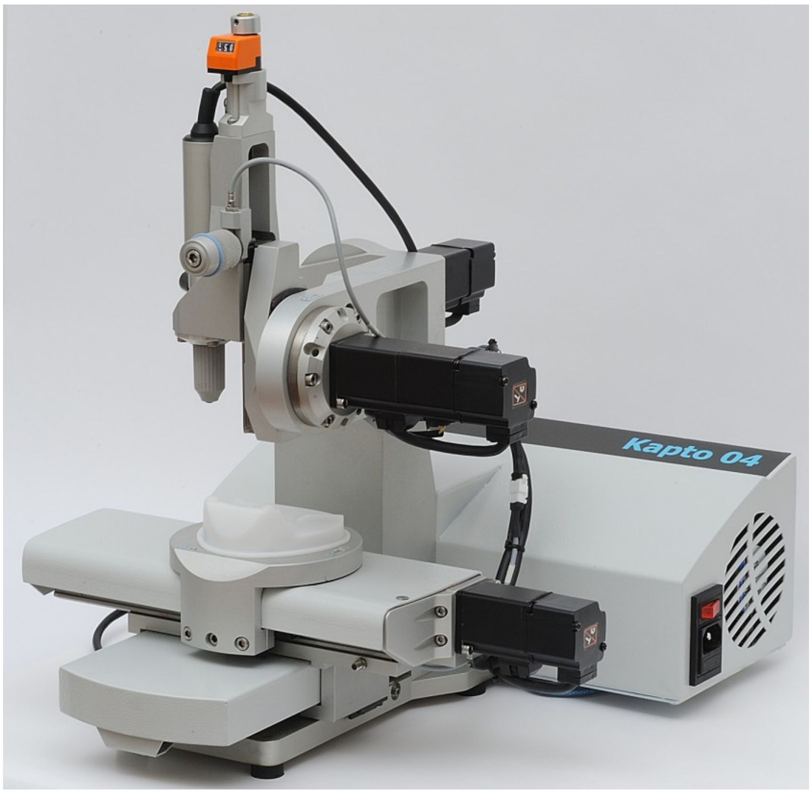

Fig. 6.3. *The 5-axes robotized arm*

6.2 IMPLANTS TRANSFER

In consideration of the advantages of the approach proposed by Sansoni (see Section 6.1), it has been decided to start from it to define the planning transfer method. Once designed the template reference frame, planned the stent-robot alignment, and programmed the engines drivers to translate coordinates into rotations (Sansoni 1999), it remained to define the software output in accordance with the specified requirements. In the 3D world context of the software, each implant is identified by a position (the model center), a quaternion defined orientation, and a 3D mesh; these data are dynamically stored in the implants class instances. Consequently, the application can easily get the output information needed by the robot. In fact, the implant center provides the required coordinates (x,y,z), whereas we can obtain the rotations (tilt and turn) calculating the angles between the implant axis and the system horizontal axes. However, before to transfer these data to the robot interface, the software has to modify them in order to be in accordance with the stent reference frame. Actually, we have designed the radiological/surgical template to have a reference frame suitable to the robot coordinate system, but the software 3D environment kernel has been developed to manage an its own coordinate system. More specifically, its system coincides with the 3D world origin, having direction axes that are intuitive for the user and typical of CAD applications. Thus, every object within is defined in relation to this coordinate system, that almost always does not correspond to the stent reference frame inside the dataset. As a consequence, the application needs to change the coordinates in accordance with the anatomy related reference frame, before to pass them to the robot. In order to accomplish this task, it has been implemented a feature to recognize the reference frame of interest (see Fig. 6.4). With this functionality the user identifies on the axial plane the top and the bottom of the user-left titanium reference frame marker, and the top of the right one, clicking in the circular section center at the proper height. The three spotted points detect a plane with its own normal, achieving, in fact, the needed coordinate system to correlate anatomy and implants to.

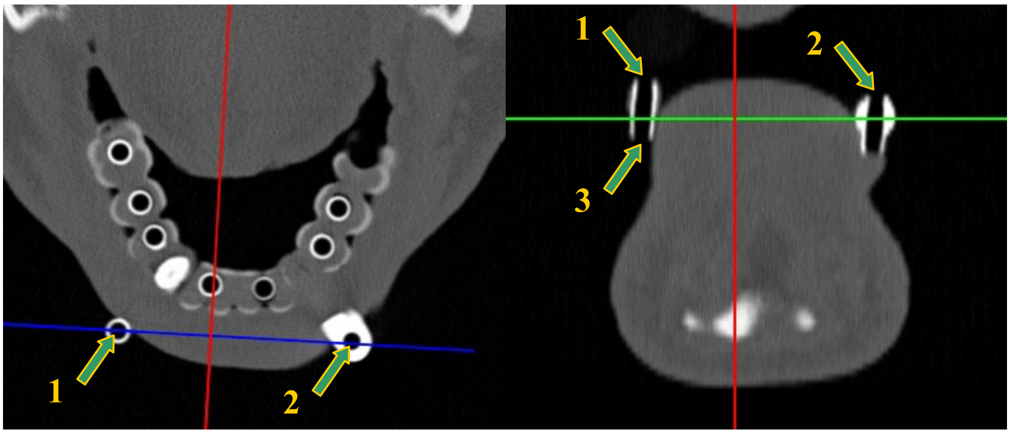

Fig. 6.4. *Stent reference frame identification*

The software is then able to change implants data (position and orientation) in accordance with the identified reference frame, applying the proper geometrical transformations (translations and rotations). Then, the application provides the models half-heights, achieved from the implants 3D meshes, letting the robot being able to drill each planned implant to the correct depth. Finally, before to pass the parameters to the utensil interface, they are properly modified in accordance to the dental arch nature. In fact, whereas a virgin surgical stent placed in the robot platform has a determined relationship with the utensil reference frame (the outer radio-opaque markers), its radiographic representation does not in regard of the software 3D world coordinate system. This is due to the axial camera management in the software, that visualizes the dataset from different points of view, in relation to the examined dental arch (maxilla or mandible). Consequently, considering that the practical procedure of the reference frame identification software feature is constant (user-left marker top and bottom centers, user-right marker top center), the selected coordinate system does not necessarily match with the stent-robot one. To solve this problem, the parameters are modified in accordance of both the robot axes directions and the real stent reference frame orientation. In Fig. 6.7 it is shown a flowchart of the change of the coordinate system during the whole procedure.

In conclusion, after having identified the reference frame radiographic representation, the user just needs to select the desired planned implants in the alignment window and to confirm the data transferring through the proper button.

Fig. 6.5. *Base interlocking system on the robot platform and robot axes directions*

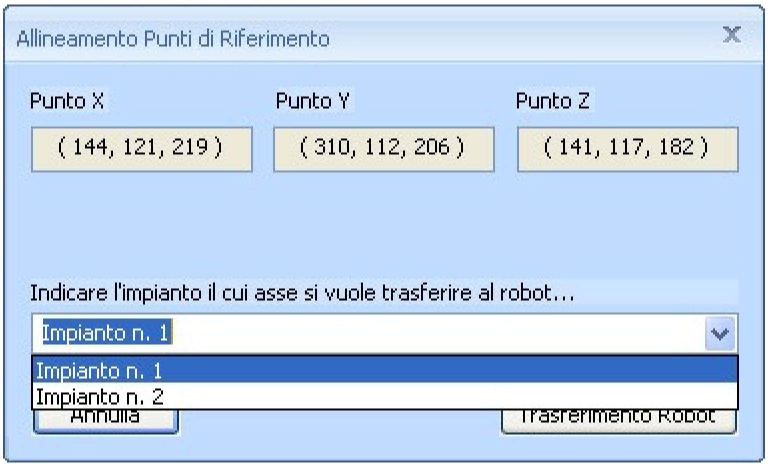

Fig. 6.6.*Software interface for implants planning transfer*

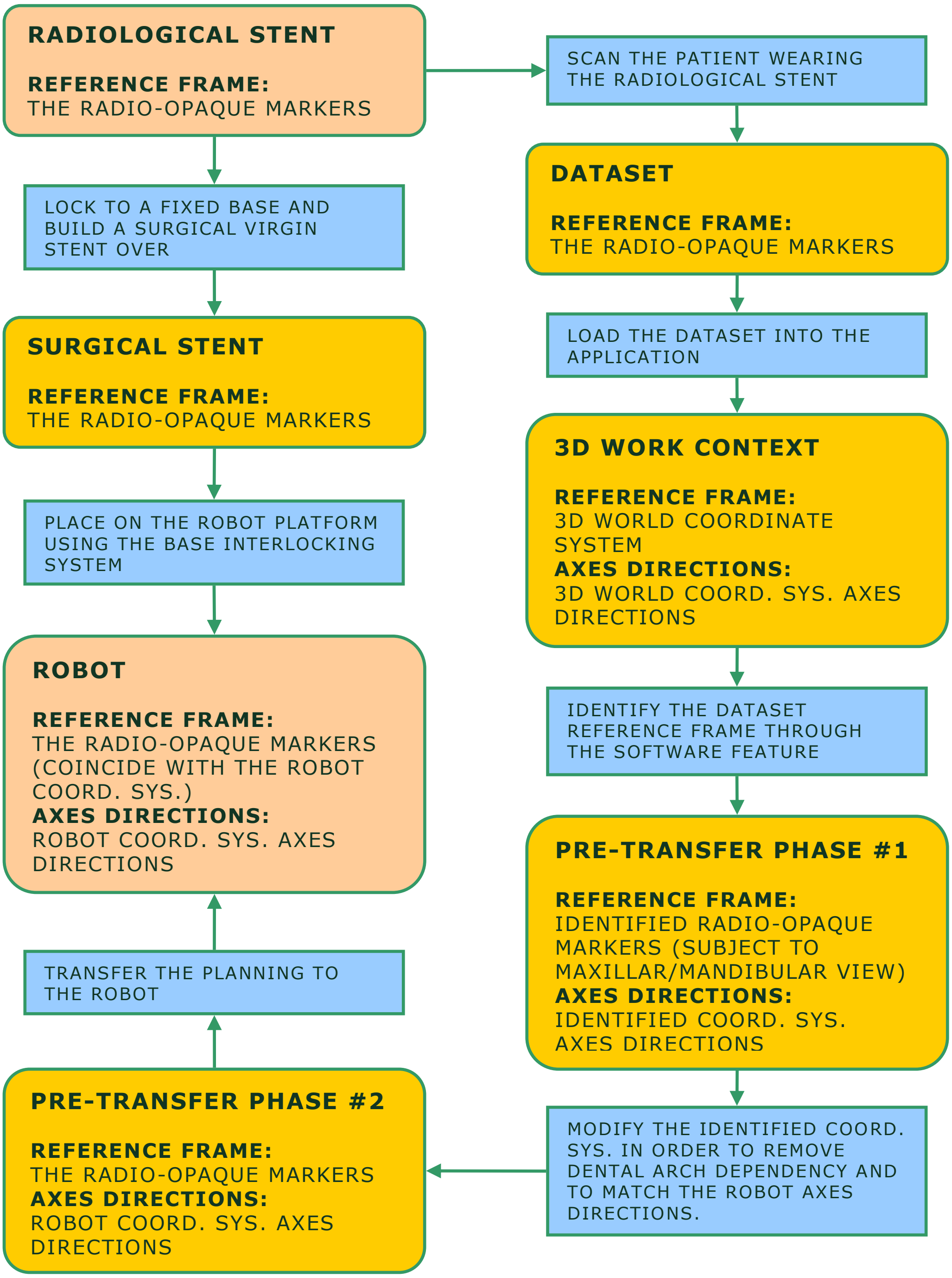

Fig. 6.7. *Change of the coordinate system*

6.3 PLANNING TRANSFER PRECISION

In order to evaluate correctness and precision of the implants planning transfer, and consequently to validate the last phase of the proposed approach, it has been digitally compared a multi-marker base and its planning transferred replica.

The first step of the adopted procedure has concerned the manufacturing and measurement of titanium reference markers in laboratory, each one of length 10 mm ± 0.03 mm (quoted uncertainty), under controlled conditions (20 °C ± 2 °C and 101325 Pa). Secondly, several markers have been installed in a plaster support, each one with a different orientation and for a different depth.

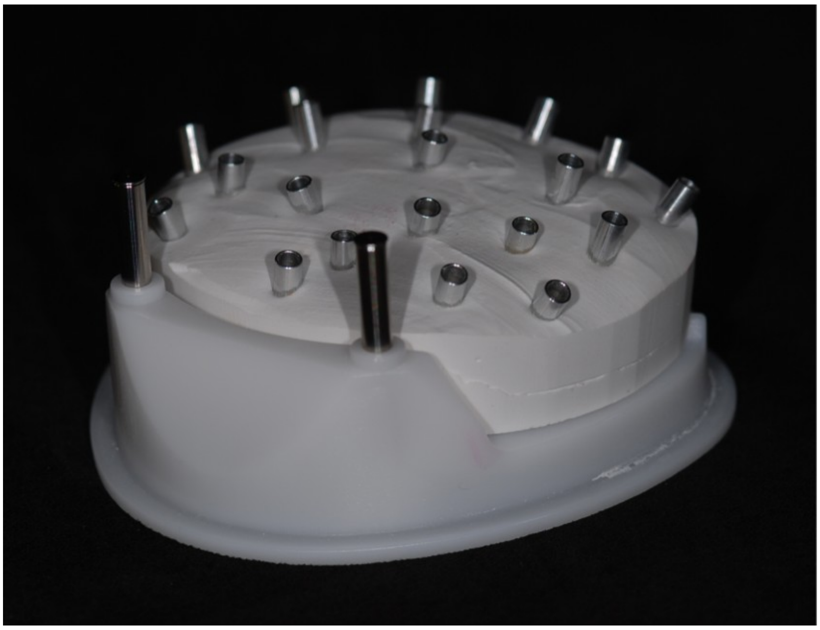

Fig. 6.8. *The first multi-marker base*

Then, the plaster block has been fixed on a plastic base (see Fig. 6.8) equipped with a titanium reference frame (see Section 6.1), and scanned by a Cone Beam Computed Tomography (CBCT) CEFLA GROUP – MYRAY scanner set with the following parameters: 90 kV; 6.5 mA; image reconstruction matrix of 512x512 pixel; 0.2268 mm of pixel thickness. The achieved dataset is composed by 209 slices, and it is characterized by both an Interslice value and a Pixel size of 0.2268 mm, thus no anisotropy nor interpolation errors are involved (Chiarelli et al. 2010b). At this point, after having imported and loaded the achieved data in the presented software, it has been accomplished the proper planning. 9 radio-opaque cylinders in the dataset have been selected, choosing the most diverse pool of orientations and depths, and suitable cylindrical CAD models have been overlapped onto each one, trying to match them as best as possible on the related best cross-sectional plane (see Chapter 4). To these purpose it has been used the generic implant builder feature of the software to shape hollow cylinders of proper dimensions, taking advantage of the positional constraints derived from the inner and outer markers radiuses. At the end of the planning, it has been used the software-robot interfacing feature (see Section 6.2) to transfer the planned implants into another plaster support fixed on the same kind of base as the first one (see Fig. 6.9).

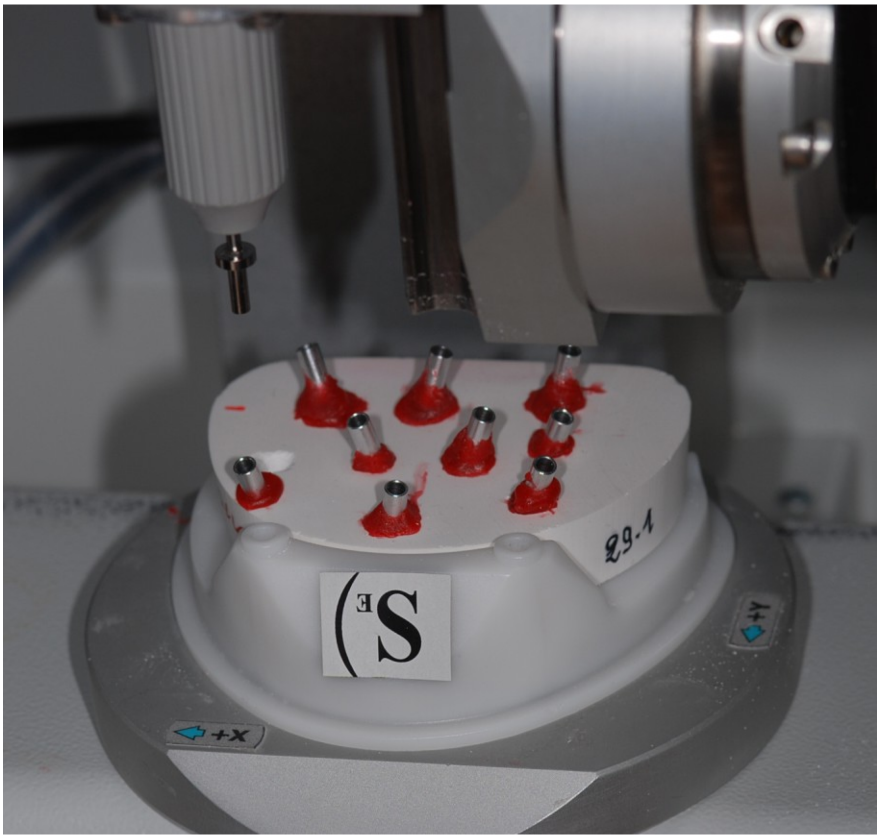

Fig. 6.9. *The obtained replica*

Once inserted the hollow titanium cylinders, the new multi-marker base has been scanned as well. Also in this case, after having imported and loaded it in the software, it has been accomplished the proper planning, following the previously described overlapping procedure. Using the planning transfer feature, it is possible visualize the data transferred from the software to the robot for each exported implant. Consequently, it has been feasible to evaluate the correctness of the transfer comparing the overlapping models parameters passed. In

Table 6.1-6.3 we report the resulting data. The shown values are respectively the identified markers centers distances in mm in relation to the robot reference zero (see Table 6.1), the identified markers orientations as slope angles around the robot reference frame X and Y axes (see Table 6.2), and the detected discrepancies (see Table 6.3).

TABLE 6.1. COMPARISON OF MARKERS POSITIONS

Markers	1st multi-marker base: positions			2nd multi-marker base: positions		
#	*x / mm*	*y / mm*	*z / mm*	*x / mm*	*y / mm*	*z / mm*
1	-43.2321	-14.9494	14.3952	-43.0959	-14.7379	14.3432
2	-19.9185	-8.5574	16.0543	-19.8157	-8.3345	16.0505
3	5.5280	-15.2188	16.3541	5.5264	-14.9999	16.3493
4	-43.0173	-32.7633	14.9035	-42.8115	-32.5903	14.8960
5	-30.8868	-26.7070	12.0022	-30.8670	-26.4583	11.9464
6	-11.3118	-25.2999	12.7169	-11.3544	-25.1291	12.6762
7	-41.7967	-46.2773	10.4191	-41.5988	-46.0256	10.2329
8	-20.1998	-43.5107	10.3369	-20.0484	-43.1966	10.1893
9	0.7690	-43.6163	10.0102	0.5720	-43.3699	9.8148

TABLE 6.2. COMPARISON OF MARKERS ORIENTATIONS

Markers	1st multi-marker base: orientations		2nd multi-marker base: orientations	
#	*tilt*	*turn*	*tilt*	*turn*
1	18.5977°	24.2108°	20.5323°	23.5591°
2	12.5797°	13.0757°	14.5504°	12.9952°
3	22.1745°	-9.7267°	22.8370°	-9.7011°
4	6.7243°	19.0803°	8.1689°	18.1879°
5	13.9272°	20.5047°	15.7667°	19.0975°
6	18.1886°	-8.1716°	20.0514°	-8.8158°
7	-1.4850°	16.8268°	-0.3331°	15.9823°
8	-2.2369°	14.7691°	-1.8041°	12.8755°
9	-4.5935°	-15.6226°	-3.9895°	-17.6872°

TABLE 6.3. MARKERS POSITION AND ORIENTATION ERRORS

Markers	Positions transfer errors			Orientations transfer errors	
#	*x / mm*	*y / mm*	*z / mm*	*tilt*	*turn*
1	0.1362	0.2115	-0.0519	1.9346°	-0.6516°
2	0.1028	0.2230	-0.0038	1.9707°	-0.0805°
3	-0.0016	0.2189	-0.0049	0.6626°	0.0256°
4	0.2059	0.1731	-0.0075	1.4446°	-0.8924°
5	0.0198	0.2487	-0.0558	1.8395°	-1.4072°
6	-0.0426	0.1708	-0.0407	1.8628°	-0.6442°
7	0.1979	0.2518	-0.1862	1.1519°	-0.8444°
8	0.1514	0.3141	-0.1476	0.4328°	-1.8936°
9	-0.1970	0.2463	-0.1954	0.6040°	-2.0646°

It results that the average position error along a single axis is about 0.072 mm, with about 0.314 mm as maximum absolute discrepancy and about 0.002 mm as minimum one, whereas the average position error (distance from the expected position) is about 0.283 mm in general. Concerning the orientation, instead, it results that the average angle error around a single axis is about 0.192°, with about 2.065° as maximum absolute discrepancy and about 0.026° as minimum one, whereas the average angle error (slope angle from the expected orientation) is about 1.798° in general. Notice that the reported results include the contributes of any positioning human and off-axis robot errors. Concerning original-replica discrepancy evaluation, the obtained results are significantly better than the ones achieved in similar studies based on stereolithography, in relation to the values reported by Di Giovanni et al. (2005), in which the best maximum error got was 1.1 mm (Klein & Abrams 2001; Van Steemberghe et al. 2002; Sarment et al. 2003a; Sarment et al. 2003b, Tardieu et al. 2003).

Also regarding the study involving both the evaluations (translation discrepancy and slope difference) accomplished by Di Giovanni et al. (2005), the precision achieved outperforms the stereolithographic approach one, whereas the average of the distance between the planned implant and the produced replica was 1.45 mm ± 1.42 mm at implant platform level and 2.99 mm ± 1.77 mm at apex level, with an axes difference angle of 7.25° ± 2.67° of standard deviation. In addition, it has to be noticed that the overlapping procedure has been accomplished on CBCT images, therefore better results are expectable on common CT ones, due to their sensibly higher image quality and resolution.

CHAPTER 7: RELATED WORK

In regard of the development of the solutions and features described in this dissertation, it has been necessary to study and review the related state of the art, both concerning the solutions adopted by existing planning software in relation to the common problems and lacks described (see Section 1.3), as well as the most recent and innovative techniques focused to mandibular canal recognition and tubular structures segmentation.

Many planning software tools are nowadays available, and, starting from CT images, they can provide an ad-hoc-built 3D visualization, and a multi-view one based on a series of images, namely *axial*, *panorex* and *cross-sectional* images. Among them, it is worth mentioning the pioneering software system DentaScan (GE Medical Systems), and SIM/Plant by Columbia Scientific (now property of Materialise). As previously reported (see Section 1.3), often the typical approach views are misleading or measurement error prone. Other software systems also provide a 3D representation which can be used for producing a solid model to guide the operative surgical phase (e.g., SurgiCase® by Materialise and CAD Implant by Praxim™). However, when re-orienting is considered (as, for instance, in SurgiCase), it is done according to a user-defined direction which is prone to mistakes too, also because they do not consider any reference marker. To the best of the knowledge acquired, apart from DentalVox

(Cucchiara et al. 2001), none of the mentioned systems consider the possibility of determining the direction of the planned implant (i.e., the best cross-sectional plane) by exploiting radio-opaque markers as it has been reported in this dissertation, and therefore re-orienting accordingly the 3D volume in order to have correct measures.

With the purpose of understanding the common problems in this kind of applications, and consequently of being able to define objectives to research solutions for (in order to develop a reliable planning tool), the state of the art in commerce and related approaches proposed in literature have been reviewed (see Section 7.1).

Similarly, regarding the mandibular canal segmentation and recognition, different related approaches have been studied and evaluated, in order to know better the state of the art, acquiring a wider knowledge on its panorama (see Section 7.2).

7.1 PREOPERATIVE PLANNING SOFTWARE

A pioneer work to move towards a 3D environment which well represent the real anatomy of the bone structure is described by Verstreken et al. (1998). The whole planning system described can be summarized as “one object, multiple views”, meaning that each object will consistently have the same aspect in all windows. In this work, the 2D multi-view and 3D environment are better integrated, but implant planning is still done in the 2D multi-view environment, and still prone to influence quantities discussed by Cucchiara et al. (2001). Furthermore, Verstreken et al. also propose a double scanning procedure, in order to evaluate esthetics results, besides design criteria. This is possible when the patient already wear a removable prosthesis which in many cases reflects optimal tooth positions. Then, a second scan of this prosthesis is used to obtain its structure. The two scans are then aligned by attaching small radio-opaque markers to the prosthesis, but the markers are exploited to that purpose only. Experimentation of the approach described by Verstreken et al. for CBCT images and comparison between the 2D CT and this approach, and the Procera system implementing it (Verstreken et al. 1996), are respectively described by Van Assche et al. (2007) and Jacobs et al. (1999). Van Assche et al. (2007) conclude that CBCT images could be used for implant planning, taking into account a maximal 4° angular and 2.4 mm linear deviation at the apical tip, while Jacobs et al. (1999) show a certain accordance (about 34%) in predictability between the two approaches, but a better pre-operative assessment of implant size by the 3D one.

Cucchiara et al. (2001; 2004) proposed to re-orient the original CT dataset according to a computed, relevant direction, usually equal to the axis of a radio-opaque marker inserted in a radiological mask worn by the patient during the CT scan. This approach, implemented in the DentalVox software tool (Cucchiara et al. 2001), leads to correct measures, and achieves a measurements precision that outperforms usual DentaScan approaches one, as discussed by Cucchiara et al. (2004). In addition, the described software is able to manage anisotropy in some cases of study, achieving a more precise and correct work environment as a result. This approach, however, is still multi-view: even if a 3D rendered model of the bone structure can be presented to the user, implant planning is done in a 2D multi-view environment, that includes the misleading panoramic view too. Moreover, the CT dataset re-orienting operation is not dynamically performable, but needs to reload the whole work context. Finally, the anisotropy correction algorithm applies one pass of interpolation only (see Chapter 3), consequently being not able to handle datasets characterized by an interlslice value not multiple of the related pixel size one, although this is a significant improvement in comparison to the majority of the software in commerce nonetheless.

A quite recent software able to provide a 3D representation of the volume, giving the user the possibility to produce a mask to guide the surgical operation is described by Kasumoto et al. (2006). The developed application starts from a stereolithographic file (achieved by the radiographic volume through a third-party software), and mix knowledge of computer graphic and mesh morphing to visualize the 3D model, and to make possible to modify it through the use of a virtual drill connected to a haptic device, giving the user a force feedback in relation to the kind of the surface drilled. Then, the software allows the user to insert implant-simulating cylindrical models in the 3D structure, and to create the stereolithographic file to produce the surgical mask through rapid prototyping. Obviously, the aim of what is described by Kasumoto et al. is mainly focused on the physical simulation of implants insertion to train inexperienced dentists, and only secondarily to be a tool to guide the surgeon during the operation. Actually, it differs from the work proposed in this dissertation starting from the beginning of the approach, since it leaves the three-dimensional reconstruction to a third-party software to achieve the bone model. However, the most obvious difference concerns the reliability and the tools required to accomplish a correct and effectively usable pre-operation planning: in the approach of Kasumoto et al. the simulation part is merely based on the three-dimensional representation of the bone structure, without any radiographic reference (to achieve the correct information needed to the surgeon to work in safety). Then, the mask created through rapid prototyping from a stereolithographic file has thought to be supported directly by the bone, forcing the surgical operation to the consequent invasiveness to ensure the stability for the milled template.

A complete approach to implant planning and positioning, similar to the one presented in this dissertation, is the Med 3D implantology one (implant3D and X1med3D). The process flow starts with the scan of the patient wearing a template of the prosthetics wax-up in which has been inserted a registration brick marker. Then the data is transferred to a CD-ROM to be read by the provided planning software. After the planning, a surgical mask with titanium guides, correspondent to the planned implants, is produced though the use of a positioning device.

Finally, the achieved template is used in the surgical phase. While the overall approach resembles the one described in Section 2.1, there are several differences within. The first thought is about the choice to include the prosthetics in the scan: it is a good way to evaluate aesthetics results in the 3D view, but just if it has been also implemented the possibility to hide, when necessary, the prosthetics structure. Another difference is the decision to avoid an internal database to store the cases of study: where this is a good way to save hard disk space, decreasing system requirements consequently, it reduces usability, forcing the user to have every CD-ROM immediately available and to load data with the speed of an optical device. Med 3D claims as an advantage that their data are loaded without any central processing, so directly the axial slices from the CD-ROM, but, on the contrary, this does not guarantee to operate upon an isotropic voxel, and therefore the whole system can be subject to significant errors concerning measurement and proportions. Furthermore, the multi-planar views, even if connected each other for real-time changes, seem to follow the common DentaScan methodology, providing a 2D context of work, plus an ad hoc 3D one, characterized by the usual cross-sectional reconstruction. Thus, as already discussed, the system carries on a significant error in measurements due to the slope angle between the cut plane and the tooth axis of interest.

Another approach of the same kind is the one proposed by IVS Solutions AG regarding coDiagnostiX® (and gonyX®). Apart from the several protocol requirements needed to get everything works properly, the process flow it is quite similar to the one described immediately before. It starts from the fabrication of a prosthetics appliance, which is worn by the patient during the CT scan afterwards. Then, it uses the provided software to load the data and plan the most suitable implant positions. Finally, a surgical mask is drilled by a mechanical device accordingly with the implants axes and the produced template is used during the operation. In addition to the prosthesis scan, allowing to estimate the esthetics results during the planning, there are useful features included in the proposed software, from mandibular nerve canal drawing to several implants functionalities. However, the first most significant lack is, again, the absence of the reconstruction of the whole dataset under isotropic conditions, implying the incorrectness of measurements achieved along the axis normal to the axial plane. Then, the decision to keep the multi-view DentaScan interface, forcing the user to pass through both the drawing of the panoramic curve and the implants raw positioning in the common incorrect cross-sectional planes. By the way, although through a 2D context of work, using the 3D one just to visualize the planning, this approach shows to have understood the incorrectness of the common cross-sectionals. To face it, it provides the possibility to align a plane, called Tangential View, to an implant axis, letting to achieve correct measurement regarding the implant. On the other hand, this process forces the user to use a 3D object to determine the correct slope angle, instead of defining a simple line in the axial view as proposed in this dissertation. The advantage of the cross-sectional reconstruction presented in Chapter 4, moreover, is the freedom to cut the radiographic volume arbitrarily, and not just in relation to the implants.

Materialise's SimPlant® is another software for pre-operative planning for oral implantology. It is the main part of an already seen approach that concerns the CT scanning of a patient wearing a prosthetics template, the planning of implants positions on the provided software, and the creation and use of an ad-hoc-built surgical mask where titanium guides have been installed. As well as a double scanning procedure for prosthesis structure evaluation, the software provides also several useful functionalities, like nerve identification, virtual teeth creation, and collision detection. Moreover, there's a feature to align axial planes to the occlusal one too. However, again, the first big lack is the choice to work on the original dataset, without managing the possible, and quite probable, anisotropy of the volume. This, as already said, may lead to significant errors concerning measurements and proportions. Another difference with the system presented in this dissertation is about the interface: although the software has the merit to provide an integrated 3D work context, it carries on the obsolete DentaScan multi-planar view, consequently including panoramic and cross-sectional views. As explained, measures achieved on these views are incorrect, due to the distortion of the panoramic view and the slope angle between the tooth axis of interest and the cross-sectional cut plane. Aware of this problem, although letting the possibility to work on the incorrect views, the software offers a functionality to visualize a view centered on the implant, parallelly to its height axis. As previously seen, this procedure forces the user to update continually the view to fit the implant orientation, instead of having the option to define the desired axis and plane, as proposed in Chapter 4.

7.2 MANDIBULAR NERVE CANAL RECOGNITION

A powerful approach developed in regard of medical images segmentation is described by McInerney & Terzopoulos (2000). They presented a new class of deformable contours (called snakes) defined in terms of an Affine Cell Image Decomposition framework (ACID), calling the developed model T-snakes. Their approach extends conventional snakes, enabling, among other features, topological flexibility (thus, the name of topology adaptive snakes, or T-snakes). The algorithm is based mainly on the combination of two parts. One of them is about the application of a parametric snake on the image, needing to start from a seed point, but being quite robust to not get negatively influenced by its position (till obviously it relies in the proximity of the area to be segmented). The second part consists of decomposing the image space in affine cells (e.g., the Marching Cubes method described in Section 2.2.2), and applying iterative snake reparameterization in order to allow it to adapt to a possibly changed topology. This last operation starts with a deformation step, involving external and internal forces computing and consequently snake nodes updating, that is repeated a user-defined number of times. Thus, the snake silhouette will change, tending towards the image grid cell edges. Then two other reparameterization phases follow. In the first one the T-snake elements are intersected with the grid cell edges, and the achieved intersection points of which may become the snake future nodes. The second phase, instead, aims at redefining snake correspondent edge cells, as well as its interior ones in order to know at any time the inner region. Then, the T-snake elements are updated in relation to the grid boundary cells. Finally, McInerney & Terzopoulos also provided an algorithm version for three-dimensional segmentation (called T-surfaces), thus operating on a 3D dataset, that, in regard of the mandibular canal identification, could be exploited in order to avoid the otherwise needed multiple seed points (one for each slice). However, whereas this approach has great segmentation potential, it results not the optimum in regard of mandibular canal identification. In fact, it could not work correctly in mandible interior environment, independently from the complexity of the shapes it is able to recognise. Problems such greyscale-intensity similarity between canal inside and outside, conduct holes and interruptions, inconstant canal soft tissues density, low contrast and common artefacts, are significant obstacles to its efficacy. In order to manage these kind of situations, the authors provided the possibility to manually customise the snake inserting some types of constraints (the intuitive interaction feature is one of the described goals). However, its relevant dependence from a proper user interaction is not a desirable trait in an oral implantology planning software, at least in the extent that would be needed in regard of the mandibular canal segmentation.

In relation to segmentation of jaw tissues, and consequently in regard of highlighting and identifying the different mandible regions, among which the mandibular canal, Lloréns et al. (2009) presented an interesting approach very recently. Fundamentally they propose the application of Fuzzy Connectedness (FC) theory in support of an ideal automatic and time-efficient jaw segmentation algorithm (the automation of which is subject to future work). The application of the fuzzy technique on images, described by Udupa & Samarasekera (1996), allows to achieve, starting from a seed and analyzing every pixel of the image through a growing filter, a connectivity map that defines the affinity between each pixel and the seed. The authors propose to exploit FC on each CT image of a dataset, given proper starting points and parameters, in order to identify connected regions, and consequently to segment them. About the mandibular canal, this methodology can be accomplished using some testing-determined best FC parameters to get the connectivity map, and applying a default threshold on it. Then, the application of a holes-filling algorithm on the segmented region is needed, aiming at uniforming the mandibular canal area. Notice that the requested seed point is selected by the user on CT slices, and some FC parameters are achieved locally in the neighbourhood of the seed point. Whereas the described FC parameters local definition seems based on the same logic of the threshold range one presented in this paper, the proposed approach looses a significant part of its desirable automatism due to the need of intense interaction of the user. Actually, Lloréns et al. prospected the algorithm automatism for another jaw's area only (i.e., the cortical bone). However, even if the planning doctor did not need to identify a canal seed point for each CT dataset slice, hypothesizing that the authors will develop an automatism for the mandibular canal segmentation too, it would follow an analysis of the whole 3D reconstructed dataset nonetheless, ignoring the mandibular conduct shape a priori. This means that, in relation of the timings reported (7 seconds of processing per slice on MATLAB), it could result excessive concerning real-time planning software interactivity requirements (unless drastically optimized on purpose). Moreover, the authors seem not to have taken in consideration the real, unpredictable, and absolutely not continuous nature of the mandibular canal, ignoring to describe the result of the FC growing filter in correspondence of holes and canal interruption, that actually is the most critical point of its recognition. However, fuzzy connectedness as segmentation methodology on CT images, that they validated, remains an interesting path to be explored nonetheless.

As already reported in Section 5.2, Yau et al. (2008) presented an immediate and user friendly methodology to segment the mandibular nerve canal. Their algorithm is based on the common Dentascan multi-view context, and on cross-sectional views scrolling along the panoramic curve in particular. Starting from an user-defined seed point, and finishing in correspondence of second one, the presented approach provides the analysis of each scrolled slice in order to extract the inferior alveolar nerve region. In particular, it consists of successive applications of a statistical segmentation and a region growing filter around a seed point, and the intersection with an expected nerve region in the following slice to find the seed point on it (see in detail in Section 5.2). In this way the algorithm is able to identify the conduct path, as well as its thickness according to the regions recognised during the advance. Whereas this approach is very interesting for intuitiveness and low-interaction needing, it is not robust enough to excellently trace mandibular canals. Indeed, holes, bifurcations, and significant canal interruptions, typical of these tubular structures, strongly affect the proposed algorithm, possibly leading to leakages.

Another approach able to semi-automatically identify mandibular structures in CT, as the mandibular canal and the dental nerve, is the one reported by Rueda et al. (2006). This algorithm mainly consists of an automatic segmentation of soft tissues and a semi-automatic landmarking process, in order to produce an Active Appearance Model (AAM). In particular, whereas the Active Shape Model (ASM), a template matching technique, adapt the shape of the object to be segmented according to the statistical information of a training set previously annotated by an expert, the AAM, that is an ASM extension, also takes into account texture and shape variability. The reported approach aims at improving the state-of-the-art of template matching algorithms, although it keeps a disadvantage in its need of an intensive model training, as well as in the necessity of a semi-automatic landmarking, in order to increase the system precision. In addition, the results reported (i.e. a mean error of 4.76 mm for the mandibular canal) are clearly in conflict with the precision needed by proper oral implantology planning software, highlighting a significant deficiency in this kind of techniques.

A quite recent approach to tubular surfaces extraction, that does not need the application of templates and algorithm training, is described by Li & Yezzi (2007). The proposed methodology combines minimal path and active surfaces techniques in order to extract both vessels 3D surface and their centerline, allowing to represent the full 3D tubular model rather than a curve within its interior simply (a limit of minimal path techniques only application). The idea behind their approach is to model a tubular surface as a 4D curve, subtended by two user-defined endpoints, that is determined by three spatial coordinates (the curve points) plus a fourth one which described the thickness (radius) of the vessel. Thus, each 4D point (including the user-defined ones) represents a sphere in the 3D space, and the vessel model is achieved enveloping the sphere along the identified curve. The tubular surface centerline, if needed, is consequently achievable by the spheres centers. The proposed algorithm is surely a good innovation toward pseudo-constant-grey-intensity tubular surfaces recognition, like the vessels one, but it carries on some disadvantages when applied outside that context. First of all, the algorithm is thought to work on fairly intensity constant shapes, such as vessels and colons in medical imaging. To this regard, the authors provide also an alternative way to calculate the sphere inner region potential (the value used to determine the 4D curve evolution), that allows to take in consideration the tubular edges only, avoiding the inner differences of greyscale intensity. However, not only the mandibular canal is not grey-intensity-constant at all, but, as reported in Section 5.3, neither its edges continuity is predictable, involving surface holes as well as its complete merging with the rest of the mandible. Moreover, the proposed methodology needs the interaction of the user not only concerning the starting and final points definition, but also in regard of setting, for each tubular recognition, the most proper algorithm parameters, among which the sphere potential formula and the initial spheres radii, that significantly affect the final result effectiveness. Naturally, this is in conflict with the aim of easing and speeding up the user operations in a planning software system (as defined in Section 1.3.4), and consequently a reason for which this approach has been discarded. Furthermore, Li and Yezzi claim that the developed algorithm is able to achieve the needed reconstruction on noisy and low contrast images, but actually the level of noise and neighbourhood complexity of a mandible interior is not comparable with the one of vessels, that are quite more neatly defined compared to the inferior alveolar nerve canal. This emerged also talking directly with Prof. Yezzi about possible applications of active contour models in the mandibular region. Finally, exploiting a similar methodology, the authors presented also an approach able to recognise multi-branch vessels, instead of single branch ones, and that needs one user-defined point (sphere) instead of two (Li et al. 2009). Whereas its application on the mandibular canal could be interesting to identify the branches of the inferior alveolar nerve, as the mental one, it keeps the disadvantages previously described.

Another algorithm of tubular segmentation based on 4D-curve-exploiting is explained by Mohan et al. (2010), and it focuses mainly on brain fiber bundles and cardiac blood vessels recognition. The proposed approach, that aims at tubular anatomical structure extraction, works similarly to the one presented by Li & Yezzi (2007), which the authors declare to having been inspired by. In relation of the techniques involved, it differs mainly in regard of energies calculation (a class of functionals that define the region segmentation): the authors cannot optimize them using the minimal path technique, as Li & Yezzi did, because their energies are directional dependent, being related to the position of the 4D curve and its tangent. In addition, their region based segmentation uses local statistics, rather than statistics related to the whole structure, as traditionally performed in these methodologies. The clear advantages of the presented approach are the need of one user-defined seed point only (the starting one) and the characteristic to adapt to greyscale intensity inconstancy along the tubular conduct regions. Moreover, similarly to the evolved approach presented by Li et al. (2009), the algorithm proposed by Mohan et al. is able to identify, during the 4D curve definition, departing branches and consequently to evolve along their direction, being able to achieve tubular trees recognition instead of a single branch structure only. However, even if this approach has the important improving to not need intensive user interaction, it presents several of the mandibular canal structure and artefact sensitivity problems described in the previous related work review.

Also Benmansour & Cohen (2010) have been inspired by Li & Yezzi (2007) in regard of vessels segmentation and tubular surface extraction. They proposed a similar approach based on a variant of the minimal path method that models a vessel as a 4D curve (centerline plus local radii), whereas the most relevant step is in the local metrics to minimize. In particular, the authors have built an anisotropic potential (based on a technique called Optimally Oriented Flux), that is well oriented along the vessel direction and provides a good estimate of its radius, while marching fast along the centerline. The main advantages of the developed algorithm are about its robustness to leakage, as well as to its initialization. Indeed, the algorithm need at least two endpoints to start with (or more if the intention is to identify more than one branch), but its quite insensitive to their location, provided they are within the conduct lumen (the disk section of the vessel). Moreover, the presented algorithm demonstrated to be successful also in presence of low noise, and adaptive to conduct scale variations. However, regardless of these good points, the approach remains bonded to vessels characteristics of smoothness, continuity and uniformity, that recognition of which is actually its primary aim, consequently having potential difficulty in presence of image low contrast, inner and outer shared densities, interruptions, and significant deformations (as happened in cases of non circular or occlused lumen reported the authors).

CHAPTER 8: DISCUSSION

The dissertation ends with conclusions about the research accomplished, hypothesized future works, and right and proper acknowledgments.

8.1 CONCLUSIONS

In this dissertation, it has been presented a complete and fully 3D approach for oral implantology planning, aiming at improving the state of the art through management and correction of related common mistakes. Firstly, the most significant lacks of planning software systems in general have been defined (misleading work context views, unhandled volume anisotropy, incorrectly reconstructed cut planes, lack of relevant anatomies automatic identification). Then, they have been contextualized for the oral implantology medical field, and many literature approaches have been analysed to determine the way to undertake. Subsequently, solutions have been developed and implemented, producing an application in which implant planning and simulation can be done in a isotropic 3D environment, taking advantage of computer graphics techniques. A correct and realistic view of the bone anatomy is achieved, and besides correct measures, also correct orientations of the planned implants is easily computed and transferred to the surgical act. The whole approach requires that during the CT scan, the patient wears a radiological stent with radio-opaque markers, among which two are used as reference frame, to have relevant axes in the 3D space and an anatomy related coordinate system. Then, after exploiting the software, the planning data can be correctly transferred, through proper coordinate system change, into a surgical stent drilled by a bur equipped 5-axes anthropomorphic arm interfaced to the application.

Regarding the framework, it has been developed a multi-view work environment that discards the misleading panoramic view in favour of a wider sight on the planning-fundamental cross-sectional ones, and that fully integrates the 3D view into. The work context actually is a 3D virtual world watched through different filtering-lens-equipped cameras, that allows the user to plan in every view, being able to observe the modifications in real time in each other view. The views filters, achieved using ad-hoc rendering techniques, allow to visualize the scene emphasizing diverse aspects, as the radiographic for detailed positioning or the fully three-dimensional to analyse the planning as a whole together with the bone structure. The built-in graphic engine, developed on purpose, is powered by a quaternion library developed from scratch, that, additionally, allows a correct trackball rotation for the 3D bone model, achieved exploiting the Marching Cubes isosurface extraction algorithm. The user interaction has been enhanced, implementing, among the others, a post-rendering picking system, as well as selection states and micrometre accuracy movements of objects. Furthermore, implant CAD and generic models loading have been supported, in order to allow to accomplish the best planning in accordance with the needs of the doctor. This has been also possible because of the developed mesh manager, that, exploiting video memory and graphics, handle intense use of three-dimensional objects, keeping good performances. Finally, several tools and features with the aim of completing and improving the planning, like measurement tools, a contrast/brightness modifier, and an useful axes storing system.

The anisotropy problem has been correctly handled through the development of a 2 Pass Interpolation algorithm, that is able to properly subdivide the 3D dataset whereas necessary, achieving an isotropic volume as a result. The algorithm consists of two main steps: in the first one it uniformly fills the interslice void spaces with the maximum integer number of pixel-size high slices, then it divides the previous result in a proper number of groups, and reconstructs a new group for each old one, with the needed number of pixel-size high slices, through interpolation. As a consequence, every CT dataset imported in the software will be correctly processed, obtaining an isotropic volume independently from the ratio between the DICOM interslice value and pixel dimension. Anisotropy correction has been validated calculating the measurement errors implied by the absence of anisotropy management, the application of 1 pass of interpolation, and the application of 2 passes of interpolation, for 40 markers distributed over 5 different cases of study (2 maxillas and 3 mandibles), and comparing the results. The proposed method totally outperformed the 1-pass-only one, with a mean error of 0.002 mm against 0.416 mm, that already outperformed the no-interpolation method in turn (mean error of 4.070 mm).

In relation to the incorrectness of common cross-sectional planes, it has been provided a run-time reconstruction feature able to dynamically redefine oblique planes through interpolation, in accordance with any axis the user chooses at any moment of the planning. In this way, the doctor is able to accomplish correct measurements on oblique planes, for any number of axes of interest, without the need of a CT scan necessarily characterized by a transaxial plane orthogonal to a particular tooth axis, nor multiple CT scans if more axes are needed. In addition, in order to support the custom reconstruction functionality, it has been provided the possibility to automatically obtain the tooth axis of interest. In particular, this feature helps the implantologist identifying the marker axes and avoiding any mistake due to the manual reconstruction process. Moreover, to complete the slice reconstruction tool, it has been extended the functionality allowing the user to choose at run-time to reconstruct the cross-sectional planes parallel to the height axis of the desired implant. In this way, it is possible, at any time, to know the surrounding area of the implant, providing the possibility to get fundamental distances between the borders of the implant and the rest of the environment. As successfully resulted from the evaluation, because of these group of functionalities the implantologist has dynamically at hand any desired area of interest during the planning, being able to achieve the correct measures he needs to operate in safety. Measurements precision has been validated by considering different scans of a dried human partially edentulous mandible, which was scanned several times, with different angular orientations. Measures achieved, and related errors, have been accomplished both on the presented system, exploiting the slice custom reconstruction functionality, and on a common Dentascan based one, and the results have been compared. Precision achieved (mean error of 0.038 mm) is resulted to be better then the DentalVox tool one, which already outperforms usual DentaScan multi-view approach in precision (Cucchiara et al. 2004). It has been also evaluated and validated both the effectiveness and the efficiency of the automatic marker identification feature, applying it on 69 markers distributed over 15 datasets as testing base, achieving a success rate of 93% excluding extreme noise cases, and 74% otherwise. Finally, it has been demonstrated the software compliancy about CTCT images. A survey about the cross-sectional slice reconstruction functionalities, with related testing results, have been reported in Chiarelli et al. (2010a).

As well as the others research objectives, also the automatic recognition of the mandibular nerve canal has been solved. This has been accomplished developing an algorithm based on the application of local statistical segmentation along successive slices properly defined. The algorithm, that requires low interaction, needing only two user-defined points (a starting and a final one), calculates at each progressing step the following seed point, and the direction of the related slice as a consequence. Robustness and effectiveness is assured by its division in two main parts. In the first one, the propagation front starts from the final point and proceeds for a limited path, identifying a checkpoint immediately at the bottom of the mental foramen ascent. The second part, instead, consists of applying the segmentation advance from the starting point, properly modifying the seed points generation in accordance with the checkpoint position. Finally, the achieved paths are merged. In this way it is possible to handle leaks due to canal surface holes, as well as to overcome the conduct disappearance in its final part, obtaining the inferior alveolar nerve canal centerline and thickness. Then, a tubular structure mesh builder, that has been implemented on purpose, is able to use the mandibular canal identifying seed points to reconstruct a 3D model of it, exploiting Catmull-Rom splines to smooth the model curve (adding further robustness against isolated errors). The quality of the recognition feature has been clinically validated by a renowned implantologist, who tested the functionality on both the mandibular canals in 7 CT datasets, achieving a successful rate of 13 cases, and confirming the efficiency of the presented canal automatic identification methodology. In 1 case the algorithm failed due to the complete hiding of the canal in its first part, due to an extreme scattering shadow effect, where the checkpoint attraction force is significantly weaker. In order to manage this kind of situations, it has been also implemented a canal manual drawing functionality, with the aim of allowing the user to accomplish the proper planning even in cases of extreme noise.

In addition, with the purpose of completing the defined global approach for oral implantology planning, it has been implemented the interfacing between the software and a robot able to drill properly the surgical stent. This has been achieved exploiting two outer radio-opaque markers in the radiological stent worn by the patient during the CT scan. These makers allows to have the same physical reference frame both in the 3D virtual world of the planning software, as in the working space of the drilling robot. Thus, before to transfer the planning data to the anthropomorphic robotized arm, the implant models needed parameter (position, orientation, and depth) are transformed in accordance with the user-identified reference frame in the radiographic volume. Then, a surgical stent is built on the same wax-up of the radiological one, that also shares the same plastic support, and is fixed to the robot platform exploiting the base interlocking system. In this way, the surgical mask reference frame will corresponds to the robot one, allowing a proper coordinate system sharing. Finally, the 5-axis robot drills the virgin stent reproducing the planning onto the surgical template. The dentist is then able to use the produced mask during the surgical act to guide the drilling and inserting operations, consequently implying greater precision with minimal invasiveness. Planning transfer precision has been validated comparing digitally a multi-marker base and its software-guided robot-drilled replica, and obtained results (mean discrepancy of 0.314

mm in position and 1.798° in angle) outperform the ones of similar studies in literature about stereolithography (Di Giovanni et al. 2005).

In conclusion, each of the four research objectives have been completed, contributing to develop a reliable and fully 3D approach for oral implantology, and an improved planning software system, in particular. As emerged from each evaluation accomplished, the proposed software overcomes the state of the art, providing solutions for the related lacks and flows, consequently allowing implantologists to plan upon a correct and precise work environment. Finally, the planning can be transferred directly into the surgical act exploiting a robot-drilled template, increasing the safeness and the precision of the operations, speeding up the surgical procedure, and decreasing the post-operative timings and patient's discomfort, thus contributing to improve the minimally invasive surgery. Notice that, at last, every solution adopted, from the framework to the anisotropy management, as well as the custom slice reconstruction, is completely and directly reusable for any other medical field. The only exceptions are the relevant anatomy recognition and the physical reference frame, as well as the design of the drilling robot, that should be re-contextualized in accordance with the new field (even if the mandibular canal recognition could be re-set for other relevant tubular structures with just few tweaks).

8.2 FUTURE WORK

Even if the main deficiencies identified in oral implantology planning software have been dealt with, there are surely other improvements that can be realized in order to significantly enhance the software support to the user. A brief survey of some of them follows:

- Mandibular canal detail improvement: with the purpose of increasing the recognised mandibular canal realism, it would need few tweaks on the reconstruction algorithm in order to achieve a tubular structure with varying diameter, improving the canal highlighting precision as a consequence. This feature could be obtained exploiting the previously segmented nerve regions for the automatic recognition, and through a custom diameter for each user-defined seed point in relation to the manual drawing.
- Maxillary sinus drawing: another relevant anatomy in oral implantology, that could be useful to highlight, aiming at easing the related planning, is the maxillary sinus (air-filled space that communicates with the nasal cavity, within the bones of the skull and the face). The possibility to draw this volume would help the implantologist to take it into consideration more easily during the planning, avoiding the risk to damage the superior alveolar nerve within, as well as arteries nearby.
- Collision detection: implementing a collision detection feature the software would be able to warn the user, in real-time, whenever implants planned would touch or be too much near to

other objects, like the mandibular canal or other implants as well, giving the possibility to correct the unseen problem.

- Computer aided markers centering: in order to further enhance the custom slice reconstruction functionality, it could be added a centering support feature. It would be feasible exploiting the Hough transform for circles recognition (used in the markers automatic identification), and applying it over a small region of interest whenever the user would want to spot a radio-opaque marker center (in order to identify its axis). In this way, the cursor could be magnetically-like guided toward the desired center, significantly increasing the precision of the manual operation.
- 3D bone model rendering and interoperability: other rendering techniques could be exploited with the aim of improving particular operations, or allowing new ones. For example, a Direct Volume Rendering technique could be used to enhance the complete 3D volume analysis (being able to show every tissues layer through different levels of transparency), or a volumetric 3D reconstruction (e.g., using a Marching Tetrahedron algorithm) as base for a mesh deformability feature (e.g., for maxillofacial surgery planning).
- CT/CBCT images enhancing: implementing automatic image processing enhancers, like sharpening, windowing, and closing algorithms, able to define the proper degree of application in relation to the dataset greyscale value statistics, could improve significantly effectiveness and efficiency of automatic

recognition features (as the mandibular canal recognition and the marker automatic identification).

- Extension to other medical fields: as previously mentioned, the software is easily transferable to other medical specialties, because the most of its framework and functionalities is basically adaptable to any radiology based diagnosis and surgical planning (e.g., maxillofacial or orthopaedic), as well as to implantology in general.

8.3 ACKNOWLEDGMENTS

I would like to thank everyone who made possible this research dissertation. Special thanks to Prof. Evelina Lamma and Eng. Tommaso Sansoni for their significant support to the development of the interactive application and the kindness shown, as well as to Drs Federico Franchini and Achille Lamma for their invaluable help, that includes necessary knowledge sharing, medical requirements and priorities definition, and testing and evaluation of the software. Finally, I would like to thank also my family, and my fiancée Svenja in particular, who contemporarily supported and borne me during the research doctorate and the writing of this dissertation.

REFERENCES

Barker, T. M., Earwaker, W. J. S. & Lisle, D. A. (1994) Accuracy of stereolithographic models for human anatomy. *Australasian Radiology* **38**: 106-111.

Benmansour, F. & Cohen, L. D. (2010) Tubular Structure Segmentation Based on Minimal Path Method and Anistropic Enhancement. *International Journal of Computer Vision* **92(2)**: 192-210.

Bianchi, S. D., Ramieri, G., De Gioanni, P. P., Martinetto, F. & Berrone, S. (1997) Validation of anatomical SLA replicas: personal experience and literature review. *Radiol Med* **94**: 501-510.

Bouyssié, J. F., Bouyssié S., Sharrock, P. & Duran, D. (1997) Stereolithographic models derived from X-ray computed tomography – Reproduction accuracy. *Surg Radiol Anat* **19(3)**: 193-199.

Canny J. (1996) A computational approach to edge detection. *IEEE Trans Pattern Anal Machine Intell* **8(6)**:679–97.

Chiarelli, T., Franchini, F., Lamma, A., Lamma, E. & Sansoni, T. (2009a) A 3D environment for oral implant planning and simulation. *International Journal of Computer Assisted Radiology and Surgery* **4(S1)**: S217-S219.

Chiarelli, T., Lamma, E. & Sansoni, T. (2009b) A Tool to Achieve Correct and Precise Measurements for Oral Implant Planning and Simulation. In: IEEE, ed. 2009 IEEE International Workshop on Medical Measurements and Applications Proceedings, pp. 246-251.

Chiarelli, T., Lamma, E. & Sansoni, T. (2010a) A fully 3D work context for oral implant planning and simulation. *International Journal of Computer Assisted Radiology and Surgery* **5(1)**: 57-67.

Chiarelli, T., Lamma, E. & Sansoni, T. (2010b) Techniques to Improve Preoperative Planning Precision for Oral Implantology. *IEEE Transactions on Instrumentation and Measurement* **59(11)**: 2887-2897.

Choi, J. Y., Choi, J. H., Kim, N. K., Lee, J. K., Kim, M. K., Lee, J. H. & Kim, M. J. (2002) Analisys of errors in medical rapid prototyping models. *Int J Oral Maxillofac Surg* **31**: 23-32.

Cucchiara, R., Franchini, F., Lamma, A., Lamma, E., Sansoni, T. & Sarti, E. (2001) Enhancing Implant Surgery Planning via Computerized Image Processing. *International Journal of Computerized Dentistry* **4(1)**: 9-24.

Cucchiara, R., Lamma, E. & Sansoni, T. (2004) An image analysis approach for automatically re-orienteering CT images for dental implants. *Computerized Medical Imaging and Graphics* **28(4)**: 185-201.

Di Giacomo, G. A., Cury, P. R., de Araujo, N. S., Sendyk, W. R. & Sendyk, C. L. (2005) Clinical Application of Stereolithographic Surgical Guides for Implant Placement: Preliminary Results. *Journal of Periodontology* **76(4)**: 503-507.

Duncan, J. S. & Ayache, N.(2000) Medical Image Analysis: Progress over Two Decades and the Challenger Ahead. *IEEE Transaction On Pattern Analysis and Machine Intelligence* **22(1)**: 85-106.

Gouraud, H. (1971) Continuous shading of curved surfaces. *IEEE Transactions on Computers* **C-20(6)**: 623–629.

Hughes, N. H. (unpublished) Euler Angle Conversion for Arbitrary Rotation Sequence Using Geometric Methods. *Braxton Technologies*.

Illingworth J. & Kittler, J. (1988) A survey of the Hough transform. *Computer Vision, Graphics, and Image Processing* **44(1)**:87-116.

Jacobs, R., Adriansens, A., Verstreken, K., Suetens, P. & van Steenberghe, D. (1999) Predictability of a three-dimensional planning system for oral implant surgery. *Dentomaxillofacial Radiology* **28(2)**: 105-111.

Klein, H. M., Schneider, W., Alzen, G., Voy, E. D. & Gunther, R. W. (1992) Pediatric craniofacial surgery: comparison of milling and stereolithography for 3-D model manufacturing. *Pediatr Radiol* **22**: 458-460.

Klein, M. & Abrams, M. (2001) Computer-guided surgery utilizing a computer-milled surgical template. *Pract Proced Aesthet Dent* **13(2)**:165-169.

Kragskow, J., Sindet-Pedersen, S., Gyldensted, C. & Jensen, K. L. (1996) A comparison of three-dimensional computed CT scans and SLA models for evaluation of craniofacial anomalies. *J Oral Maxillofac Surg* **54**: 402-411.

Kusumoto, N., Sohmura, T., Yamada, S., Wakabayashi, K., Nakamura, T. & Yatani, H. (2006) Application of virtual reality force feedback haptic device for oral implant surgery. *Clinical Oral Implants Research* **17(6)**: 708-713.

Lill, W., Solar, P., Ulm, C., Watzec., G., Blahout, R. & Matejka, M. (1992) Reproducibility of 3D CT-assisted model production in the maxillofacial area. *Br J Oral Maxillofac Surg* **30**: 233-236.

Li, H. & Yezzi, A. (2007) Vessels as 4-D Curves: Global Minimal 4-D Paths to Extract 3-D Tubular Surfaces and Centerlines. *IEEE Transactions on Medical Imaging* **26(9)**: 1213-1223.

Li, H., Yezzi, A. & Cohen, L. (2009) 3D Multi-branch Tubular Surface and Centerline Extraction with 4D Iterative Key Points. *MICCAI 2009* **LNCS 5762**: 1042-1050.

Lloréns, R., Naranjo, V., Clemente, M., Alcañiz, M. & Albalat, S. (2009) Validation of Fuzzy Connectedness Segmentation for Jaw Tissues. *IWINAC 2009* **LNCS 5602**: 41-47.

Lorensen, W. E. & Cline, H. E. (1987) Marching Cubes: A high resolution 3d surface construction algorithm. *Computer Graphics* **21(4)**: 163-169.

McInerney, T. & Terzopoulos, D. (2000) T-snakes: Topology adaptive snakes. *Medical Image Analysis* **4**: 73-91.

Mohan, V., Sundaramoorthi, G. & Tannenbaum, A. (2010) Tubular Surface Segmentation for Extracting Anatomical Structures from Medical Imagery. *IEEE Transactions on Medical Imaging* **29(12)**:1945-1958.

Rueda, S., Gil, J. A., Pichery, R. & Alcañiz, M. (2006) Automatic Segmentation of Jaw Tissues in CT Using Active Appearance Models and Semi-automatic Landmarking. *MICCAI 2006* **LNCS 4190**: 167-174.

Sarment, D. P., Al-Shammari, K. & Kazor, C. E. (2003a) Stereolythographic surgical templates for placement of dental implants in complex cases. *The International Journal of Periodontics & Restorative Dentistry* **23(3)**: 287-295.

Sarment, D. P., Sukovic, P. & Clinthorne, N. (2003b) Accuracy of implant placement with a stereolithographic surgical guide. *The International Journal of Periodontics & Restorative Dentistry* **18(4)**: 571-577.

Tardieu, P., Vrielinck, L. & Escolano, E. (2003) Computer-assisted Implant Placement. A Case Report: Treatment of the Mandible. *The International Journal of Oral & Maxillofacial Implants* **18(4)**: 599-604.

Udupa, J. & Samarasekera, S. (1996) Fuzzy connectedness and object definition: Theory, algorithms, and applications in image segmentation. *Graphical Models and Image Processing* **58(3)**: 246-261.

Van Assche, N., van Steenberghe, D., Guerrero, M. E., Hirsch, E., Schutyser, F., Quirynen, M. & Jacobs, R. (2007) Accuracy of implant placement based on pre-surgical planning of three-dimensional cone-beam images: a pilot study. *Journal of Clinical Periodontology* **34(9)**: 816-821.

Van Steenberghe, D., Naert, I., Andersson, M., Brajnovic, I., Van Cleinenbreugel, J. & Suetens, P. (2002) A custom template and definite prosthesis allowing immediate implant loading in the maxilla: A clinical report. *Int.J.Oral Maxillofac Implants* **17**: 663-670.

Verstreken, K., Van Cleynenbreugel, J., Marchal, G., Naert, I., Suetens, P. & van Steenberghe, D. (1996) Computer-assisted planning of oral implant surgery: a three-dimensional approach. *International journal of oral & maxillofacial implants* **11(6)**: 806-810.

Verstreken, K., Van Cleynenbreugel, J., Martens, K., Marchal, G., van Steenberghe, D. & Suetens, P. (1998) An image-guided planning system for endosseous oral implants. *IEEE Transactions on Medical Imaging* **17(5)**: 842-852.

Sansoni, T. (1999) Tecniche di Elaborazione Grafica e Visione Applicate ad Immagini Medicali (Italian). In: Università di Ferrara – Dipartimento di Ingegneria, Tesi di Dottorato in Ingegneria dell'Informazione, XVI Ciclo

Twigg, C. (2003) Catmull-Rom splines.

Yau, H. T., Lin, Y. K., Tsou, L. S. & Lee, C. Y. (2008) An Adaptive Region Growing Method to Segment Inferior Alveolar Nerve Canal from 3D Medical Images for Dental Implant Surgery. *Computer-Aided Design and Applications* **5(5)**: 743-752.

CONFERENCES AND PUBLICATIONS

INTERNATIONAL JOURNALS

A fully 3D work context for oral implant planning and simulation
Chiarelli, T., Lamma, E. & Sansoni, T.
International Journal of Computer Assisted Radiology and Surgery; vol. 5, Issue 1: 57-67, 2010.

Techniques to Improve Preoperative Planning Precision for Oral Implantology
Chiarelli, T., Lamma, E. & Sansoni, T.
IEEE Transactions On Intrumentation and Measurement; vol. 59, Issue 11: 2887-2897, 2010.

INTERNATIONAL CONFERENCES

A Tool to Achieve Correct and Precise Measurements for Oral Implant Planning and Simulation
Chiarelli, T., Lamma, E. & Sansoni, T.
2009 IEEE International Workshop on Medical Measurements and Applications (MeMeA 2009); Proceedings: 246-251.
Cetraro, Italy. May 29-30 2009

A 3D Environment for oral implant planning and simulation
Chiarelli, T., Franchini, F., Lamma, A., Lamma, E. & Sansoni, T.
Computer Assisted Radiology and Surgery (CARS) 2009, 23rd International Congress and Exhibition; International Journal of Computer Assisted Radiology and Surgery, vol. 4, Supplement 1: S217-S219, Springer Verlag ed., Heidelberg, D, 2009.
Berlin, Germany. June 23-27 2009

ITALIAN WORKSHOPS AND CONFERENCES

Correct and Precise Measurements for Oral Implant Planning and Simulation: Approach and Software
Chiarelli, T., Lamma, E. & Sansoni, T.
2009 Era Scientific Conference; Seminar.
Cattolica, Italy. May 11 2009

Protocollo tecnico-clinico di chirurgia guidata con il sistema Dental Vox
Franchini F., Chiarelli, T., Lamma, A. & Zullo, A.
Convegno Associazione Nazionale Dentisti Italiani (ANDI) Roma, “Implantologia oggi: raggiungere l'eccellenza mediante la pianificazione protesica e computer-guidata”
Rome, Italy. October 2 2010.

SUBMITTED

From Implant Planning to Surgical Execution: an Integrated Approach for Surgery in Oral Implantology

Chiarelli, T., Franchini, F., Lamma, A., Lamma, E. & Sansoni, T.

Clinical Oral Implants Research.